Quantifying volume loss from rock penetration in sand during subsea rock installation, using a fallpipe vessel

Thesis report

T. S. E. (Ties) Verhagen

Delft University of Technology

TU Delft

GREAT LAKES
DREDGE & DOCK
COMPANY, LLC

Quantifying volume loss from rock penetration in sand during subsea rock installation, using a fallpipe vessel

Thesis report

by

T. S. E. (Ties) Verhagen

to obtain the degree of Master of Science
at the Delft University of Technology,

Student number:	4470710	
Project duration:	September 2022 – August 2023	
Committee members:	Dr. ir. A. Antonini	TU Delft, Coastal Engineering
	Dr. ir. . Hofland	TU Delft, Hydraulic Structures and Flood Risk
	Prof. dr. ir. C. van Rhee	TU Delft, Dredging Engineering
	M. Beton	Great Lakes Dredge & Dock Company, LLC

Acknowledgement

This thesis marks the final step in obtaining a master's degree in Hydraulic Engineering at the Delft University of Technology. The collaborative nature of this research with Great Lakes Dredge & Dock Company (GLDD), headquartered in Houston, Texas, adds a significant dimension to its importance. GLDD's active engagement in advancing offshore wind infrastructure in the United States is commendable, evident through their development of a cutting-edge subsea rock installation vessel that is under construction at the moment. I am grateful for the opportunity to align my research with GLDD's aspirations, with the hope that it can contribute constructively to their ongoing efforts towards a more sustainable future.
The process of conducting this research has ignited a profound passion within me for the field of subsea engineering. Such enthusiasm has prompted me to embark on a career in this dynamic domain.

First and foremost, I would like to extend my heartfelt gratitude to the late Prof. dr. ir. Cees van Rhee. His invaluable guidance has significantly shaped the trajectory of this thesis. His instrumental assistance in establishing the research framework and meticulous preparation for the lab tests were pivotal in driving this study forward. I am very thankful for the opportunity to collaborate with him over the course of several months. His dedication and expertise have left an indelible mark on this work and his absence will undoubtedly be felt deeply within the dredging community.

Furthermore, I would like to thank Dr. ir. Alessandro Antonini, whose responsiveness and insightful guidance proved invaluable during the course of this research. His ability to swiftly provide detailed insights and solutions to the challenges I encountered left a lasting impression on me. Following our discussions, I consistently departed with multiple pages filled with his notes and our collaborative insights, alongside a treasure trove of recommended books and articles. Additionally, I express my special thanks to him for assuming the role of committee chairman when I asked him to do so.

Moreover, I would like to thank my supervisor from GLDD, Michael Beton. Despite his demanding schedule, he consistently made the effort to engage in discussions about my progress and the challenges I encountered. Having someone on board with a pragmatic perspective on the problem proved invaluable. Whenever I found myself entangled in intricate details, Michael always provided steadfast solutions that kept me moving forward in my research. I am genuinely grateful for his commitment in bringing me to Houston on two occasions, where he dedicated substantial time and attention to delve deeply into the core of my research.

Finally, I would like to express my appreciation to Dr. ir. Bas Hofland for his invaluable support during a critical phase in my thesis. His willingness to invest time and effort has been very much appreciated. Dr. ir. Hofland swiftly immersed himself in the intricacies of my thesis topic, offering invaluable insights and enhancing the quality of my work with his incisive and lucid feedback.

T.S.E. Verhagen
Amsterdam. August 2023

Abstract

In the field of offshore engineering, subsea rock installation has emerged as a pivotal technique. As offshore operations extend to greater water depths, the deployment of a versatile fallpipe has become a cornerstone for precise rock particle placement. A comprehensive determination of the overall rock material volume required for installation entails accounting for geometric factors, operational losses, and seabed displacements. To ensure effective project management and cost estimation, a precise grasp of volume loss during installation proves indispensable. Against this backdrop, the current thesis delves into the intricate domain of volume loss stemming from rock penetration within sand substrates.

The core endeavor of this research is the development of a model that quantifies volume loss due to rock penetration within sandy seafloors. The investigation combines theoretical modeling with empirical validation through lab testing. Through analysis, it is revealed that the complex behavior of granular media necessitates an in-depth understanding of the theory, together with assumptions and simplifications to create an effective penetration depth model. The literature study outlines the various forces exerted on a rock as it impacts the seafloor and commences its penetration into the sand. Within the summation of forces, one component to consider is the bearing force exerted by the sand. This force can be calculated using two distinct approaches: the Terzaghi formula for shallow foundations and the Brinch Hansen formula, also applicable to shallow foundations. In this thesis, both formulas are employed to assess their applicability to the dynamic penetration of spherical particles in a sandy seafloor. Once these forces have been aggregated within the equation, two distinct methods to resolve the equation and determine the penetration depth of a spherical rock in sand are employed. The first method is rooted in the principle of a work-energy balance, stating that the cumulative work done by the sum of forces matches the change in the rock's kinetic energy. In contrast, the second method is based on the impulse-momentum balance, underlining the concept that the summation of forces multiplied by a specific duration in time, is equivalent to the change in the rock's momentum during that defined time interval. The work-energy method is preferred over the impulse-momentum method because of the specific objective of the single stone model, which centers on determining penetration depth, a distance measurement. The work-energy method inherently incorporates the distance variable within its formula, aligning directly with the desired outcome. In contrast, the impulse-momentum method necessitates calculating penetration depth by multiplying time with velocity for each discrete time step, introducing a less efficient computational process.
Following a comparison between the results derived from laboratory tests and the computed penetration depths using both the Terzaghi and Brinch Hansen-based models, it becomes evident that the Terzaghi formula offers a closer approximation to the behavior of the bearing force.

Further insights are drawn from multi-stone penetration testing, wherein assumptions and simplifications are strategically employed. The intersection of the multi-stone model with a three-dimensional normal distribution delineates the positions of rocks post-fallpipe discharge, bridging theoretical modeling with practical subsea rock installation scenarios. Although a somewhat unrealistic scenario of centric rock-rock collisions and perfect stacking of rocks on top of each other is assumed, the model provides a valuable worst-case scenario in terms of volume loss.

Though the model's validation is confined to sandy seafloors, its implications extend beyond. The study underscores the need for real-world data integration to refine the model.

Contents

Part I

introduction

1

Introduction to the research

1.1. Background

While the world's energy consumption continues to increase, world leaders are determined to make policies to reduce greenhouse gas emissions as much as possible. The Paris Agreement was signed in 2015 with the goal of strengthening the global response to the threat of climate change. Popular alternatives for coal-fired power plants are wind turbines. With space becoming more scarce as a result of the growing world population, onshore wind turbines become less popular compared to their offshore alternatives. This, in combination with the fact that wind speeds are larger and more uniform on offshore sites, results in an increase in the development of offshore wind farms (Esteban et al., 2011)(Kaldellis and Kapsali, 2013).

The U.S. also shifts its focus towards offshore wind energy with the development of Empire I & II, an offshore wind farm in front of the U.S. east coast that is expected to power one million households in New York with renewable energy, shaping the future of the offshore wind industry in the U.S. (GLDD, 2022). The development of such a large offshore wind park comes with great challenges, some of which will be discussed in this research.
An important challenge that arises when designing an offshore wind farm is caused by the development of a scour hole around the foundation of the wind turbines. Especially when using a monopile foundation, which was the case with almost 83% of the wind turbines connected to the network in Europe at the end of 2017, scour hole development is the main concern in offshore wind farms (Esteban et al., 2019).
Scour holes can be prevented by the installation of bed protection at the base of a monopile. Much research has been done on determining the required size of the rocks that make up the bed protection. An important formula was presented by Isbash in 1936, linking the required stone diameter to the flow velocity, relative density, and a stability constant (Isbash, 1935). To protect the bed around the monopile foundations from scour hole development, a consortium of Grate Lakes Dredge & Dock Company (GLDD) and Van Oord was chosen to perform subsea rock installation (SRI) works for Empire I & II.

During SRI, large amounts of rock are dumped from the deck of a ship, after which they descend through the water column and finally land on the seafloor. Multiple processes occur that influence the amount of rock volume that is required to successfully deliver the designed bed protection. Being able to quantify the effect of each of those processes can be especially useful for marine contractors like GLDD, for better estimating the amount of rock volume that is required for SRI projects.

Theoretical amounts of rock volume that are required for bed protections or subsea rock supports in the offshore industry can quite easily be determined from CAD drawings and 3D models of the design. The practical amount required for these kinds of projects however is a bigger challenge. With the arrival of the fallpipe vessel, contractors like GLDD can dump rocks more accurately than with its less accurate alternative, a side stone dump vessel, due to the reduction of the free fall height and thus a reduction of the influence of currents on the stones (IADC, 2019) (see section 2.3).

Previous research on the process of the rocks descending through the fallpipe (Vehmeijer, 2022) (Stoter, 2018) has already clarified important aspects of SRI such as the rock velocity, concentration and the distribution of rocks over the fallpipe's cross-sectional area. An uncertainty that remains however is the interaction of the rock with the seabed. Practice shows that a deviation from the theoretical amount of rock volume needed can occur due to the immediate displacement of the seabed (Visser and Van der Meer, 2008 and de Vries et al., 2009), which causes a larger amount of material to be needed than what was calculated beforehand with the use of technical drawings. Immediate displacement of the seabed is a process that consists of the following elements:

1. Surface erosion
2. Penetration of the rock particles into the seabed
3. Material flow into the rock skeleton
4. Immediate deformation of the subsoil (settlement)

Research has already been done on all four elements, yet there is no comprehensive model that approximates the volume losses during SRI as a result of rock-soil interaction. Estimates have been made for the thickness of the soil layer lost through soil erosion (de Vries et al., 2009) and models exist for the approximation of the amount of material that flows into the rock skeleton as a result of the buildup of contact stresses between the rock particles and the soil. Furthermore, with the use of PLAXIS or other finite element models, the immediate deformation of the subsoil can be modeled and determined. However, the penetration of the rock particles into the seabed is a great uncertainty when performing SRI. Miedema (2021), Visser and Van der Meer (2008), and De Vries et al. (2009) have written about a method to analytically determine the penetration depth of individual stones into the seabed. Beemsterboer (2013) has done research on the modeling of the penetration depth of rock particles into soft clay to better estimate the volume losses that occur during SRI (Beemsterboer, 2013) and found that 20% of the total volume lost during SRI is a result of rock penetration into the seabed. All of the aforementioned have used a single-stone model in their approach to this problem and all of them have assumed a seabed consisting of clay. In reality, however, rocks are not dumped one by one but in great numbers at the same time. This makes the single-stone model a good starting point for further research, however, it greatly simplifies the process that occurs in reality.

It is also important to recognize that seabeds can be made of a variety of substances, including sand, which is fundamentally different from clay in terms of its properties, which is why they differ greatly in terms of their structural qualities. The findings from Beemsterboer's research may therefore not necessarily be applicable to rock penetration in sand.

While clay exhibits high cohesion and low shear strength, with sand it is the other way around. When considering SRI techniques for sand as opposed to clay, this fundamental difference in their mechanical behavior necessitates a different approach regarding the expected volume losses. To ensure a thorough and precise installation process, the strategy and considerations used for each soil type must be adjusted to account for their distinct structural characteristics.

1.2. Objective and research questions

The objective for this thesis is to propose a modelling strategy to determine the volume losses that occur during subsea rock installation. With this objective, this thesis will contribute to a further understanding of the interaction between rock particles and the seabed which can be of great use for the offshore wind industry as well as for subsea pipe constructions and the construction of rubble mound breakwaters on soft soils.
The objective of this research can be translated into the following research question:

How can volume losses as a result of immediate penetration of rock particles in sand during subsea rock installation be quantified?

To answer the research question, the following sub-questions will have to be answered as well:

1. What forces act on a single stone while it penetrates a sandy seafloor?
2. What is the magnitude of the impact of each force on the overall penetration depth of an individual stone?
3. How are stones distributed across a flat seabed after being discharged from a fallpipe?
4. What affects the additional penetration depth of a stone when multiple stones land on top of each other?

1.3. Methodology

This study employs a systematic approach to answer the research (sub-)questions above. The following steps outline the methodology undertaken:

- **Literature Study**
  An in-depth review of existing literature will be conducted to delve into the nuances of subsea rock installation processes. This involved an inventory of forces acting on a body during penetration within granular media. The literature study is described in chapters 3.
- **Model Development**
  Based on the insights gained from the literature study, a computational model will be formulated. This model aims to accurately represent the forces and dynamics involved in subsea rock installation scenarios. This is described in chapter 4 and 5.
- **Data Collection and Analysis**
  A series of comprehensive laboratory experiments will be conducted to collect data to validate the computational model. This is done by performing scaled penetration tests. This data will then be analyzed to establish a robust validation framework for the computational model. This is done in chapters 6 and 7.
- **Model Validation**
  The computational model will be validated using the data collected from the laboratory tests. This validation process ensures that the model's outcomes align closely with the empirical observations, attesting to the model's accuracy and reliability. The validation of the model is described in chapters 8 and 9.
- **Real-life Application**
  Following successful validation, the computational model will be further refined to extend its application to real-life subsea rock installation scenarios. this means that the results of the model will be analyzed for larger rocks. This is described in chapter 11.

1.4. Delimitations

Because SRI is a complex subject with a lot of individual parameters influencing the penetration depth of rocks into the seabed and with that the volume loss, choices will have to be made for what to include in this graduation research. Therefore, it is important to clearly define the boundaries and limitations of the research.

To simplify the representation of rocks for research purposes, they will be approximated as spheres.

This choice is made because rocks come in various shapes, some more rounded while others may be flatter. The decision to use spherical schematization aims to ensure consistency and facilitate the investigation of external factors affecting penetration depth. This means that the laboratory tests will also be conducted using spherical objects. Also, next to coming in various shapes, rocks can also come in various sizes. For this research, only two different sphere sizes are used to validate the model.

Moreover, it should be mentioned that in the laboratory tests, the spheres are dropped individually, which means that the collective jet effect resulting from a group of rocks descending through water is not considered. Additionally, this research assumes that the rocks descend through still water, and thus, the influence of waves and currents is beyond the scope of this study.

Finally, a horizontal seabed is assumed in which the rocks penetrate immediately. In reality, a seabed can also be slightly inclined, resulting in the possibility that rocks bounce a couple of times before penetrating into the sand. This phenomenon is not taken into account in this study.

Part II

Theory

2

Offshore wind energy

Wind energy represents a clean and sustainable energy source that is undergoing rapid innovation. This form of energy harnesses the force of the wind, both on land and at sea. Driven by European energy policies, particularly in north-western regions, and further fueled by the advantage of higher and more consistent wind speeds at sea, offshore wind turbines are increasingly favored over their onshore counterparts. (Esteban et al., 2011)(Kaldellis and Kapsali, 2013). However, the construction of offshore wind turbines brings with it several challenges that will have to be overcome to see the project become a success. A short introduction to offshore wind turbines and their installation is given in **??** till section 2.3.

2.1. Different wind turbine foundations

Several types of foundations exist for offshore wind turbines, which vary in their applicability for different water depths. To begin with, offshore wind turbines can be categorized into bottom-mounted structures and floating structures. Floating structures are used when wind farms are constructed at great water depths, although they are only at the research and development stage. When focusing on the bottom-mounted structures, the monopile structure is the most widely used foundation technique for modern-day wind turbines. This will also be the kind of structure that will be used when constructing the Empire I and Empire II wind farms. A monopile structure consists of a steel tube with a diameter that can be up to 10m. The average diameter of the offshore wind turbines that were installed in 2018 however was 7.26m (Sánchez et al., 2019). The steel tube, which is driven into the seabed for several meters, transfers the load of the wind turbine to the subsoil where a force in the opposite direction is provided by the bearing capacity and the friction between the shaft and subsoil.

2.2. Scour development and prevention

As mentioned earlier in the introduction of this thesis, scour hole development is one of the main concerns when developing offshore wind farms. When there is paid insufficient attention to this problem, scour hole development can cause operational downtime and in some extreme cases, even the collapse of the wind turbine structure (Esteban et al., 2011). For this reason, the prevention of scour holes around the monopile foundation of wind turbines is an important part of the planning phase of wind farms.

Monopiles and other submarine structures that attach wind turbines to the seabed cause fluctuations in the hydraulic field that surrounds these structures (Whitehouse et al., 2011). Currents caused by waves or the tide force a flow of water around the monopile structure, resulting in the contraction of streamlines on both sides of the monopile. Caused by the fact that the reattachment point of the streamlines lies not directly behind the monopile, lee-wake vortices develop between the monopile and the reattachment point (Rambabu et al., 2003). Higher up in the water column, this does not cause any significant problems, however, at the seabed level, this is another story. The contraction of the streamlines and the lee-wake vortices cause a local increase in flow velocity, which can be enough to bring seabed particles into suspension. When these particles are carried away by the current, a scour hole forms around the monopile structure.

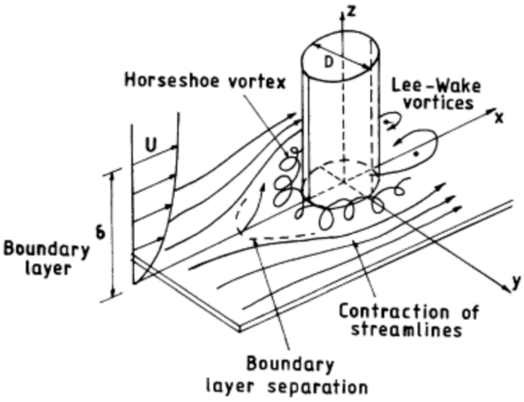

Figure 2.1: Flow around a cylindrical construction. Stevens et al., 1991

2.3. Subsea Rock Instalation

To construct the bed protection mentioned above, contractors perform SRI. SRI is done by dumping rock from a ship, which can be done in several different manners. These manners will be discussed in this subsection.

Side stone dumping

When it is desirable to dump large amounts of rock in a short amount of time and the focus does not lie on precision, the method of side stone dumping is regularly chosen for SRI. It is a very straightforward method of rock placement for which a Side Strone Dumping Vessel (SSDV) is commonly used in practice. This ship is loaded with a large amount of rock before it sails toward the desired dumping location. This dumping location should ideally be in shallow waters, to minimize the inaccuracy that comes with side stone dumping. When the SSDV has arrived at the dumping location, the rock material is deposited overboard using dozer blades that push the rock over the sides of the vessel. To make sure that the ship remains at the same position during dumping, most SSDVs are provided with a dynamic positioning system. An SSDV is shown in Figure 2.2.

Figure 2.2: A Van Oord side stone dumping vessel.

Fallpipe vessel

To achieve more precision during SRI, a fallpipe is used when placing rock at greater depths. A fallpipe is mostly used for the construction of rock supports for pipelines and internet cables on the seafloor. Because the rocks are in a guided descent through the fallpipe for the greatest part of the falling process, the rocks can be placed with high precision. A fallpipe vessel can have a flexible or a rigid fallpipe, where a flexible fallpipe consists of multiple bottomless buckets that are attached to each other. A fallpipe vessel that is currently under development by GLDD is shown in Figure 2.3(“Offshore wind”, n.d.)

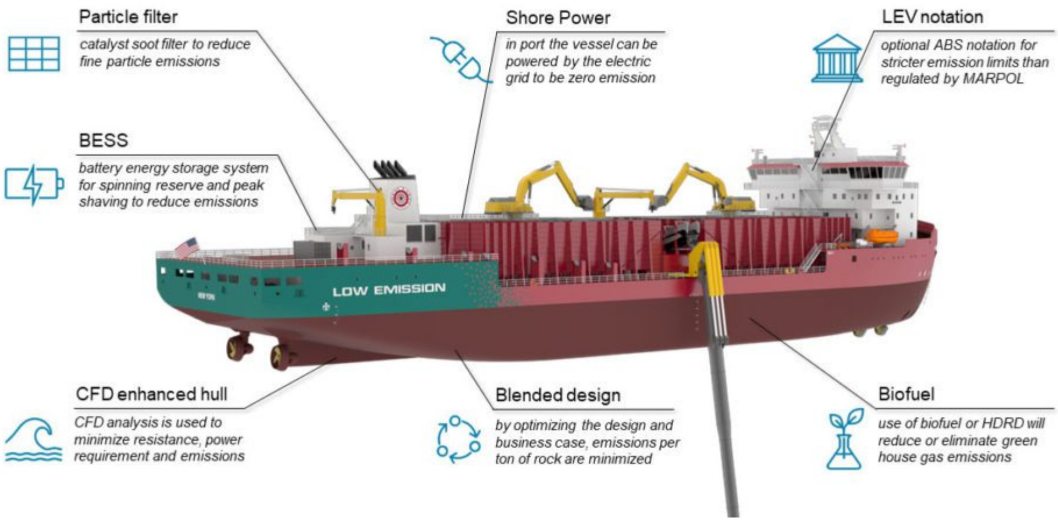

Figure 2.3: Fallpipe vessel currently under development by GLDD

3

Relevant properties and forces

In this section theoretical background will be provided on the process of rock-soil interaction. It is an essential part of this thesis since it focuses on the underlying physics of seabed penetration, which is what both the single- and multi-stone models will be based on. First, the relevant properties of rock and soil will be discussed, after which these properties will be translated into relevant forces that haven an influence on the penetration depth of the rocks into the subsoil.

3.1. Rock properties

The properties of the dumped rock can influence penetration. The density of certain rock material, together with the size and shape of the individual rock particles are important properties that should be taken into account when developing a rock penetration model.

First of all, the density of the rock material is an important property. In combination with the volume of individual rock particles, it determines the mass. If one would use vulcanic stone, for example, a rock material with a relatively low density, this would influence the penetration depth of the rocks and also on the effectiveness of the bed protection, since larger stones would be necessary to provide the required weight that would prevent the stones from being displaced by currents. In SRI projects, a commonly used rock type is granite. This particular rock type has a density between 2650- and 2750 kg/m^3 Furthermore, the size and shape and size of the rocks are important properties. The size has already been mentioned in combination with the density, determining the weight of individual rock particles. However, the size also has an influence on the production rate of the fallpipe vessel and the stability of the rock layer when it has been installed. A combination of the size and shape of the rock particles has a great influence on the settling velocity of the rock and the bearing capacity provided by the subsoil. A further explanation of this influence will be provided in section 3.3.

The rock that is used for SRI products is not produced in uniform sizes. This is a result of the production process of natural rock, which done by blasting. To make it possible to work with many different shapes and sizes, the European Standard EN133833 was created. This standard defines a set of size classes which are called ”standard gradings”. These gradings are defined by four limits:

- The Extreme Lower Limit (ELL): a maximum of 5% of the rocks in the grading is allowed to be smaller than the ELL.
- The Nominal Lower Limit (NLL): a maximum of 10% of the rocks in the grading is allowed to be smaller than the NLL.
- The Nominal Upper Limit (NUL): a maximum of 30% of the rocks in the grading is allowed to be larger than the NUL.
- The Extreme Upper Limit (EUL): a maximum of 3% of the rocks in the grading is allowed to be larger than the EUL.

For smaller rock gradings, the gradings are defined by size, while for the larger rock gradings, they are defined by weight. To convert mass into size (diameter), the nominal diameter method is used:

$$d_n = \sqrt[3]{\frac{\text{mass}}{\text{density}}} \tag{3.1}$$

The output of Equation 3.1 is the rib of a cube with the same volume as the rock in question. This means that the nominal diameter of a rock is always smaller than the sieve diameter ($\mathrm{d_s}$) because the shape of a rock is never a perfect cube. According to the rock manual (CUR, 2007), the nominal diameter of a rock can be calculated as follows:

$$\mathrm{d_n} = 0.84\mathrm{d_s} \tag{3.2}$$

This is however an empirical rule with a large variation. This is why Equation 3.1 is preferred over Equation 3.2. For application as bed protection, it is not desirable that rocks are too elongated. This means that the length-to-thickness ratio (LT) should be lower that a certain value. The LT ratio is determined by dividing the maximum length l [m] of a rock particle by the minimum distance d [m], the distance between two parallel lines through which the rock would just pass.

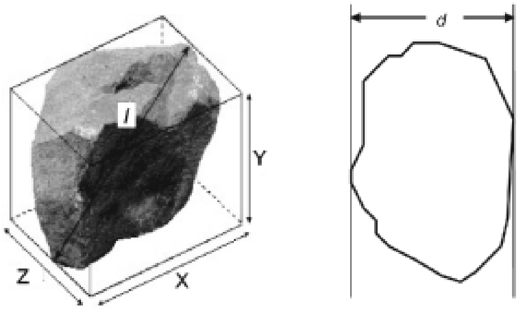

Figure 3.1: LT ratio CUR, 2007, showing L and d.

For course gradings (small stones), 20% of the stones in the grading are allowed to have an LT ratio over 3. With heavy gradings, which is the term in EN13383 for large stones, the relative amount of stones that have an LT ratio of over 3 can only be 5%. When a grading passes these LT ratio tests, the label may mention $\mathrm{LT_A}$. These rules prevent rock suppliers from delivering stones with shapes that are undesirable for the construction of (marine) structures.

3.2. Soil properties

When modeling the immediate penetration of rock particles into the soil, the properties of this the soil are relevant for determining its resistance to penetration. This resistance, or strength, is caused by the bearing capacity of the soil. There are two types of shear strength in soils: drained and undrained. If the water in a soil can flow out of the pores during shearing, the soil is said to be drained. Because the pore water pressure is zero, the total stress in the soil equals the effective stress. If this water is unable to drain from the pores due to the soil being sealed off, the soil will behave undrained.

Because the focus of this thesis lies on the penetration of rock particles in a sandy seafloor, the behavior of the subsoil can be considered drained. Sand is such a coarse material (relative to clay for example), that there is no water pressure build-up within the soil, meaning that the effective stress equals the total stress.

An important property of sandy soil is its angle of internal friction. This can be determined by drawing a mohr circle with the effective principal stresses ($\sigma_1^{'}$ & $\sigma_3^{'}$) as input. A mohr circle for drained shear strength can be seen in Figure 3.2. With the angle of internal friction, the bearing capacity of sandy soil can be determined. More on this topic will be discussed in section 3.3.

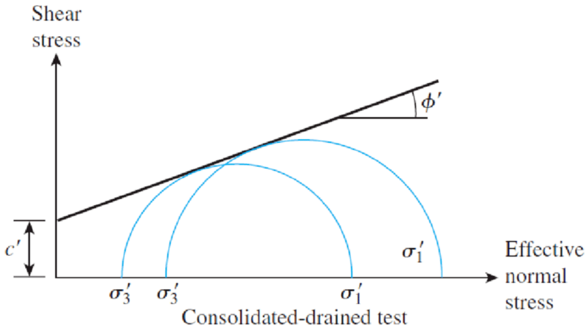

Figure 3.2: Mohr circle for drained shear strength (Albaba, 2012).

3.3. Scaling of the penetration depth

The forces that a projectile experiences as it enters a granular medium are extensively discussed in the literature. The force that slows a penetrating projectile down and eventually causes it to stop completely is not clearly understood to be dependent on any one factor. However, it is evident that this force is the end result of force chains that involve a number of particle-to-particle contacts (de Bruyn and Walsh, 2004). The combined effect of these chains produces a drag force that is experienced by a projectile, such as a stone, moving through the granular material. Numerous studies have attempted to comprehend the behavior of granular materials by examining their response to stress induced by impacts (Seguin et al., 2009)(Nordstrom et al., 2014)(Ciamarra et al., 2004)(Ambroso et al., 2005), although almost all of them relate to object penetration in dry sand. The topic of discussion however is the scaling characteristics of the drag force, because it is unknown if it depends on the impact velocity, the diameter, density, or the penetration depth of the object.
Brzinski III (Brzinski III et al., 2015) did research on the penetration depth scaling for impact into wet granular packings by releasing spheres into packings of spherical glass grains wetted either by water or mineral oil. He found out that the penetration depth in wet sand can be scaled by the same formula that was used for approximating the penetration depth in dry granular materials by Uehara et al. (Uehara et al., 2003):

$$d = (0.14/\mu)\rho_n^{1/2}D^{2/3}H^{1/3} \tag{3.3}$$

With:
d = penetration depth
μ = tan θ_R
θ_R = angle of repose for the grain material.
ρ_n = $\rho_{particle}/\rho_g$.
ρ_g = $\phi\rho_{gm}$
ϕ = the volume fraction of grains in the packing.
ρ_{gm} = the mass density of the grain material.
D = the diameter of the penetrator.
H = the fall height of the penetrator, including the penetration depth.

The constant of proportionality for water-saturated grains however is different from that of dry grains: 0.044 instead of 0.14. This would mean that water-saturated pores would cause a higher stopping force acting on penetrators than is the case with dry sand. According to Brzinski III, this would be the result of dilatancy and capillary action in the sand, and the magnitude of this extra stopping force scales with the impact velocity of the penetrating object. This will be discussed further in the thesis. However, if we look at Equation 3.3, it is obvious that the penetration depth in granular materials depends on the fall height of the object:

$$d :: H^{\frac{1}{3}} \tag{3.4}$$

This would mean that the penetration depth of an object depends on the energy it possesses at the moment of impact. Katsuragi and Durian, 2007 interpreted this scaling rule to be the result of an empirically determined drag force of which the magnitude could be derived from the following formula:

$$\sum F = -mg + k|z| + \frac{mv^2}{d_1} \tag{3.5}$$

In which k and the d_1 are constants obtained by using experimental data for fitting. The depth-dependent term $k|z|$ results from pressure that increases linearly with depth and the $\frac{mv^2}{d_1}$ term is caused by inertia-related drag. Seguin et al., 2009 presented a similar formula for describing the drag force between a penetrator and a granular medium:

$$\sum F = gm - F_z(z) - F_v(v) \tag{3.6}$$

Note that Equation 3.5 assumes a force directed upward as positive, while Equation 3.6 assumes a force directed downward as positive. According to Seguin et al., the granular friction that is not covered in Equation 3.5 and Equation 3.6 can be neglected since its order of magnitude is much smaller compared to the friction caused by pressure and inertia. For shallow penetrations, Equation 3.5 and Equation 3.6 seem to describe the sum of forces quite well (de Bruyn and Walsh, 2004).

As previously stated, the terms in Equation 3.5 and Equation 3.6 are dependent on the particularities of the performed test. Obtaining an accurate fit for k|z| and $\frac{mv^2}{d_1}$ still requires tailoring to the specific test conditions. However, Katsugari's findings suggest that $\frac{mv^2}{d_1}$ may be linked to $A\rho_g v^2$ at high Reynolds numbers (Katsuragi and Durian, 2013), which aligns with Van der Meer's assumption that the velocity-dependent component of the net force scales with a drag term (Visser and Van der Meer, 2008). Furthermore, the linear and depth-dependent component should be related to $\mu g \rho_g A|z|$ according to Katsugari, which again matches the work by Van der Meer where the depth-dependent force assumed to be related to the formula for ultimate bearing capacity by Brinch Hansen (Hansen, 1970). Because the particle-soil interaction that is being researched in this thesis takes place underwater, a buoyancy force makes up the first part of Equation 3.5 together with the gravity force.

In this way, a model can be created based on Equation 3.5 that returns the penetration depth by assuming the total stopping force is made up out of a gravitational term, a buoyancy term, an inertial drag term, and a pressure-dependent drag term.

3.4. Forces on a single stone

Gravity force

The gravity force is always directed downwards when we consider the x-axis to be parallel to the seabed and the y-axis perpendicular to it. The magnitude of the gravity force is dependent on the density and size of the stone by means of the following formula:

$$F_{grav} = V \cdot \rho_{rock} \cdot g \tag{3.7}$$

In Equation 3.7, g represents the gravitational acceleration constant (9.81 m/s). When considering the stone to be a sphere, the volume can be determined using a simple formula:

$$V_{rock} = \frac{1}{6}\pi d_n^3 \tag{3.8}$$

Combining Equation 3.7 and Equation 3.8, the gravity force acting on a single stone penetrating the seabed can be calculated using Equation 3.9

$$F_{grav} = \frac{1}{6}\pi d_n^3 \cdot \rho_{rock} \cdot g \tag{3.9}$$

As a body moves through a fluid, a certain volume surrounding this body also has to be brought into motion. This means that when the body accelerates (or decelerates), this volume of fluid surrounding the body has to do the same. In comparison to a situation where a body is accelerating in a vacuum, an extra force is needed when this happens in a fluid with a certain viscosity. Given that force is equal to mass times acceleration, we can think of the additional force as a fictitious increase in the object's mass in the fluid (Techet, n.d.).

This force acts in the opposite direction of acceleration. In the case of a stone decelerating as a result of a collision with the seafloor, the added mass force will be directed downwards and will cause a larger penetration compared to a situation in which the added mass force is neglected. The added mass coefficient is a measure of how the mass of a body is affected by the presence of a fluid (such as water or air). In the case of a sphere, the added mass coefficient is 0.5 (Ghassemi and Yari, 2011), which means that the added mass can be determined as follows:

$$M_{added} = \frac{1}{2} \cdot V_{rock} \cdot \rho_{water} \tag{3.10}$$

This mass is added to the mass of the stone, which increases the gravity force:

$$F_{grav} = (\frac{1}{6}\pi D_{rock}^3 \cdot \rho_{rock} + \frac{1}{2} \cdot \frac{1}{6}\pi D_n^3 \cdot \rho_{water}) \cdot g \tag{3.11}$$

Buoyancy force

Because this thesis considers subsea rock installation, a buoyancy force has to be taken into account that is directed opposite to the gravity force. The buoyancy force was defined by Archimedes and is equal to:

$$F_{buoyoancy} = V_{rock} \cdot \rho_{water} \cdot g \tag{3.12}$$

Again, the rock is considered to be a sphere of which the volume can be calculated using Equation 3.8.

Drag force

As a result of drag forces between the rock particle and the water particles, a resulting drag force is directed upwards with a magnitude that can be calculated using the following formula:

$$F_{drag} = \frac{1}{2} \cdot \rho_{water} \cdot v_{rock}^2 \cdot A \cdot C_D \tag{3.13}$$

In Equation 3.13 it is assumed that the (sea)water surrounding the rock particle is not moving in a vertical direction. A is the surface area of the rock that equals the surface area of a circle with diameter d_n as mentioned in Equation 3.8. C_D is the drag coefficient of which the value depends on the Reynolds number. The relation between the Reynolds number and the drag coefficient can be found in Equation 4.2.

Bearing force

As soon as the rock particle hits the seabed, the bearing force of the soil will also be part of the net force. An arbitrary type of soil can support a load up to a certain magnitude. The ultimate load that a soil can support before it fails is called the ultimate bearing capacity (UBC) of a soil. There are several views on estimating the UBC of a soil. Terzaghi (1943) was the first to develop a theory on the bearing capacity regarding shallow foundations, in which shallow meant that the width of the foundation is larger than the depth ($B > d$). He presented three formulas for three different kinds of foundations, namely square foundations, circular foundations, and continuous foundations (Terzaghi, 1943). In this thesis, the formula for computing the UBC for a circular foundation will be elaborated since the shape of a rock can best be described by a sphere that has an effective area in the shape of a circle. Terzaghi's formula for the UBC of a circular foundation is the following:

$$\frac{F_{bearing}}{A_{effective}} = 1.3cN_c + \gamma' zN_q + 0.3\gamma WN_\gamma \tag{3.14}$$

A_{eff} is the cross-sectional area of the rock particle that is penetrating the seabed. The size of A_{eff} depends on the penetration depth of the particle. Miedema(2021) used a slightly altered formula for computing the ultimate bearing capacity, based on experiments carried out by Beemsterboer(2013). This formula (3.15) better fits the situation of a foundation with the shape of a stone, which is not a strip or a square and neither exactly a circle. This method is from now on referred to as the adapted Terzaghi method.

$$\frac{F_{bearing}}{A_{effective}} = 1.2cN_c + \gamma' zN_q + 0.4\gamma' WN_\gamma \tag{3.15}$$

In both equations 3.14 and 3.15, γ' is the effective unit weight of the soil, c is the cohesion factor and W is the effective width of the foundation. The bearing capacity factors (N_i) are defined in the following way:

$$N_q = \frac{(e^{(\frac{3\pi}{4} - \frac{\phi}{2})tan(\phi)})^2}{2cos^2(\frac{\pi}{4} + \frac{\phi}{2})} \tag{3.16}$$

$$N_c = \frac{(N_q - 1)}{tan(\phi)} \tag{3.17}$$

$$N_\gamma = 1.5(N_q - 1)tan(\phi) \tag{3.18}$$

A limitation of Terzaghi's and Miedema's formulas is that they are only valid for shallow foundations, which means that the penetration depth of a stone can not be larger than its diameter (B < d). With SRI, it is conceivable that situations will occur where the penetration depth of stones is larger than their diameter, in which case equations 3.14 and 3.15 can not be applied. According to Bowles (1988), the best method for solving deep foundation situations is with the use of the Brinch Hansen theory because it allows any B/d ratio (Bowles, 1988). Brinch Hansen's formula for the ultimate bearing capacity of foundations is also used by Visser & Van der Meer (2008), De Vries et al. (2009) and Beemsterboer(2013):

$$\frac{F_{bearing}}{A_{effective}} = cN_c s_c d_c i_c g_c b_c + \gamma' z N_q s_q d_q i_q g_q b_q + \frac{1}{2}\gamma' W N_\gamma s_\gamma d_\gamma i_\gamma g_\gamma b_\gamma \tag{3.19}$$

W represents the effective width of the foundation. A schematic figure showing the effective width and effective area of a rock are shown in Appendix A. d_i represents the depth factors, i_i are factors that depend on the inclination of the force on the foundation while b_i represents the inclination of the base of the foundation itself. q is the effective surcharge that is acting on the soil and finally, the cohesion factor of the soil is represented by c (Hansen, 1970). The bearing capacity factors in Equation 3.19 should be calculated differently than for the Terzaghi method. For the Brinch Hansen method, the bearing capacity factors are determined in the following way:

$$N_q = e^{\pi tan(\phi)} tan^2(45 + \frac{\phi}{2} \tag{3.20}$$

$$N_c = (N_q - 1)cot(\phi) \tag{3.21}$$

$$N_\gamma = 1.5(N_q - 1)tan(\phi) \tag{3.22}$$

Because this thesis assumes a horizontal seabed that is penetrated by a stone/rock, all factors regarding the inclination of the soil or the stone itself can be neglected. The shape factors, however (s_i), should not be neglected. They are computed in the following way:

$$s_\gamma - 1 - 0.4\frac{B}{L} \tag{3.23}$$

$$s_q = 1 + sin(\phi)\frac{B}{L} \tag{3.24}$$

$$s_c = 0.2\frac{B}{L} \tag{3.25}$$

As mentioned earlier, A_{eff} depends on the penetration depth of the rock particles. Beemsterboer (2013) has presented a clear schematized drawing, showing the two different regimes of penetration of a rock particle into the seabed. This drawing is shown in Figure 3.3, which also clearly shows the dependence of A_{eff} on D_{cross}.

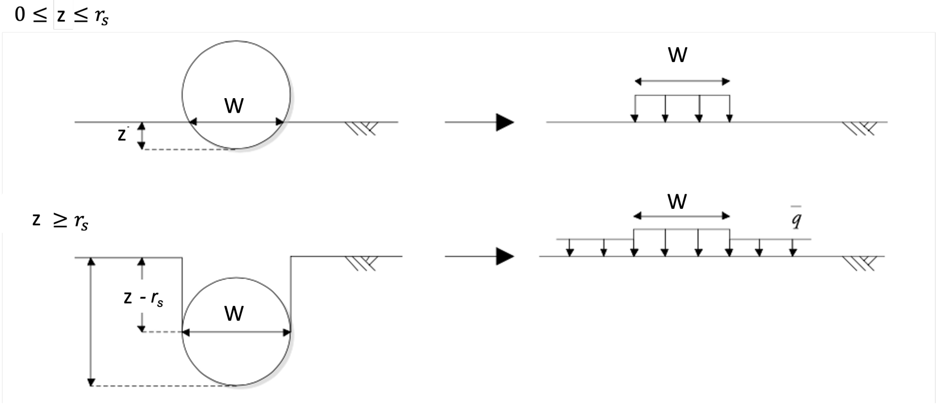

Figure 3.3: The two different regimes of penetration of a rock particle into the seabed. (Beemsterboer, 2013)

The formulas for determining the effective width (W) of the stone are presented below:

$$W = \begin{cases} 2 \cdot \sqrt{r_s^2 - (z - r_s)^2}, & 0 \leq z \leq r_s \\ 2 \cdot r_s, & z \geq r_s \end{cases} \tag{3.26}$$

With the effective width known, the effective area can be calculated with Equation 3.27.

$$A_{effective} = \frac{1}{4}\pi W^2 \tag{3.27}$$

Finally, a correction has to be made for the spherical shape of the rock particles. Since almost all foundations have a flat base, the equations by Brinch Hansen do not account for the extra bearing capacity of the soil that is a result of additional penetration by a spherical object. In other words, an extra wedge of soil is pushed away by the stone due to its spherical base. By multiplying the penetrated volume of the sphere by the unit weight of the soil, the formula takes the extra bearing capacity into account that is caused by additional penetration of the spherical object. The final formula becomes (Beemsterboer, 2013):

$$F_{bearing} = F_{Hansen} + V_{wedge} \cdot \overline{\gamma} \tag{3.28}$$

With the formula for V_{wedge}:

$$V_{wedge} = \begin{cases} \pi(r_s \cdot z^2 - \frac{1}{3}z^3), & 0 \leq z \leq r_s \\ \frac{2}{3}\pi r_s^3, & z \geq r_s \end{cases} \tag{3.29}$$

The formulas by Terzaghi and Brinch Hansen give different results when computing the bearing capacity for similar situations. In other words, the method used to assess bearing capacity has a significant impact on its outcome (Shill and Hoque, 2015). As an illustration, two plots are shown in Figure 3.4. Figure 3.4a shows the outcomes of the two methods as a function of the depth of the foundation, and Figure 3.4b shows the results of the two methods as a function of the angle of internal friction. In both cases, it concerns cohesionless soil (c = 0) with a unit mass of 1800 kg/m^3 and an effective unit mass of 775 kg/m^3. The foundation is a circular foundation with a diameter of 0.5m.

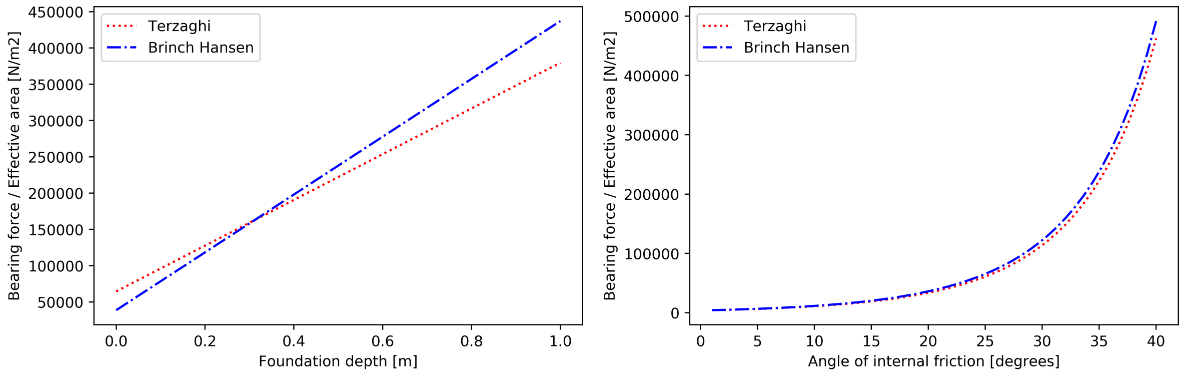

(a) Ultimate bearing capacity by Terzaghi and Brinch Hansen ($\phi = 35°$).**(b)** Ultimate bearing capacity by Terzaghi and Brinch Hansen (d = 0.5m).

Figure 3.4: Ultimate bearing capacity

From Figure 3.4a it can be observed that using the method by Terzaghi results in higher ultimate bearing capacities than the method by Brinch Hansen for foundation depths up to roughly 0.3 m. Although the ultimate bearing capacities for lower values for ϕ are more or less equal, the difference increases when the value for ϕ exceeds 25 degrees. Since the angle of internal friction (ϕ) for saturated sand lies between 30 and 45 degrees, this is something to take into account. To better compare the two methods, the same plots as in Figure 3.4 are shown although now for a depth- and internal friction angle range that is expected to be more applicable for the situation of a rock particle penetrating a seafloor of saturated sand.

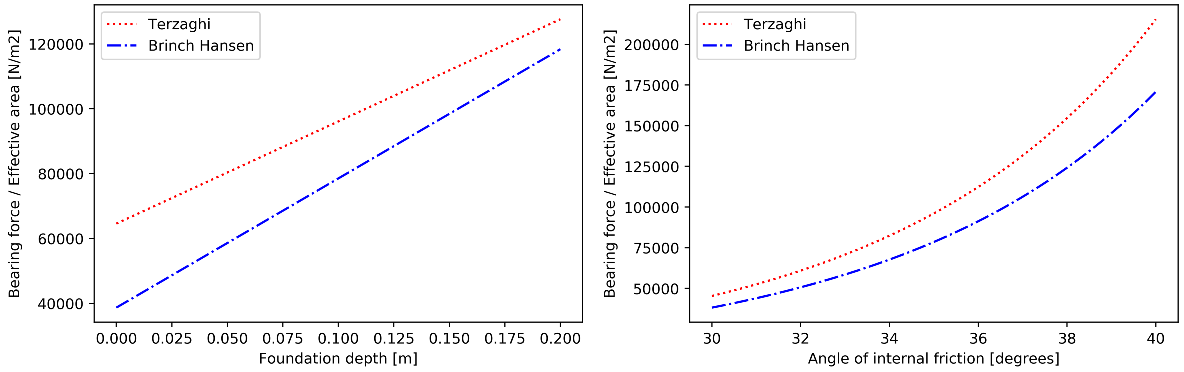

(a) Ultimate bearing capacity by Terzaghi and Brinch Hansen ($\phi = 35°$). **(b)** Ultimate bearing capacity by Terzaghi and Brinch Hansen (d = 0.1m).

Figure 3.5: Ultimate bearing capacity

In Figure 3.5 it is seen that for the range of values for the foundation depth and ϕ that is applicable to the subject of this thesis, the Terzaghi method results in higher ultimate bearing capacities than the Brinch Hansen method.

Dilatancy of the sand

The dilatancy of sand can significantly impact the resistance encountered by a rock particle during its penetration into saturated sand. The virgin seabed is typically characterized by a tightly packed structure, resulting in a relatively low void ratio. Upon impact of a stone, an increase in shear stresses in the deformation zone is observed, leading to an expansion in pore volume. Given the saturated nature of the sand, this additional pore volume must be filled with water. If the rate of penetration exceeds the ability of water to flow into the newly created pores, the resistance to penetration experienced by the stone is increased (Miedema, 2014).

An initial approximation of the influence of dilatancy may be attained by utilizing a formula designed for evaluating the force required for saturated sand cutting. The alteration in pore pressure within the saturated sand can be related to the cutting speed, the cutting depth, and the permeability of the sand (Van der Schrieck, 2006).

$$\Delta p = \frac{vh}{k} \cdot \Delta n \cdot \rho_w \cdot g \tag{3.30}$$

Where:

Δp = change in pore pressure [kPa].
v = impact velocity [m/s].
z = penetration depth of the stone.
k = permeability of the sand.
Δn = $\frac{\Delta V}{V}$.
V = volume of the sand.

Since the bearing force depends on the effective pressure within the soil, a drop in water pressure would mean an increase in the bearing force. Equation 3.30 is a formula used in dredging for determining the additional resistance from the sand on the cutter head of a cutter suction dredger. Regrettably, the formula has proven unsuitable for modeling the penetration of rocks in a sandy seafloor, as it significantly overestimates the strengthening effect on the sand. Consequently, this formula has been omitted from consideration in this thesis.

Net force

With all relevant forces discussed, the net force (F_{net}) on a single rock particle can be determined as the sum of all the relevant forces:

$$F_{net}(v,z) = F_{grav} - F_{buoyancy} - F_{drag}(v) - F_{bearing}(z) \tag{3.31}$$

The forces directed downward are taken as positive, which explains the minus sign in front of the gravity force. According to Bijnagte & Luger (2005), because the velocities are low, it is not necessary to take dynamic effects into consideration such as grain fractioning and inter-particle friction between the sand grains. This is consistent with the views of Seguin (Seguin et al., 2009). Of course, the impact velocity of the rock particle plays an important part in determining the penetration depth. In this research, the terminal settling velocity of rock particles will be used as the impact velocity. Because the terminal settling velocity is reached over a relatively short distance compared to an unsubmerged situation, the scaling rule of Katsugari and Durian (Katsuragi and Durian, 2007), who stated that the penetration depth is related to the total drop height to the power 1/3, does not apply. This study does not take into account the intermediate stage of subsea rock installation between the moment the stones leave the fallpipe and the moment the stones hit the seafloor.

4

Penetration depth of a single stone

To determine the penetration depth of a single stone into the seabed, the formulas that were discussed in section 3.3 will be used and combined. These formulas however only describe a static magnitude of a force, while the stopping force that acts on a penetrating object is, of course, dependent on z and on t. To be able to link the magnitude of the stopping force to the above-mentioned depth and time, several methods can be used. The impulse-momentum method is the most commonly used method. However, Miedema (2021) has used a method that is based on the work that is carried out by the soil when the bearing force is resisting the penetration by a rock particle. Both methods, together with several sub-methods, will be discussed and tested in this thesis. Due to the innate irregularities in the geometry of rocks that are used for bed protection, spherical rock particles are assumed in this model in order to assure a more standardized model.

4.1. Terminal settling velocity of a single rock

When a single stone settles through stagnant water, the balance of forces will ultimately determine the terminal settling velocity. This velocity is an important input parameter for the work-energy method, as well as for the impulse-momentum method. The acceleration of the stone can be determined with the use of Equation 4.1 (Van Rhee, 2002).

$$V_{rock}\frac{dv}{dt}(\rho_s + C_m\rho_w) = V_{rock}(\rho_s - \rho_w)g - C_d A_g \frac{1}{2}\rho_w v|v| \tag{4.1}$$

Where:

V_{rock} = Volume of the stone.
v = Vertical velocity of the stone.
A_g = Projected surface of the stone.
C_d = Drag coefficient.
C_m = Added mass coefficient.

Notice that the effect of buoyancy and the effect of the dynamic viscosity of the water are incorporated into the formula via respectively $(\rho_s - \rho_w)$ and the drag coefficient C_d.
C_d depends on the Reynolds number for a sphere. There are several empirical relationships between the Reynolds number and the drag coefficient. The most common ones are shown in

$$\begin{aligned} &C_d = \frac{24}{Re_p} \qquad Re_p \leq 1 \\ &C_d = \frac{24}{Re_p} + \frac{3}{\sqrt{Re_p}} + 0.34 \qquad 1 < Re_p < 2000 \\ &C_d = 0.4 \qquad Re_p \geq 2000 \end{aligned} \tag{4.2}$$

Where:

Re_p = vD/ν

For small grains such as clay or sand particles, it is possible that the Reynolds is equal to 1 (Stokes flow) or between 1 and 2000 (transitional regime). For stones that are used for SRI, the flow regime is almost always turbulent, which means that the Reynolds number is above 2000 and the drag coefficient is equal to 0.4. However, in the final stages of the impact, the velocity of the rock becomes close to zero, meaning that it is very well possible that the flow regime is laminar during those stages. However, since the drag force will play an almost negligible role when the velocity is close to zero, it can be assumed that the flow regime is turbulent during the whole penetration process.
To determine the terminal settling velocity, which is the velocity the stone reaches for $t \rightarrow \infty$, the acceleration ($\frac{dv}{dt}$) in Equation 4.1 should be set equal to 0. Now the terminal settling velocity can be calculated using the following formula:

$$w_0 = 1.8\sqrt{\Delta g D} \tag{4.3}$$

Where:
Δ = $\frac{\rho_s - \rho_w}{\rho_w}$

4.2. Work-energy method

The work-energy method is based on the principle that a certain amount of work equals a certain amount of kinetic energy. In other words, the net force that acts on a stone multiplied by the penetration depth is equal to the change in kinetic energy of the stone. Since the stone comes to a complete standstill after a certain distance, the change in kinetic energy is equal to the amount of kinetic energy the stone possesses just before coming into contact with the seabed. This means that the integral of the net force is equal to the total change in kinetic energy, as is shown in Equation 4.4.

$$\Delta E_{kinetic} = \int_{z=0}^{z=d} F_{net}(z)dz \tag{4.4}$$

In Equation 4.4, z is the vertical position of the rock. z is considered positive downwards and z=0 for the moment of impact. d is the final penetration depth of the stone. The kinetic energy of an object is calculated using Equation 4.5.

$$E_{kinetic} = \frac{1}{2}mv^2 \tag{4.5}$$

In Equation 4.5, v is the velocity of a rock at the moment of impact. Finally, m is the mass of the stone, including the added mass (Equation 3.10).

Equation 4.4 can be solved in two ways: as an ordinary differential equation (ODE) and as an algebraic equation. The latter was developed by Miedema (Miedema, 2021) and will be elaborated on first in subsection 4.2.1.

4.2.1. Static method

With this method, F_{bearing} is determined with the use of the Terzaghi method (Equation 3.15) and is assumed to be a static force, independent of z. Equation 4.4 is now no longer an equation containing an integral and can be written as Equation 4.6.

$$d = \frac{\Delta E_{kinetic}}{F_{net}} \tag{4.6}$$

In this case, z in Equation 3.15 is assumed to be 0, and W, which in reality depends on z as discussed in section 3.3, is now assumed to have a constant value equal to the diameter of the stone. $A_{effective}$ in Equation 3.15, which depends on W, is equal to $\frac{1}{4}\pi D^2$. Also, F_{net} in Equation 4.6 does not contain the drag force for this method (Miedema, 2021). Equation 4.6 provides a simplified approach to calculating the final penetration depth of a rock. Although it is a simplified formula, it does consider the impact velocity and rock diameter, which are factors expected to exhibit some correlation with the actual penetration depth in reality.

One drawback of this method is its inability to realistically depict the evolution of the net force. As the rock continues to penetrate the sand, the bearing force shifts from zero to becoming the dominant force within the net force. However, with this approach, the bearing force remains constant.

4.2.2. Numerical method

Equation 4.4 can also be solved as an ODE. The rate of change in kinetic energy is dependent on the magnitude of F_{net} and z. The further a rock penetrates the seafloor, the higher the bearing force becomes. Looking at Equation 3.15, we see that this works in two ways: a larger penetration depth directly results in a larger value for F_{bearing} via an increased value for z and thus a higher effective stress, and indirectly results in a larger value for F_{bearing} via an increased value for W, since W is a function of z (Equation 3.26). The differential equation for solving the penetration depth using the method based on work and energy is given in Equation 4.7(Clark and Behringer, 2013).

$$\frac{dK}{dz} = F_{gravity} - F_{buoyancy} - F_{drag}(v) - F_{bearing}(z) \tag{4.7}$$

Here, K represents the kinetic energy. Since v^2 is present in both the formula for kinetic energy (Equation 4.5) and for the drag force, v^2 can better be described as:

$$v^2 = \frac{2K}{m} \tag{4.8}$$

This way, it becomes possible to write Equation 4.7 in the following form:

$$\frac{dK}{dz} = F_{gravity} - F_{buoyancy} - F_{drag}(K) - F_{bearing}(z) \tag{4.9}$$

When the impact velocity is given as an initial condition, the initial kinetic energy can be determined and the ODE can be solved numerically.

$$\begin{aligned} v_{z=0} &= v_0 \\ z &= 0 \end{aligned} \tag{4.10}$$

With Equation 4.9, it can be calculated for which value of z, K = 0. This value for z will then be equal to the final penetration depth. In comparison with the static method, the numerical method has the advantage that it can calculate F_{net} as a function of z and v. A possible disadvantage is that Equation 4.9 can not be solved by hand whereas this is possible with Equation 4.6

It is also an option to combine the static and numeric methods. This combined approach would leverage the simplicity and efficiency of the static method while also incorporating the numerical method's ability to capture complex dynamics and non-linear behavior.
A way to do this is by presetting the effective area and the effective width ($A_{effective}$ and W respectively in Equation 3.15 and Equation 3.19) to fixed values. The effective area would be equal to $\frac{1}{4}\pi D^2$ and W would be equal to the diameter D. However, the bearing force would still be dependent on the penetration depth z, which is a different from the static method.

4.3. Impulse-momentum method

The impulse-momentum method is founded on the fundamental principle that a given impulse will result in a definite change of momentum. The net force on the rock particle is seen in this situation as a time-dependent force that will act on the particle for a certain amount of time, causing a corresponding change in the rock's velocity:

$$F_{net}(t) \cdot \Delta t = m \cdot \Delta v(t) \tag{4.11}$$

In Equation 4.11, F_{net} is the net force on the descending stone, Δt is the time step in seconds, m is the mass of the stone (including the added mass) and Δv is the variation in the velocity of the stone per time step Δt. Notice that with the impulse-momentum method, F_{net} is a function of time instead of distance as was the case with the work-energy method. This automatically means that Δv has to be a function of time as well. The further a stone penetrates the seafloor, the greater the bearing force delivered by the seafloor will become (Terzaghi, 1943, Hansen, 1970). With an increasing penetration depth, z and W in Equation 3.15 and Equation 3.19, $F_{bearing}$ will increase. In other words, $F_{bearing}$, which acts in the opposite direction to the direction of movement of the stone, will increase with time. Simultaneously, the drag force that acts on the stone will decrease as the velocity of the stone decreases.

The penetration of a stone comes to a halt when $v = 0$. In order to determine when this is the case, Equation 4.11 should be written in a different form (Holmen et al., 2017):

$$\Delta v(t) = \frac{F_{net}(t)}{m} \cdot \Delta t \tag{4.12}$$

If both sides of Equation 4.12 are divided by Δt, Equation 4.12 becomes Figure B.6a

$$\frac{\Delta v}{\Delta t} = \frac{F}{m} \tag{4.13}$$

Which is an ODE, equal to $F = m \cdot a$

With initial conditions

$$\begin{aligned} v_{t=0} &= v_0 \\ z_{t=0} &= z_0 = 0 \end{aligned} \tag{4.14}$$

Equation 4.13 can be solved numerically. Again, as was the case with the work-energy method in section 4.2, the effective area and effective width ($A_{effective}$ and W respectively in Equation 3.15 and Equation 3.19) can be a function of z or equal to preset values. The effective area would be equal to $\frac{1}{4}\pi D^2$ and W would be equal to the diameter D.

4.4. Sampling time and distance

Ordinary differential equations (ODEs) were resolved using the Runge-Kutta method. In order to solve initial value problems (IVPs) for ODEs, the Runge-Kutta method belongs to a class of iterative solutions. The explicit fourth-order Runge-Kutta (RK4) method and other variations of the Runge-Kutta method, as well as explicit and implicit methods with higher-order accuracy, are typically implemented by SciPy's solve-ivp function and are a popular approach. By dividing the integration interval into smaller steps and updating the solution at each step based on a weighted combination of function evaluations at various points within that step, it approximates the solution of an ODE. Since the error decreases with the fourth power of the step size, it is fourth-order accurate.

4.5. Overview of the methods

An overview of all the methods to calculate the penetration depth of individual stones is given in Figure 4.1.

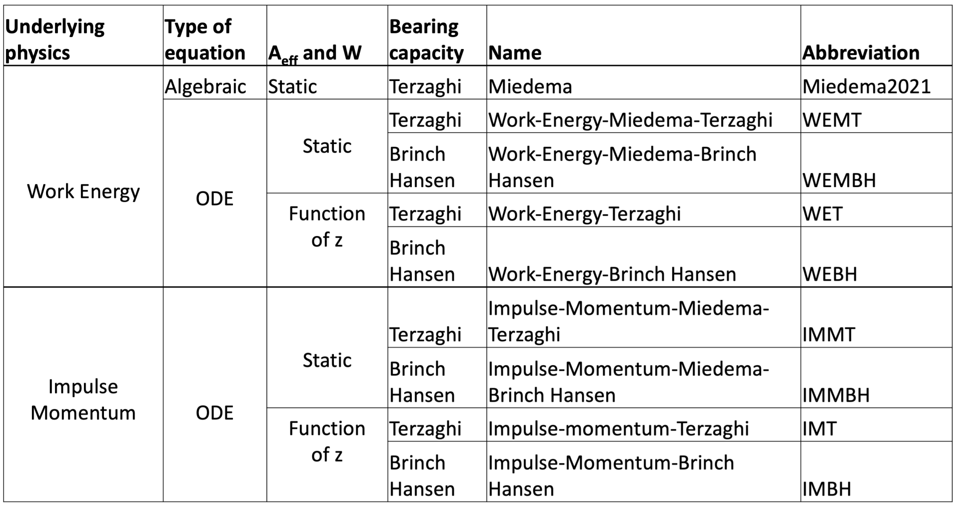

Underlying physics	Type of equation	A_{eff} and W	Bearing capacity	Name	Abbreviation
Work Energy	Algebraic	Static	Terzaghi	Miedema	Miedema2021
	ODE	Static	Terzaghi	Work-Energy-Miedema-Terzaghi	WEMT
			Brinch Hansen	Work-Energy-Miedema-Brinch Hansen	WEMBH
		Function of z	Terzaghi	Work-Energy-Terzaghi	WET
			Brinch Hansen	Work-Energy-Brinch Hansen	WEBH
Impulse Momentum	ODE	Static	Terzaghi	Impulse-Momentum-Miedema-Terzaghi	IMMT
			Brinch Hansen	Impulse-Momentum-Miedema-Brinch Hansen	IMMBH
		Function of z	Terzaghi	Impulse-momentum-Terzaghi	IMT
			Brinch Hansen	Impulse-Momentum-Brinch Hansen	IMBH

Figure 4.1: Overview of all the methods.

Both the work-energy method and the impulse-momentum method are employed to solve an identical equation. Consequently, when the same formula for bearing capacity and the same value for effective width are applied, these two methods should yield identical results. This expectation arises from the fact that both the work-energy balance and the impulse-momentum balance are well-established and proven concepts in the world of physics and mechanics. If we look at Figure A.2 in section A.3, we see that this is indeed the case.

Now, a well-informed selection of the most suitable method aligning with the primary focus of this thesis can be made. Given that the primary concern revolves around the penetration depth of rocks, rather than the duration of penetration, the work-energy method emerges as the logical choice. This decision arises from the fact that the work-energy balance equation inherently includes the distance variable, making it directly relevant to our objectives.
In contrast, the impulse-momentum balance doesn't explicitly incorporate distance since momentum is dependent on mass and velocity. While it is possible to compute the distance traveled during each time step by multiplying the current velocity by the time interval, this approach introduces additional computational steps, rendering the impulse-momentum method less efficient.
Moreover, the choice of which velocity to use for determining the distance traveled over the time step becomes a pertinent question when employing the impulse-momentum method. Should it be the velocity at the start of delta t, the velocity at the end of delta t, or perhaps the average velocity between these two time points? Given the computational modeling complexities and the focus of this thesis, we will not delve further into this issue at present. Therefore, for the remainder of this thesis, the preferred and adopted method will be the work-energy method.

5

Multi stone penetration model

When constructing bed protection to prevent scour hole development near an offshore wind turbine, a large number of stones is dropped in a relatively short amount of time. This makes the approximation of the process using a single-stone model a very simplified version of reality. Other particles will settle on top of the earlier layers once the initial particles have filtered through the soil. The penetrated particles will be pushed deeper into the seafloor as a result of this process. Beemsterboer (2013) has covered this process in his thesis, albeit in a very simplified way.
Using a simpler method can be advantageous because it might remove the need for highly detailed numerical models that involve calculating interactions between each stone. This approach provides a practical and efficient alternative that can significantly reduce the computational complexity and resource requirements associated with more intricate numerical models.

An analytical way to determine the additional penetration as a result of multiple stones falling on top of each other is by using the principle of momentum conservation. This principle was used by Beemsterboer (2013) when he wrote an introduction for a method to describe the process behind the dumping of multiple stones at the same time. When one stone falls on top of another and the collision is considered to be 100% plastic, it can be assumed that the additional stone's extra impulse is equivalent to the extra momentum of the two stones combined. When the masses of both stones are known, the increase in momentum can be translated to a change in the velocity of the two stones. Now the situation regarding two stones can be treated as a single-stone situation. To illustrate this analytical method, Beemsterboer presented a clear drawing of the process that can be seen in Figure 5.1

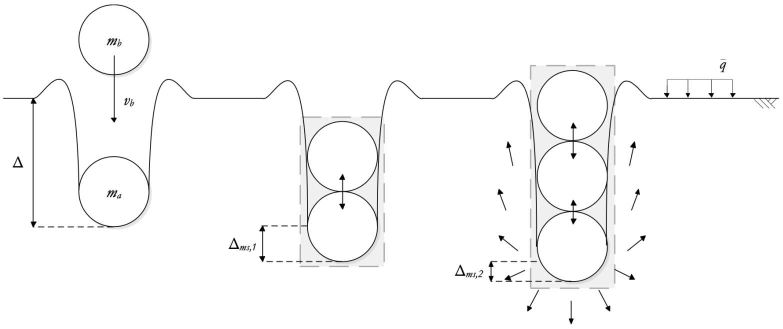

Figure 5.1: Multi stone penetration (Beemsterboer, 2013)

To further use this method, it should be clear what kind of simplifications have been made. First, Beemsterboer assumed that the new particle's impact velocity and mass are equivalent to the previous stones. Secondly, the previous stone has already come to a complete stop before the next stone collides. Thirdly, the impact is modeled as totally plastic, meaning that after impact, both particles are combined to form a single mass that travels with one speed and one direction. The collision is finally simplified

as a central impact, in which case both masses collide along a linear line of impact.
Using these assumptions, the situation schematized in Figure 5.1 can be translated to the following equations:

$$(m_a v_a)_1 + (m_b v_b)_1 = (m_a v_a)_2 + (m_b v_b)_2 \tag{5.1}$$

I.e., the momentum of the two separate masses before the collision is equal to the momentum of the combined masses after the collision. This is due to the 100% plastic collision with zero energy loss. Next, the assumption on mass and impact velocity is written in the form of three equations:

$$m_a = m_b \tag{5.2}$$

$$(v_a)_1 = 0 \tag{5.3}$$

$$(v_b)_1 = v_{imp} \tag{5.4}$$

With the mass of the two stones known, as well as the initial velocity of both masses, the velocity of the combined mass directly after impact can be calculated:

$$m_a \cdot 0 + m_b \cdot v_{imp} = (m_a + m_b) \cdot v_{combined} \tag{5.5}$$

Combining Equation 5.2 and Equation 5.5 we can write $m_a + m_b$ as $2m_b$. With the mass now being twice as large as before the impact, the velocity of the two masses combined should be half the impact velocity of the second stone:

$$m_a \cdot 0 + m_b \cdot v_{imp} = 2m_b \cdot \frac{1}{2} v_{imp} \tag{5.6}$$

$$v_{combined} = \frac{1}{2} v_{imp} \tag{5.7}$$

With the combined velocity, the combined additional penetration can be determined using the same formula as for a single stone. According to this method, the additional penetration for the ith stone would be:

$$v_{combined,i} = \frac{1}{i} \cdot v_{imp} \tag{5.8}$$

Equation 5.8 raises the question after how many stones the additional penetration can be considered insignificant (Miedema, 2021).

It is important to acknowledge that the results obtained using this method represent a worst-case scenario for the penetration depth of the initial stone impacting the seabed. In reality, the probability of four stones striking the first stone directly on top of each other is highly unlikely, and the chance of them aligning perfectly in a vertical pile is even smaller. In practice, the stones are more likely to land adjacent to the stone they strike, and as more stones accumulate on the seafloor, the momentum from incoming stones will be dispersed among multiple stones upon impact, resulting in very little additional penetration.
Despite these considerations, the method provides a valuable initial approximation for the subsea rock installation process. While it may not fully capture the complex dynamics of real-world scenarios, it serves as a practical starting point to estimate the worst-case outcome in terms of penetration depth.

Part III

Data gathering

6

Lab experiments

6.1. Aim of lab testing

This thesis looks into the volume of rock material that is lost during the installation of subsea rock using a fallpipe vessel. A contractor is especially concerned with rock particles penetrating the seabed because they don't contribute to the design and could be considered lost. The amount of material needed must be increased to install additional volumes of rock to make up for this loss. Contractors have long sought to precisely predict the penetration depth of these rocks to estimate the amount of material needed more precisely. The theoretical context for this issue is presented in the preceding section.

To determine the theory's practical applicability, several experiments were carried out to see how far objects penetrate into sand under certain conditions. With the help of these experiments, it is possible to better understand the factors that affect rock penetration. The experimental data can also be used to verify the single stone rock penetration model that was developed.

Because there are so many factors influencing the penetration depth during subsea rock installation, it is undesirable to change each element independently. Therefore it was decided to reduce the number of variables in order to simplify the analysis. Three significant parameters were determined with the help of the literature and studying the governing equations. These three parameters are fall height, particle diameter and D_{50} of the sand. Various sets of laboratory tests will systematically vary these parameters. Multiple tests can be compared to one another, providing helpful insights, by isolating the impact of each individual parameter and carrying out all tests in a standardized setting. To simulate the individual stones during subsea rock installation, marbles of different sizes are used during the experiments.

6.2. Set-up

6.2.1. Single-stone testing

As already indicated, the laboratory tests will involve varying three variables: fall height, particle diameter, and the grain size distribution of the sand.

The fall height from which the objects are dropped directly influences the impact velocity, whereas the impact velocity of the rocks is an important variable as it has a huge influence on the kinetic energy at the moment of impact, as well as on the momentum the rocks possess at that moment. This means that the impact velocity determines the initial condition for both the method that is based on work and energy and the method that is based on impulse and momentum. A larger impact velocity increases the amount of kinetic energy quadratically, while it increases the momentum of the rock linearly.

The diameter of the particles is another important factor that has a significant impact on the depth to which they penetrate sand. The diameter is important because it affects the particle's volume to a power of three, as well as its momentum and kinetic energy.

The D_{50} of the sand has an influence on the strength characteristics of the soil. The grain size distribution overall determines the coefficient of unity (C_u), which determines the maximum and minimum void ratio of the soil. Via the void ratio range, the relative density (D_r) can be determined, which is linked to the angle of internal friction. The angle of internal friction is the most important parameter inside the Terzaghi equation, which means that the ultimate bearing capacity is partly determined by the D_{50}. This will be elaborated more in section 6.3

An experiment setup has to be made that allows for repeating a certain experiment exactly, with only changing one of the aforementioned variables. This means that the drop height should be changeable while keeping the sand properties and object diameter the same, the object diameter should be changeable while keeping the drop height and sand properties the same, and the sand properties should be changeable while keeping the object diameter and drop height the same.

In order to accurately determine the impact velocity of the particles, it is necessary to track their movement. This is done using specialized tracking software which requires high-resolution videos with a high frame rate (FPS) for each experiment. To facilitate this, the container in which the experiments are conducted needs to have transparent sides, allowing sufficient light to reach the penetration area and enabling filming from outside the container. Therefore, the container must be constructed using materials such as glass or plexiglass to maintain transparency. A GoPro Hero 11 camera is used to record each test run because of its advanced capabilities, including the ability to shoot high-quality videos. It supports 4K video recording at 120 FPS and 2.7K video recording at 240 FPS. This high frame rate enables capturing detailed and smooth footage, facilitating accurate analysis of the experiments. Additionally, the camera's waterproof feature allows for underwater recording, expanding the range of possible scenarios and enhancing the comprehensive documentation of the experiments conducted in submerged environments. Finally, the container should have certain dimensions relative to the particle diameter to limit the boundary effects of the container. According to literature, the sides of the container should at least have a length that is ten times the diameter of the particle that is used for testing, and the thickness of the sand layer should be at least five times the particle diameter (Craig and Sabagh, 1994).

All of the above-mentioned criteria considered, the following values for variables were selected:

Variable	**Diameter [cm]**	**Fall height [cm]**	**Sand types** [-]
Variety	3	3	2
Values	2.5, 3.5, 6	10, 30, 50	coarse- and fine sand

Table 6.1: Variables for lab testing. Marbles with a density of 2400kg/m^3 were used to simulate the rock dumping process.

This leads to a minimal amount of different test runs that should be carried out in the laboratory of 18, which was determined with the following formula:

$$n_T = n_d \cdot n_{fh} \cdot n_{sp} \tag{6.1}$$

Where:

n_T = number of test runs.

n_d = the number of different particle diameters.

n_{fh} = the amount of different fall heights.

n_{sp} = the amount of different kinds of sand.

To minimize measurement errors and ensure consistency as much as possible, the marbles are dropped from a fixed point and each test run is repeated at least three times which brings the minimal amount of test runs to 54.

The following test setup was designed:

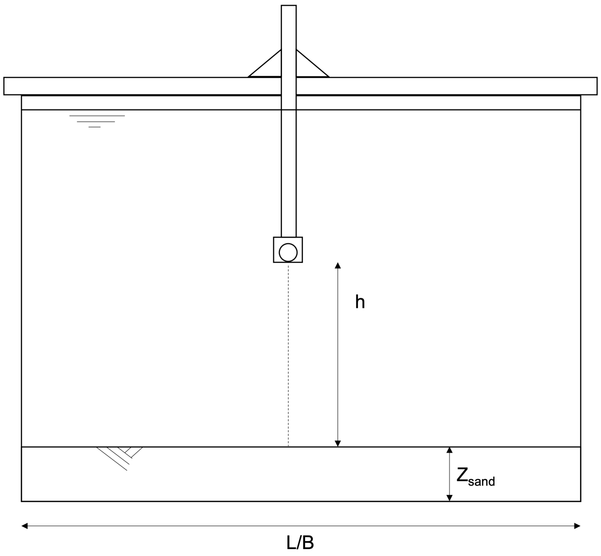

Figure 6.1: Simplified test setup

Constructing the test setup shown in Figure 6.1 is carried out taking the following steps:

1. Coarse sand (DORSILIT® nr.8 (section 6.3)) is supplied in 25kg bags that are emptied inside one of the two containers. After almost 10 bags (245kg) the minimum sand layer thickness of 30cm is reached.
2. The sand layer is densified using a vibrating needle that is inserted into the sand at multiple locations and kept at the same location for roughly one minute. This allows for the sand to reach a more compacted state as would be the case at the bottom of the sea.
3. The dimensions of the container and the thickness of the sandbed are measured again in order to determine the porosity.
4. A clamp is attached to the sides of the container using two aluminum bars, both with a sliding slot in the middle so that the height and position of the clamp can be adjusted. This helps with creating consistency regarding the drop height throughout all test runs.
5. The container is very carefully filled with water. A metal plate is placed on top of the sand layer to ensure the sand stays in its compact state as much as possible. Water is sprayed onto the sides of the container from a hose that is set to its spray position, to keep the velocity of the water is as low as possible when it reaches the sand layer. The hose is switched off as soon as the water level reaches a height of 85cm, measured from the bottom of the container.
6. Steps 1-4 are repeated for the fine sand (SIBELCO M34 (section 6.3)).

6.2.2. Multi-stone testing

To investigate what effect stone collision on the sandbed has on the total penetration depth, the lab experiments also include multi-stone tests. This is done in the course sand type with only the large marbles. The objective is to determine whether the collision between objects is of a plastic or elastic nature and to quantify the additional penetration as a result of the marble collisions.

By analyzing video recordings of the collision, it is possible to identify the type of collision and determine whether it is of a plastic or elastic nature.

The multi-stone experiments will be executed in the same container as the experiments for the penetration depth in coarse sand.

6.3. Sand properties

To assess the effect of a particular type of sand on the process of stone penetration, two types of soil will be used to create a sand bed at the bottom of the container. Both soils will consist of quartz sand, which is composed almost entirely of silicon dioxide (SiO_4). Quartz sand is characterized by sub-angular particles, a property that affects the bearing capacity. Other properties that affect the bearing capacity of sand are the grain size distribution, permeability, and porosity.

6.3.1. Grain size distribution

First, DORSILIT® quartz sand with a D_{50} of 0.51mm is used as sandbed on which the marbles will be dropped from different heights. When all three marbles are dropped three times from all different heights, the experiment will be repeated in SIBELCO M34 quartz sand with a D_{50} of 0.17mm. The grain size distribution graphs of the two types of quartz sand are shown in Figure 6.2 and Figure 6.3. Because the two types of sand consist of more than 98% of the same material, which is silicon dioxide, their densities are almost identical: 2650 kg/m^3 for the SIBELCO sand and 2630 kg/m^3 for the DORSILIT® sand. The data sheets of both sand types can be found in section B.1.

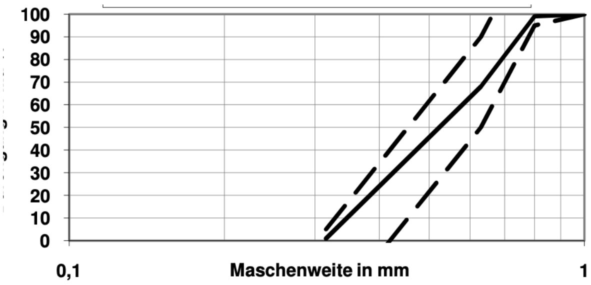

Figure 6.2: Grain size distribution for DORSILIT® nr. 8 0.3 - 0.8 mm quartz sand.

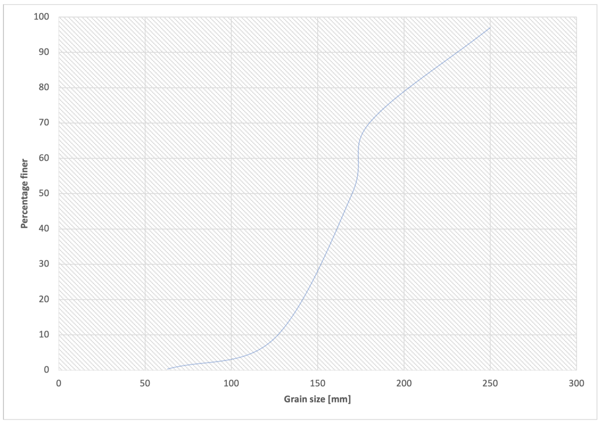

Figure 6.3: Grain size distribution of SIBELCO M34 quartz sand.

As can be seen in the two figures above, there is a significant difference in median grain size between the two types of sand. More properties are shown in section B.1.

6.3.2. Porosity

The porosity of sand depends on its void ratio. In subsection 6.3.4 and subsection 6.3.5, the void ratio will be utilized to establish a connection between the grain size distributions of the two types of sand and the angle of internal friction. This angle of internal friction is a crucial factor in determining the ultimate bearing capacity of the sand. The porosity of a material is determined by dividing the volume of the voids within the material by its total volume. As a result, porosity is a dimensionless quantity and does not possess any specific unit of measurement. It is important to note that, due to the overlapping use of the symbol ϕ for both the angle of internal friction and porosity, the symbol ϕ_p will be employed specifically to denote porosity throughout this thesis.

$$\phi_p = \frac{V_{voids}}{V_{total}} \tag{6.2}$$

With:
ϕ_p = porosity [-].
V_{voids} = volume of the voids [m^3].
V_{total} = total volume of the material [m^3].

Both the containers that are used for the experiments have the same ground surface dimensions, e.g. 0.75 x 0.72m. First, 245 kg of DORSILIT® nr. 8 0.3 - 0.8 mm quartz sand, (from now on 'coarse sand') was shoveled into the first container. After compacting the sand layer with a vibrating needle, a sand layer remained with a thickness of 30cm. This exactly meets the requirement for the minimum sand layer thickness of 5 times the largest marble diameter (Craig and Sabagh, 1994). Now the porosity can be calculated using the following formulas:

$$V_{total} = L \cdot B \cdot Z_{sand} \quad \text{(Figure 6.1)} \tag{6.3}$$

$$V_{voids} = V_{total} - \frac{mass_{solids}}{\rho_{sand}} \tag{6.4}$$

With the use of Equation 6.3.2 and Equation 6.3.2 the porosity of the coarse sand was estimated to be 0.42. After this, the second container was filled with SIBELCO M34 quartz sand (from now on referred to as 'fine sand'). The second container has the same dimensions as the first one (0.75m by 0.72m). Again, sand was shoveled in, this time 245 kg of the fine sand type. After densifying the sand with the vibrating needle, a sand layer with a thickness of 27cm remained. Unfortunately, this is just short of the $5D_{marble}$ that is required to limit the boundary effects of the container, however, since the penetration depth of the marbles in fine sand is expected to be very small, this is not expected to cause any issues. After using Equation 6.3.2 and Equation 6.3.2 again, the porosity of the fine sand is determined to be 0.37.

6.3.3. Permeability

Understanding the phenomenon of dilatancy and its significant impact on the material's bearing capacity depends critically on the permeability of the sand. Dilatancy is the tendency for granular materials, like sand, to enlarge and gain volume when subjected to shear stresses. The rearrangement and re-orientation of particles within the sand matrix cause this expansion to happen.

The speed at which water can pass through sand is directly influenced by its permeability. Sands with a higher permeability facilitate water flow while sands with a lower permeability restrict it. If the flow of water can not keep up with the rate of increase of pore volume, a drop in water pressure occurs which results in an increase of effective stress (section 3.3).

In order to accurately predict and evaluate the impact of dilatancy on sand's bearing capacity, it is crucial to know the order of magnitude of the permeability. This depends on the grain diameter as well as the porosity. The permeability of the fine- and coarse-grained sand used in this thesis was estimated using a diagram showing the permeability of different kinds of Dutch sand as a function of porosity (Figure 6.4)

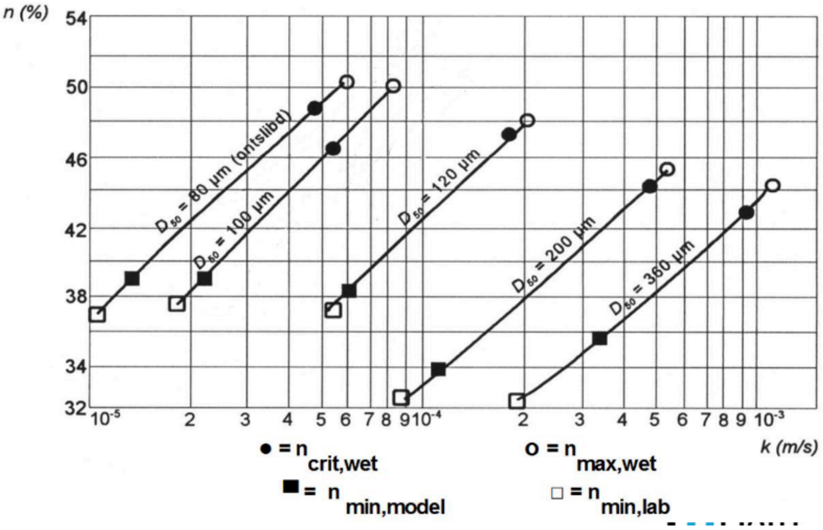

Figure 6.4: Permeability as a function of porosity (Van der Schrieck, 2006

With the help of Figure 6.4, the permeability of both sand types was estimated to be $2 \cdot 10^{-3}$ and $2 \cdot 10^{-4}$ m/s for coarse- and fine sand respectively.
These values correspond closely to the calculated values for the permeability of sand when Wang's formula is used (Wang et al., 2017). By examining 431 different sand samples with different compositions, he developed a general formula that links the d_{60} and uniformity coefficient to permeability. The formula is shown in Equation 6.5.

$$k = C_w C_u^a \frac{g}{\nu} D_{60}^2 (\log_{10}(\frac{g D_{60}^3}{v^2}))^{-1} \tag{6.5}$$

With:
C_w : = a constant equal to $2\,9 \cdot 10^-3$
C_u = Uniformity coefficient
g = Gravitational acceleration
ν = Kinematic viscosity water, normalized at $0\,89 \cdot 10^{-6}$ for 25 degrees Celcius
D_{60} = Grain size at 60% passing

Via the grain size distribution, it is possible to determine the uniformity coefficient (C_u) of a soil, which is done in the following way:

$$c_u = \frac{D_{60}}{D_{10}} \tag{6.6}$$

In Equation 6.5, the parameter D_{60} represents the particle diameter at which 60% of the soil sample is finer. The coarse sand that was used for the lab experiments has a uniformity coefficient of 1.66 while the fine sand has a uniformity coefficient of 1.4. To determine these values, Figure 6.2 and Figure 6.3 were used.
Filling in Equation 6.5 for both sand types gives leads to a permeability of $1\,15 \cdot 10^{-4}$ $2\,74 \cdot 10^{-4}$ for the coarse- and fine sand respectively.

6.3.4. Void ratio and relative density

The density and degree of compaction have a significant influence on the engineering properties of sandy soils (Hatanaka and Feng, 2006). Due to the impact of soil particle characteristics such as size, shape, and uniformity, the assessment of compactness in sandy soils cannot rely solely on in-situ dry density, which means that only comparing the particle density of the sand to the in-situ density of the sand is not sufficient for determining it's bearing capacity. To effectively characterize the density of a natural granular soil, a valuable approach is to utilize relative density.
The relative density of a soil, also known as density index or degree of compaction, can be given as a percentage or as a fraction and is used to characterize the in-situ density of a granular material to its maximum achievable density. This maximum achievable density is a theoretical density that can only

be achieved under ideal conditions. The relative density is determined via the maximum void ratio, the minimum void ratio, and the in-situ void ratio (Sumer, 2014)(Figure 6.5).

$$D_r = \frac{e_{max} - e}{e_{max} - e_{min}} \tag{6.7}$$

With:
D_r = relative density [-]
e_{max} = maximum void ratio
e_{min} = minimum void ratio

The void ratio (e) and porosity of a material are distinct concepts. While porosity represents the relative volume of voids compared to the total volume, the void ratio specifically indicates the relative volume of voids in relation to the volume of the solid particles themselves.

$$e = \frac{V_{voids}}{V_{solids}} \tag{6.8}$$

(a) **(b)**

Figure 6.5: Schematized drawing of the concepts e_{max} (a) and e_{min} (b)

Various research has been done on finding a relationship between grain size distribution, particle shape, coefficient of uniformity and the relative density of a granular material (Hatanaka and Feng, 2006)(Cubrinovski and Ishihara, 1999)(Cubrinovski and Ishihara, 2002)(Patra et al., 2010)(Mujtaba et al., 2018). With the (C_u) now known for both types of sand, the next thing to do is to determine the e_{max} - e_{min} range. According to the manufacturer, quartz sand can be categorized as sub-angular sand, which means that according to Youd (Youd, 1973) corresponds with an angularity of 0.25 - 0.35. Angularity was described by Youd as the ratio between the average radius of corners and edges and the radius of the maximum inscribed sphere (mm) of the sand particles. The void ratio can be determined by using the porosity of the two sand layers placed within the containers. By knowing the total volume, which is obtained by multiplying the length and width of the container by the thickness of the sand layer, it becomes straightforward to calculate the volumes of the voids and the solids. The specific values required for this calculation can be found in Table 6.2. With the help of Figure 6.6, e_{max} and e_{min} for both the fine- and coarse sand can be determined. The mean values are given in section B.1. With the use of Equation 6.3.4, the relative density is calculated and is shown in section B.1.

Sand	Total volume [m^3]	Porosity [-]	Volume of solids [m^3]	Volume of voids [m^3]	Void ratio [-]
Fine	0.146	0.37	0.0925	0.0533	0.58
Coarse	0.162	0.42	0.094	0.068	0.72

Table 6.2: Specific density characteristics for the two types of quartz sand used for lab experiments

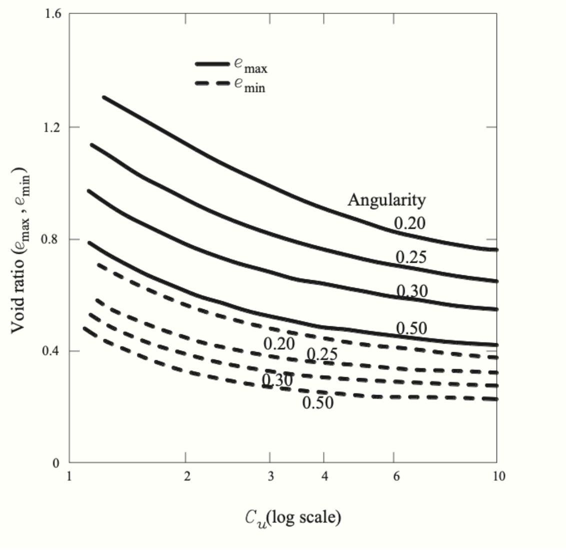

Figure 6.6: Variation of e_{max} and e_{main} with C_u and angularity (Patra et al., 2010).

6.3.5. Angle of internal friction

The net force acting on a penetrating rock, as explained in detail in section 3.3, is primarily dominated by the bearing force exerted by the soil. In this thesis, the Terzaghi formula is used to calculate the ultimate bearing capacity, considering two key soil properties: the effective unit weight and the angle of internal friction.

To validate the two methods utilized for determining the penetration depth, it is essential to determine the angle of internal friction of the sand that is used for experiments. This parameter plays a crucial role in both methods and has a significant impact on the prediction of penetration depth and the overall understanding of the rock-soil interaction.

By assessing the angle of internal friction, the reliability and accuracy of the two methods can be evaluated and compared. The angle of internal friction reflects the shear strength characteristics of the soil and provides valuable insights into the resistance that the soil offers against the penetration of rocks. Therefore, determining the angle of internal friction is of utmost importance in validating the two methods employed for determining penetration depth.

Extensive research has been conducted to explore the connection between the relative density of granular materials and the angle of internal friction. However, these investigations have yielded diverse outcomes and findings. A correlation with a very wide range between relative density and angle of internal friction is given by Meyerhof (Meyerhof, 1956) in Table 6.3

Soil packing	Relative density [%]	Angle of internal friction [$^\circ$]
Loose	20-40	30-35
Medium dense	40-60	35-40
Dense	60-80	40-45

Table 6.3: Correlation between friction angle and relative density (Meyerhof, 1956)

In this thesis, the relationship proposed by Das (Das and Sivakugan, 2016), as illustrated in Equation 6.9, is adopted to establish this correlation.

$$\phi = 25 + 0.18D_r[\%] \tag{6.9}$$

It is necessary however to include a probability density function in the calculation of the angle of internal friction since the empirical relationship between angularity, uniformity coefficient, and void ratio range is derived from numerous laboratory tests. This makes it possible to represent the inherent variability

linked to these parameters more thoroughly.
To incorporate the variability in the range of possible e_{min} and e_{max} values due to the angularity of sub-angular sand (0.25 to 0.35) and account for the deterministic nature of Equation 6.9, Sobol' sampling is used to generate a probability density function (PDF) for the angle of internal friction of both sand types. This allows for capturing the uncertainty and variability in the parameter values.
Because no information is given on the distribution of the angularity values that are associated with sub-angular grains, Sobol' sampling is a suited sampling method since it generates a set of samples that are evenly distributed across the parameter space. For example, e_{min} should lie between 0.43 and 0.5 for the coarse sand type for angularity values between 0.25 and 0.35. Instead of generating random combinations between e_{min}, e_{max} and e, a more uniform coverage of the parameter space is created.

Since multiple empirical relations, assumptions, and experiment averages are used for finding out the angle of internal friction of the two sand types, some form of probability has to be added to the outcome. With the use of Equation 6.3.4, Figure 6.6, Table 6.2 and Equation 6.9, the following probability density function is created for the angle of internal friction for the coarse- and fine sand. The values, distributions, and assumptions that were used for creating Figure 6.7 are given in appendix B.2.

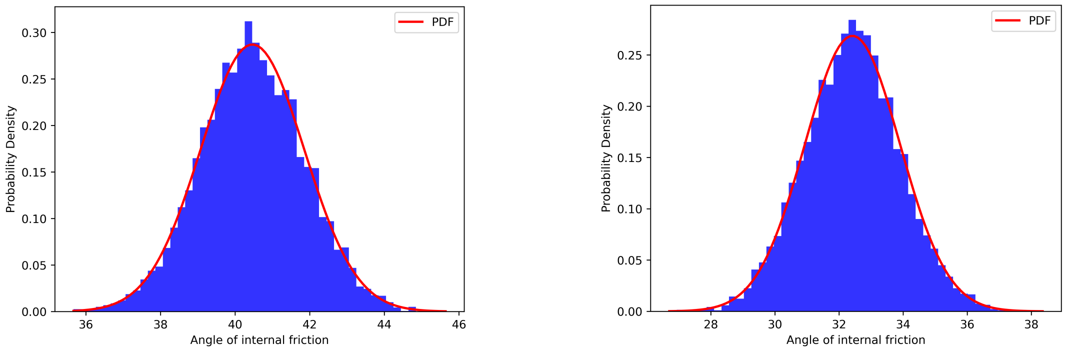

(a) Fine sand. Mean: $40.44°$, standard deviation: $1.39°$

(b) Coarse sand. Mean: $32.42°$, standard deviation: $1.49°$

Figure 6.7: Probability density function for the angle of internal friction.

6.3.6. Unit weight

To establish a relationship between stone size and penetration depth, another essential sand property that needs to be determined is the unit weight of the sand used in laboratory experiments. This can be calculated by considering the density of the sand, the porosity, and the density of fresh water. As mentioned earlier in this chapter, the particle density of quartz sand is kg/m^3. With a porosity of 38% for the fine sand, the bulk density of the fine sand in the container is calculated to be 1643 kg/m^3. However, since the experiments involve fully saturated sand, the weight of the water inside the voids must also be taken into account. The unit weight of saturated fine sand is given in Equation 6.10

$$\gamma_{sand} = 0.62 \cdot \rho_{sand} + 0.38 \cdot \rho_{water} \tag{6.10}$$

The unit weight of saturated coarse sand is given in Equation 6.11

$$\gamma_{sand} = 0.58 \cdot \rho_{sand} + 0.42 \cdot \rho_{water} \tag{6.11}$$

Equation 6.10 and Equation 6.11 lead to a unit weight of 2023kg/m^3 for fine sand and 1957kg/m^3 for coarse sand. All the properties of the two types of sand are displayed in section B.1.

Sand	D_{50}	Mean e_{min}	Mean e_{max}	e	D_r	γ [kg/m^3]	ϕ
Fine	0.17	0.48	0.91	0.58	0.77	2023	40
Coarse	0.51	0.44	0.85	0.72	0.31	1957	32

Table 6.4: Properties of the two types of quartz sand that are used for lab experiments

6.4. Execution

6.4.1. Single stone experiments

As already mentioned in subsection 6.2.1, three variables will be varied during the penetration depth experiments: the fall height, the diameter of the marble, and the grain size of the sand. The experiments are carried out in a structural manner, changing one variable at a time while the other two remain unchanged. First, the marble size and sand properties are kept the same while the fall height, and thus the impact velocity increases. The heights from which the marble is released are 10cm, 30cm, and 50cm. Then, a different marble with a different diameter is used to repeat the experiment. As already mentioned earlier, for each height, a marble is dropped at least three times to minimize measurement errors and the effect of random variations in the impact velocity and bearing capacity of the sand. To minimize boundary effects, the marbles are dropped at the center of the container, although for each repetition the point of impact is shifted a little bit to ensure the marble penetrates a virgin soil. After each sequence of three repetitions, the sand is densified again to ensure similar conditions for each fall height. This ensures that the influence of container edges on the marble's penetration depth is kept to a minimum (Craig and Sabagh, 1994). When all three marbles (D_1 = 6cm, D_2 = 3.5cm, D_3 = 2.5cm) are dropped at least three times from 3 different heights, the test setup is moved to the second container in which the finer sand is placed. Here the experiment is repeated.

Before each drop, the distance between the top of the marble and a reference point (L_1) is measured meticulously with a tape measure. Then the distance between this same reference point and the sand layer is measured (L_2) so that the distance between the bottom of the marble and the sand layer can be determined (Figure 6.8a). This is done using the following formula:

$$H = L_2 - L_1 + D \tag{6.12}$$

After the drop, the distance between the top of the marble and the reference point is measured (L_3). Equation 6.13 is then used to determine the penetration depth.

$$d = L_3 + D - L_2 \tag{6.13}$$

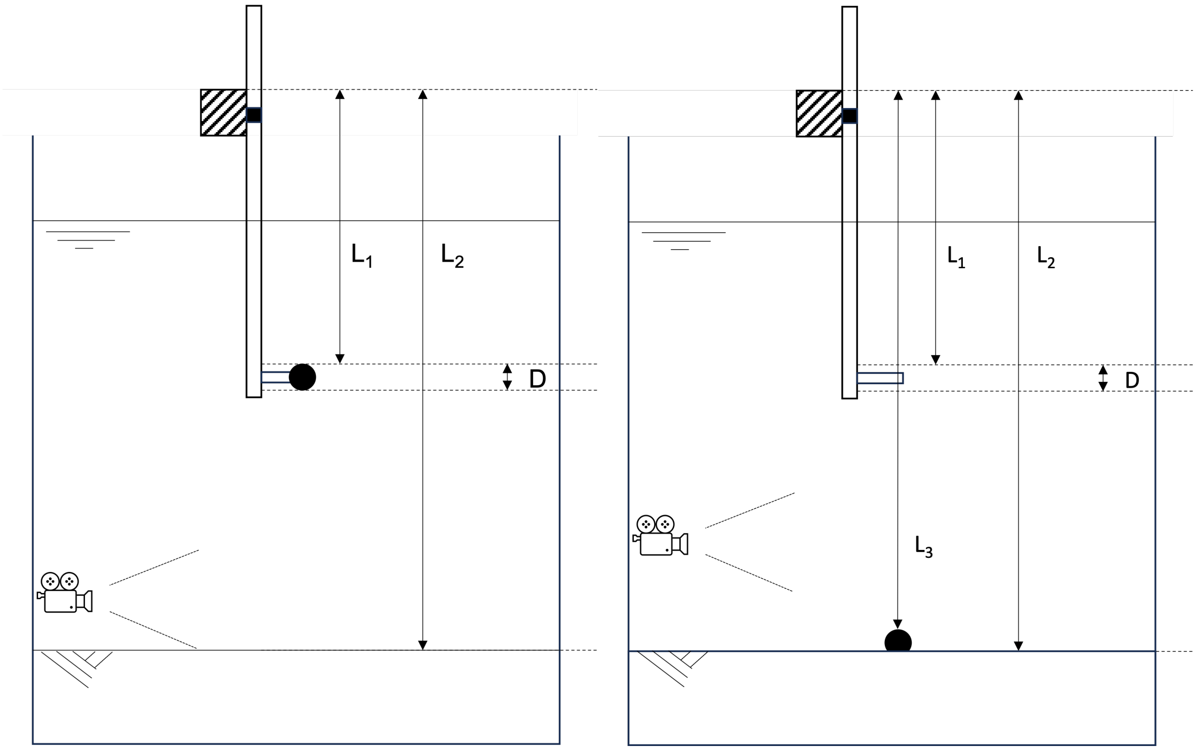

(a) (b)

Figure 6.8: Method for measuring the height of the marble above the sand (a) and the penetration depth (b).

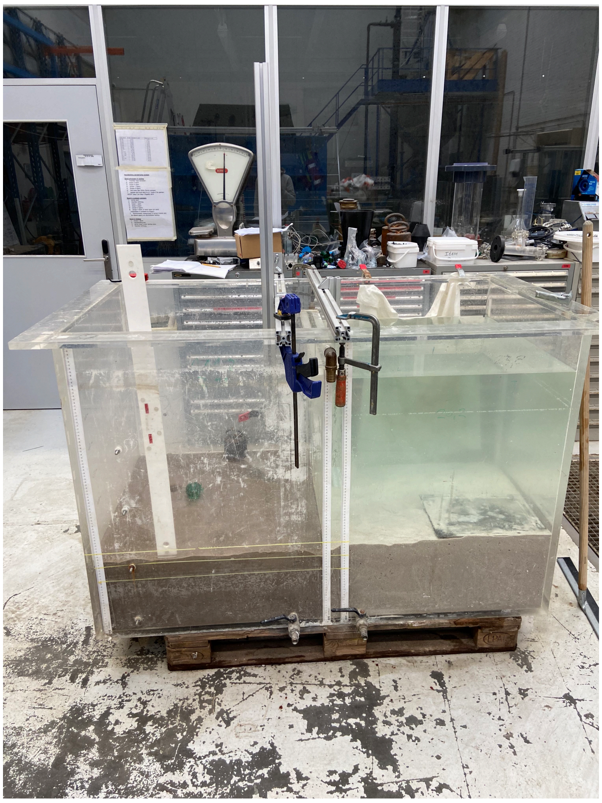

Figure 6.9: Image of the two containers. The left is filled with fine sand, right is filled with coarse sand

Regrettably, during the test runs involving the smallest marble diameter, it became evident that the measurements were highly susceptible to errors. Attempts to measure the distance between the marble's head and the reference point consistently led to the marble being pushed deeper into the sand due to its small size and weight. Consequently, this led to inflated and inaccurate penetration depth values. Thus, the outcomes of the trials involving the smallest marble were excluded from further consideration in this thesis.

6.4.2. Multi-stone experiments

Prior to each experiment, a large marble is released from a height of 50cm, resulting in an initial penetration into the sandbed. Subsequently, the second marble is manually dropped onto the first marble from a height of 40cm. To maintain consistent drop heights, an aluminum bar with an exact length of 40cm is employed. The manual dropping of the second marble is necessary to ensure precise targeting and a direct impact on the first marble. This approach enables more accurate experimentation and reduces the potential for unintended deviations. The decision to drop the second marble from 40cm, rather than 50cm like the initial release, is based on the fact that some test runs point out that the marble's trajectory can get a little unstable after 40cm of descent. This approach increases the reliability and reproducibility of the experiments.

The experimental procedure involves measuring the initial penetration depth before each collision. Subsequently, following each collision between marbles, the additional penetration depth is measured. This process is repeated until no further additional penetration is observed. To ensure accuracy and reliability, the entire cycle is repeated four times.
A schematic visualization of the test setup can be found in Figure 6.10, and photos can be found in section B.3. After each collision, Equation 6.13 is used to determine the additional penetration depth.

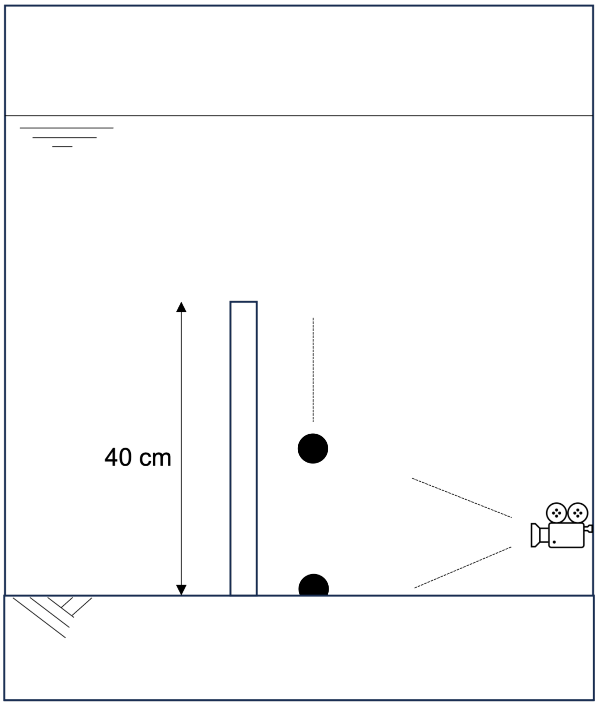

Figure 6.10: Multi stone test setup

7

Results

The purpose of this chapter is to present the results from the laboratory tests that were done and described in chapter 6. Based on the combinations of marble size and sand type, the results will be divided into four groups: large marble with coarse sand, medium marble with coarse sand, large marble with fine sand, and medium marble with fine sand. After the results are presented, a thorough analysis will be carried out to find any patterns or regularities that could facilitate a meaningful comparison of the experimental results with the model results. Finally, the levels of agreement between the three methods' results and the test results will be evaluated.

7.1. Impact velocity determination

As outlined in subsection 6.2.1, the impact velocity of rocks is a variable with significant importance in predicting their penetration depth in sand. Similarly, it is evident that accurately determining the impact velocity of the marble is crucial to establish correlations between marble size, impact velocity, sand properties, and penetration depth.

7.1.1. Theoretical impact velocity

First, the theoretical impact velocity is determined for each marble size and each fall height in order to compare it to the measured impact velocity in a later phase. To determine the impact velocity in an analytical way, van Rhee's Equation 4.1 is used. The equation should be modified from its current form, $m \cdot a = F$ to the form $a = F/m$: This is displayed in Equation 7.1

$$\frac{dv}{dt} = \frac{V_{rock}(\rho_s - \rho_w)g - C_d A_g \frac{1}{2}\rho_w v|v|}{V_{rock}(\rho_s + C_m \rho_w)} \tag{7.1}$$

Equation 7.1 is a differential equation, written in a simpler form in Equation 7.2

$$\frac{dv}{dt} = f(v) \tag{7.2}$$

By using a Python differential equation solver, the acceleration (a(t)), velocity (v(t)), and traveled distance (s(t)) can be determined. Consequently, the impact velocity can be calculated for a given fall height. In Figure 7.1 the impact velocity is plotted against the fall height for the marble with a diameter of 6 cm and for the marble with a diameter of 3.5 cm. Note that the largest marble of the two, the 6 cm marble, is also dropped from 0.2 m height where the smaller marble is not. For a drop height of 0.5m, the 3.5cm marble appears to be nearing its terminal settling velocity, as indicated by the graph. However, the graph of the 6cm marble suggests that it is still accelerating after a fall distance of 0.5. Unfortunately, due to the limitations in container dimensions utilized in the experiments, it is not possible to increase the fall height beyond 0.5m. Further velocity measurements will help ascertain whether the 6cm marble indeed fails to reach its terminal settling velocity.

7.1.2. Measured impact velocity

To establish the correlation between the theoretically determined impact velocity and the penetration depth, it is crucial to validate the accuracy and reliability of the theoretical calculations. This is done with the use of the video footage that was shot of each individual experiment run. The validation process involves analyzing the recorded video footage of each individual experiment run with a software package called "Tracker".

Tracker uses frame rate (FPS) to determine an object's acceleration, velocity, and travel distance (section B.4). Tracker must first be calibrated in order to establish a length scale within the plane of the moving object. During this calibration process, a reference object located in the same plane as the object being analyzed must manually be given a length. As an alternative, the length of the object itself can be used as the calibration length if that length is known. Furthermore, a x- and y-axis will have to be appointed to frame to provide a direction to the measured velocity. Figure 7.2a and Figure 7.2b show both a schematic illustration and a picture of the Tracker software package that is used for the measurement of impact velocity. These images give a clear picture of the procedure and demonstrate how the Tracker program was used to record and examine the impact velocities.

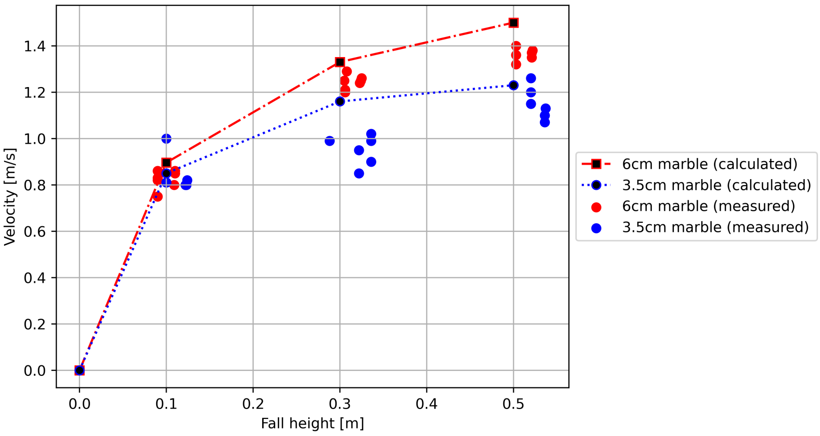

Figure 7.1: The impact velocities of the 6cm marble and the 3.5cm marble, calculated using Equation 7.1 plotted together with the measured velocities.

It is noticeable that the measured velocities of the marbles are slightly lower than the predicted velocities. A possible explanation for this finding is that a wrong drag coefficient (C_D) was used (Equation 4.2). In order to enhance the quantification of volume loss during Subsea Rock Installation (SRI), a high Reynolds number was selected to calculate the drag coefficient. This decision was based on the fact that the water surrounding descending rocks is typically turbulent, resulting in Reynolds numbers exceeding 2000. However, when using marbles as a substitute for larger rocks in simulations, it is plausible that the water surrounding the marbles exists in a transitional state between turbulent and laminar flow. This is due to the marbles' smoother surface compared to rock particles.
A lower Reynolds number would cause a higher friction coefficient (Equation 4.2) and thus a lower settling velocity. Since the impact velocity is now measured for each test run, there is no need to make adjustments to the way impact velocity is determined, the impact velocity can now be used as a variable.

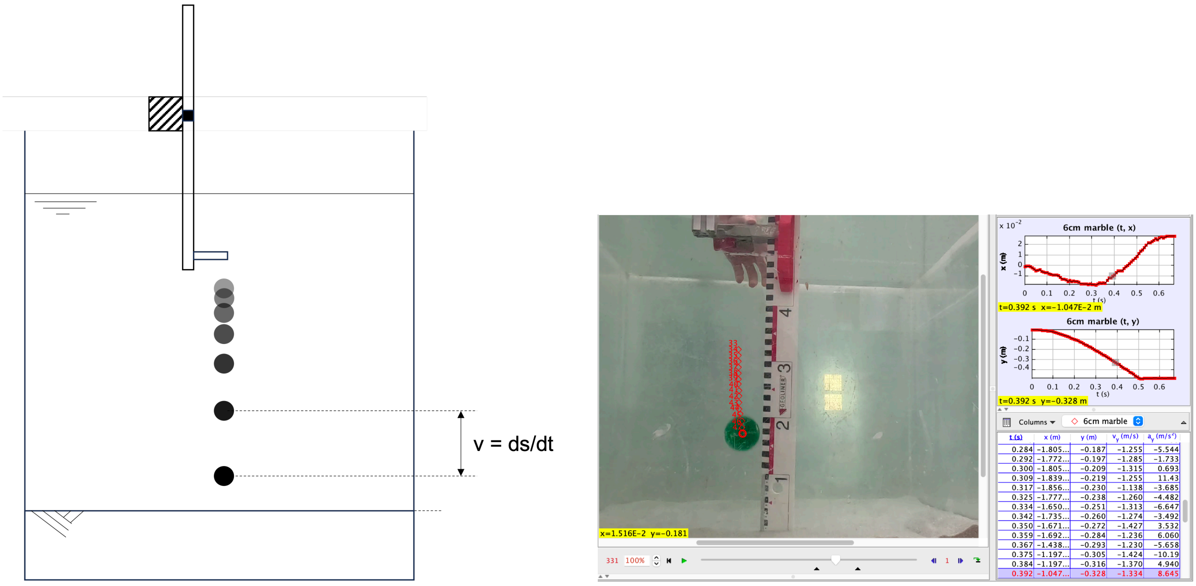

t (s)	x (m)	y (m)	v_y (m/s)	a_y (m/s²)
0.284	−1.805...	−0.187	−1.255	−5.544
0.292	−1.772...	−0.197	−1.285	−1.733
0.300	−1.805...	−0.209	−1.315	0.693
0.309	−1.839...	−0.219	−1.255	11.43
0.317	−1.856...	−0.230	−1.138	−3.685
0.325	−1.777...	−0.238	−1.260	−4.482
0.334	−1.650...	−0.251	−1.313	−6.647
0.342	−1.735...	−0.260	−1.274	−3.492
0.350	−1.671...	−0.272	−1.427	3.532
0.359	−1.692...	−0.284	−1.236	6.060
0.367	−1.438...	−0.293	−1.230	−5.658
0.375	−1.197...	−0.305	−1.424	−10.19
0.384	−1.197...	−0.316	−1.370	4.940
0.392	−1.047...	−0.328	−1.334	8.645

(a) **(b)**

Figure 7.2

7.2. Single stone results

7.2.1. Coarse sand

This chapter's opening section presents and evaluates the findings of an experiment done in coarse sand. This sand type has a relatively high permeability due to its large median diameter size and low coefficient of uniformity. Consequently, it is anticipated that dilatancy will have a noticeable but not particularly pronounced effect.

The measured penetration depths for the large- and medium marble in coarse sand are shown in Table 7.1 and Table 7.2 respectively. These penetration depths are also plotted against the impact velocity in Figure 7.4, where the results for the large- and medium marble are combined into one graph. As indicated in Table 7.1, the measured penetration depth exhibits an accuracy of 1mm. This level of precision is due to the use of a tape measure, which was accurate up to 1 mm. The tracking software "Tracker" returns the velocity of the marbles with an accuracy of 1cm/s.

Run	Marble diameter [cm]	Drop height [cm]	Impact velocity [m/s]	Penetration depth [cm]
1	6	9	0.82	0.5
2	6	9	0.83	0.7
3	6	9	0.86	0.7
4	6	9	0.75	0.7
5	6	30.5	1.25	1.1
6	6	30.6	1.20	1.4
7	6	30.6	1.29	1.5
8	6	30.8	1.21	1.5
9	6	50.3	1.4	1.3
10	6	50.3	1.36	1.6
11	6	50.3	1.32	1.6

Table 7.1: Results for the large marble lab tests in coarse sand. ϕ sand = 32°

Run	Marble diameter [cm]	Drop height [cm]	Impact velocity [m/s]	Penetration depth [cm]
12	3.5	10	0.81	0.7
13	3.5	10	0.81	0.6
14	3.5	10	0.85	0.7
15	3.5	32.2	1	0.5
16	3.5	32.2	0.95	0.5
17	3.5	28.8	0.99	0.7
18	3.5	52	1.2	0.9
19	3.5	52.8	1.26	1.1
20	3.5	52	1.15	1.2

Table 7.2: Results for the medium marble lab tests. ϕ sand = $32°$

For both the large and medium marbles, Figure 7.3a shows a more or less linear relationship between penetration depth and impact velocity. Notably, for velocities higher than 1 m/s, it is clear that the large marble penetrates the sand more deeply than the medium marble for identical impact velocities (one exception at 1.25 m/s). This finding is consistent with the idea that an object that is heavier has more momentum and kinetic energy than an object that is lighter when they move at similar velocities. In addition, the larger marble in this scenario not only weighs more but also has a larger surface area, allowing the ground to exert more upward pressure for a similar depth and, as a result, a greater bearing force.

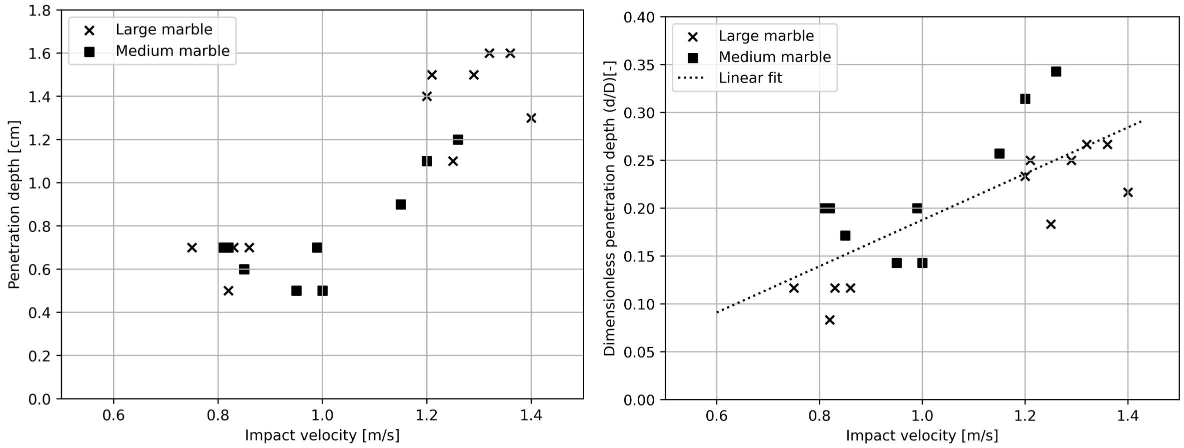

(a) **(b)**

Figure 7.3: Results for the large- and medium marble lab tests combined, plotted against the impact velocity. ϕ sand = $32°$

In order to better examine the impact of the impact velocity, Figure 7.3b plots the impact velocity against the dimensionless penetration depth (d/D). The fitted graph that is drawn through the experiment results supports the suggestion that the relationship between impact velocity and penetration depth is linear. It's interesting to note that over the entire range of impact velocities, the 3.5 cm marble consistently achieves a deeper dimensionless penetration depth. It is important to remember that this discrepancy might be related to measurement errors made when determining the penetration depth of the medium marble.

The accuracy of the medium marble is less precise than the large marble when measuring the distance between the top of the marble and the reference point, as shown in Figure 6.8b. Errors can occur if the tape measure is not placed precisely at the marble's highest point or if the measurements are taken incorrectly. Even though these sources of error are the same for both marbles, pressing the tape measure's tip against one of them to find its highest point causes more penetration due to the force used. Significantly, compared to the large marble, the medium marble experiences a greater increase in penetration depth as a result of the added force.

Consequently, this discrepancy may contribute to the higher values observed for the dimensionless penetration depth of the medium marble.

7.2.2. Fine sand

The measured penetration depths for the large- and medium marble in fine sand are shown in Table 7.3 and Table 7.4 respectively. These penetration depths are also plotted against the impact velocity in Figure 7.4, where the results for the large- and medium marble are combined into one graph.

Run	Marble diameter [cm]	Drop height [cm]	Impact velocity [m/s]	Penetration depth [cm]
21	6	11	0.85	0.2
22	6	10.9	0.8	0.2
23	6	11	0.86	0.2
24	6	32.3	1.24	0.4
25	6	32.5	1.26	0.4
26	6	32.4	1.25	0.5
27	6	52.2	1.38	0.5
28	6	52.1	1.35	0.3
29	6	52.1	1.37	0.3

Table 7.3: Results for the large marble lab tests. ϕ sand = $40°$

Run	Marble diameter [cm]	Drop height [cm]	Impact velocity [m/s]	Penetration depth [cm]
30	3.5	12.2	0.82	0.3
31	3.5	12.3	0.8	0.2
32	3.5	12.4	0.8	0.2
33	3.5	33.6	0.99	-
34	3.5	33.6	0.9	-
35	3.5	33.6	1	-
36	3.5	53.6	1.10	0.3
37	3.5	53.7	1.13	0.3
38	3.5	53.6	1.07	0.5

Table 7.4: Results for the medium marble lab tests. ϕ sand = $40°$

Unfortunately, due to measurement errors, the penetration depth for runs 33 to 35 was incorrectly recorded, resulting in negative values. Obviously, such negative values are physically impossible as they would imply that the marble remains suspended above the sand after penetration. Consequently, these results are deemed unreliable and have been excluded from further analysis and consideration in this thesis.

The (dimensionless) penetration depth is once again plotted against the impact velocity.

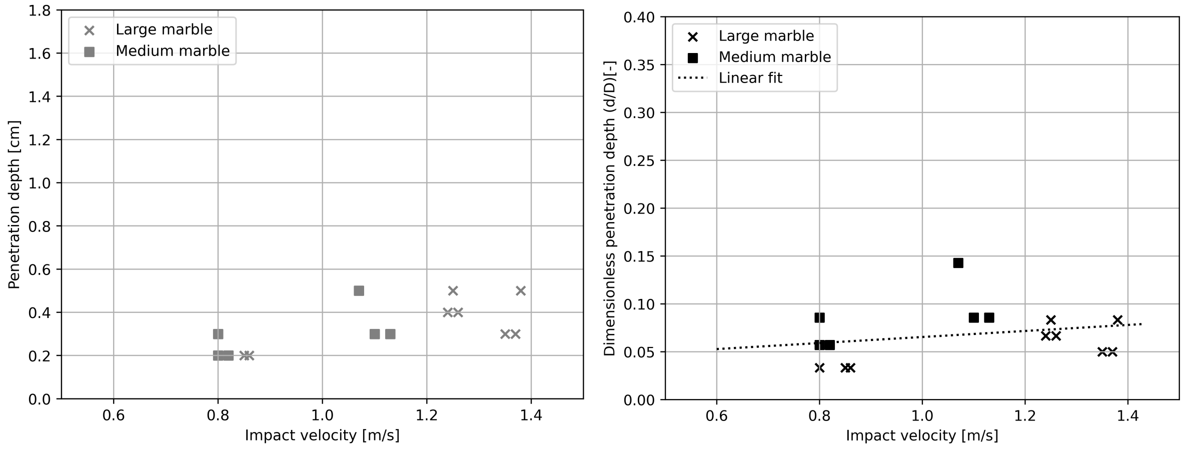

(a) **(b)**

Figure 7.4: Results for the large- and medium marble lab tests combined, plotted against the impact velocity. ϕ sand = $40°$

In contrast to the findings in coarse sand, the experiments in fine sand reveal no significant difference in the absolute penetration depth between the medium and large marble, despite the impact velocities being lower for the medium marble. When examining the dimensionless penetration depth, it becomes clear that the values for the medium marble are occasionally twice as high as those for the large marble.

During the analysis of the video recordings of the penetrations, an interesting observation emerges regarding the behavior of fine sand. Unlike the behavior observed in coarse sand, the fine sand appears to exhibit elastic characteristics during the penetration process.
A notable pattern becomes apparent as the marble penetrates the fine sand. At the halfway point of penetration, the depth achieved is greater than at the final stage. Figure 7.5 shows the location of the center of the marble during impact. The marble penetrates, rebounds, and then re-penetrates at a shallower depth. This phenomenon can be attributed to variations in water pressure within the pores of the fine sand structure.
Due to the densely packed nature of fine sand, the process of shearing between the sand grains is influenced by dilatancy. As the penetrating marble induces shear forces among the grains, the water pressure within the pores experiences a drop, resulting in an increase in effective stress, as is explained through Equation 3.30. Consequently, the fine sand exhibits significantly enhanced resistance to penetration compared to its behavior prior to the shearing event.

This behavior suggests that the fine sand acts as a medium that not only hinders penetration but also appears to store some of the kinetic energy of the penetrating marble.

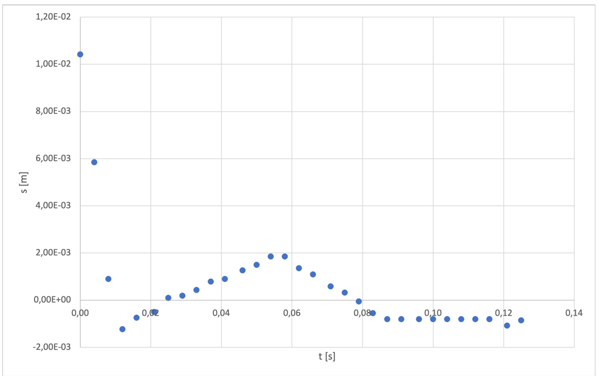

Figure 7.5: Location (s) of the marble plotted against time (t) during impact.

7.3. Multi-stone results

Four tests are executed to assess the dynamics of, and additional penetration due to multi-stone collisions. Each test consists of the number of runs that are needed before no additional penetration is observed. First it must be determined what type of collision it is that takes place on the sand bed, plastic or elastic. When this is done, the impact velocity and additional penetration can be determined.

7.3.1. Additional penetration

In the table below (Table 7.5), each additional penetration as a result of a marble hitting a marble that is already partially embedded in the sand is shown. Each time, the second marble is released from 40cm above the sand bed and strikes the marble on the bed with a velocity that is approximately 1.2 m/s.

Run	IP [cm]	V_1[m/s]	AP_1[cm]	V_2[m/s]	AP_2[cm]	V_3[m/s]	AP_3[cm]	V_4[m/s]	AP_4[cm]
1	1.6	1.25	0.2	1.2	0.1	1.25	0	-	-
2	1.6	1.23	0.2	1.19	0.1	1.22	0.1	1.22	0
3	1.8	1.25	0.2	1.22	0.1	1.25	0	-	-
4	1.9	1.24	0.1	1.28	0.1	1.23	0	-	-

Table 7.5: Additional penetrations due to marble collisions. IP = initial penetration, V_i = impact velocity at the i th collision, AP_i = additional penetration as a result of the i th collision.

In three of the four runs there is no additional penetration after 2 collisions. Only in run 2, three collisions are required before no additional penetration is observed. In reality, stones will collide at terminal settling velocity, which is not the case during this experiment. The terminal settling velocity for the marble (D = 6cm) that was used during this experiment is approximately 1.5 - 1.6 m/s if we extrapolate Figure 7.1, so this experiment was not perfectly scaled. However, we can still use the kinetic energy and momentum to analyze the additional penetration depth as a result of the collision. This will be done in Part IV.

7.3.2. Collision dynamics

The video recordings of the marble collisions were meticulously analyzed to gain insights into the collision dynamics. Upon examination, several observations can be made regarding the behavior of the marbles before and after the collisions.

When the collision is centered or centric, it becomes evident that Marble 2 experiences a complete loss of momentum. This can be observed by the fact that Marble 2 comes to a complete stop immediately after the collision before gravity gradually takes hold of it and initiates its deceleration toward the ground. The sudden halt of marble 2 indicates a significant transfer of momentum to marble 1.

On the other hand, marble 1 demonstrates an acceleration following the collision due to the gained momentum. However, due to the immediate deceleration caused by the opposing force exerted by the soil, it becomes challenging to directly observe the preservation of kinetic energy. The opposing force from the soil acts as a decelerating factor on marble 1, making it difficult to discern the conservation of kinetic energy in isolation.

Nevertheless, it is important to note that momentum is always conserved within the system during a collision. This principle ensures that the total momentum before the collision is equal to the total momentum after the collision, regardless of the specific energy transformations or losses that may occur.

Based on these observations, it can be assumed that the momentum lost by marble 2 is transferred to marble 1 during the collision. The transfer of momentum between the marbles plays a crucial role in the overall dynamics of the collision process.

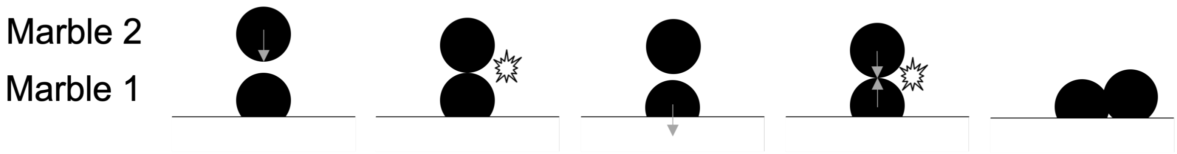

Figure 7.6: Different stages of the marble collision, showing the process as described in the text above.

Again, some sort of elastic behavior by the soil is observed. Initially, marble 1 experiences an acceleration in its downward motion immediately after the collision. However, this acceleration is subsequently counteracted by the increasing upward force exerted by the bearing force from the soil and, to a lesser extent, a friction force. As a result, marble 1 undergoes deceleration during its descent.
Meanwhile, marble 2 begins moving downward again after it has lost all of its momentum in the collision, leading to a second collision between the marbles.

Towards the end of the collision sequence, it becomes apparent that the additional penetration depth of marble 1 is less than what was observed shortly after the initial collision. This decrease in additional penetration depth suggests that the elastic behavior of the soil, combined with the interaction between the marbles, leads to energy transfers and redistributions within the system.

To visually illustrate these findings, a diagram depicting the displacement (s) and time (t) of the collision is presented in Figure 7.7, highlighting the positions of marble 1 and marble 2 throughout the collision sequence. For both marbles, s = 0 corresponds to their position at the time of the first contact between the marbles.

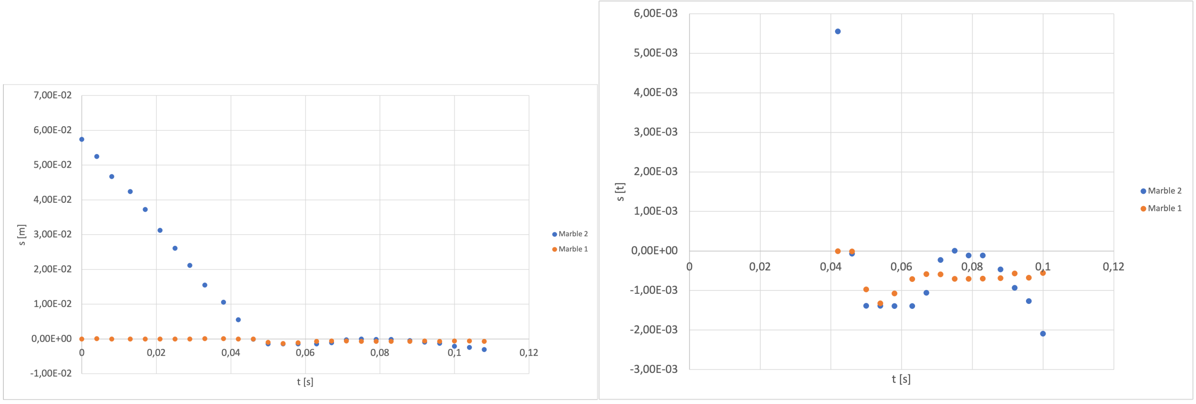

(a) **(b)**

Figure 7.7: The location (s) plotted against time (t) for both Marble 1 and 2, extracted using Tracker.

Figure 7.7b shows the positions of Marble 1 and 2 during the phase in which the collision is happening. It can be seen that the two marbles move downward together during the first part and then move upward again, indicating that the sand underneath them behaves like a spring. It can also be seen that Marble 2 (blue) springs all the way to its position at the moment of first contact.
As already mentioned earlier, the additional penetration depth at the end of the collision sequence is less than it is shortly after the collision. This is also visible in Figure 7.7b. The additional penetration depth after 0.1 seconds is less than half of the penetration depth after approximately 0.055 seconds.

So why is this elastic behavior observed during a collision between two marbles in coarse sand, but not during single stone penetration in the same sand? It is assumed that this is again the result of a drop in pore pressures in the sand due to the dilatancy of the sand grains. Since the first marble is already partially embedded in the sand, it is more difficult for the water at the boundary layer between the water and the sand to reach the pores in the shear zone, causing a drop in pressure as soon as the sand particles start shearing. It is unknown of course if the pore volume increases or decreases during shearing since no volume increase or decrease is measured and no pressure gauges were used during the experiment. However, if the pore volume would decrease, the water pressure in the pores would increase, leading to a lower effective stress and thus a drop in bearing capacity. That would not coop with what is observed during the experiments and thus a volume increase is assumed.

Part IV

Validation

8

Validation of the single stone penetration model

This chapter presents the comparison between the results of the laboratory experiments and the outcomes of the model developed based on the theoretical framework described in Part II. The main objective is to validate the model by conducting a thorough analysis of the similarities and discrepancies between the experimental data and the model predictions. Any irregularities observed during the comparison will be carefully investigated and explained. If necessary, adjustments will be made to the model to improve its accuracy and reliability.

8.1. Validation in coarse sand

First, the model outcomes will be compared to the experiment results that were executed in coarse sand (DORSILIT® nr.8 (section 6.3)). Modeling the reaction of coarse sand to penetration is expected to be more straightforward compared to fine sand. This is attributed to the reduced impact of pore pressures in coarse sand, primarily due to its higher permeability. The increased permeability allows water to escape from, or enter the pores more readily, making it easier to examine the effects of pressure increase resulting from penetration (Terzaghi & Brinch Hansen) and inertial drag since the effect of dilatancy is expected to be limited. In contrast, fine sand may exhibit greater complexities due to enhanced pore pressure influence.

Table 8.1 provides an overview of the different approaches used to calculate the penetration depth of individual stones, which will be compared to the test results of coarse sand, presented in subsection 7.2.1. A detailed description of each method can be found chapter 4.

#	Name	Type of equation
1	Miedema (2021)	Algebraic
2	Work-Energy	ODE
3	Impulse-Momentum	ODE
4	Work-Energy-Miedema	ODE
5	Impulse-Momentum-Miedema	ODE

Table 8.1: An overview of the different methods to calculate the penetration depth.

It should be noted that for methods 2 to 5, the bearing force will be calculated using both Terzaghi's method and the method proposed by Brinch Hansen. Consequently, each of these methods will yield two outcomes, one for each approach to determining the ultimate bearing force. This yields the total number of methods to nine. Table 4.1 displays the abbreviations of the nine methods, which will help to simplify their representation and facilitate clear and concise communication of the results. Figure 8.1 presents the relationship between the calculated penetration depth and the impact velocity for the large marble (D = 6cm, density = 2430 kg/m^3). The experimental data collected during the experiments is also depicted on the graph, along with a linear fit through the data. To ensure clarity in a plot containing 9 graphs, different methods are categorized by color and line style. Methods utilizing Terzaghi's formula for ultimate bearing capacity are represented by a tint of brown/red, while methods employing Brinch Hansen's formula are represented by a tint of green. Additionally, methods where the cross-sectional area and effective width depend on the depth (z) are displayed using a dotted line, whereas methods utilizing Miedema's approach with a preset cross-sectional area and effective width are represented by a dash-dotted line (-.).

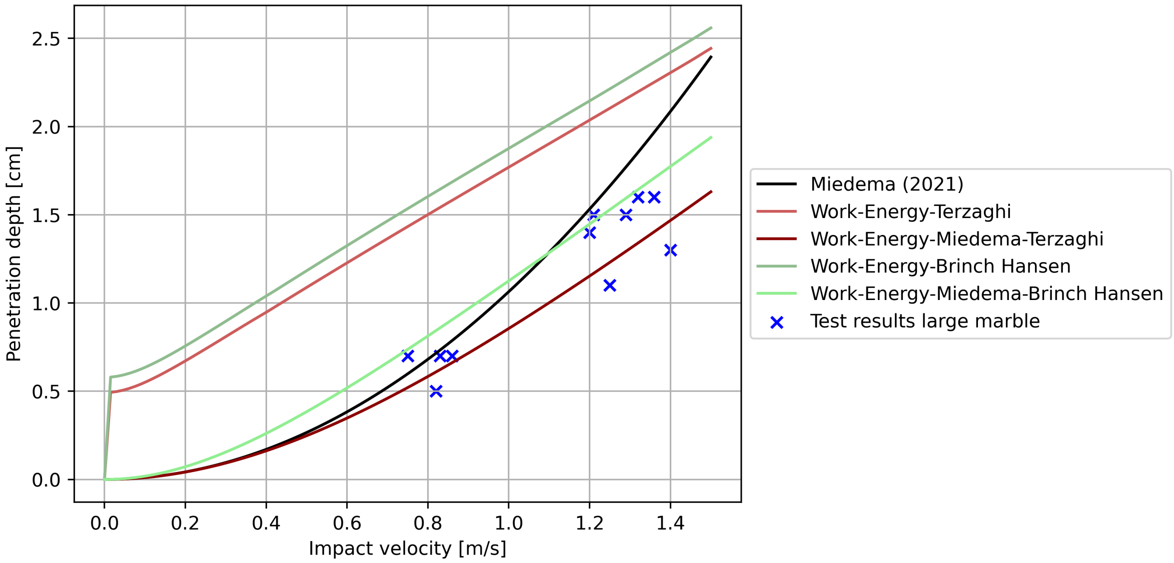

Figure 8.1: All methods plotted together with the test results for the large marble in coarse sand ($\phi = 32°$).

It should be noted that only 6 graphs seem to be visible in Figure 8.1, while the legend mentions 10 lines. This is due to the fact that the the Work-Energy method and the Impulse-Momentum method yield the same outcomes when identical methods are used for estimating the ultimate bearing capacity and efffective- area and width. This is why these graphs are plotted on top of each other, showing only 6 lines where there are actually 10 lines are plotted.

Figure 8.1 illustrates that the 'Work-Energy-Miedema-Terzaghi'(WEMT) method exhibits the closest agreement with the experimental data. This method corresponds to an approach that employs an ordinary differential equation (ODE) to calculate the penetration depth (d). The method uses the Terzaghi method for determining the ultimate bearing capacity, and combines elements of both the static and numerical methods for calculating the effective area and the effective width of the marble (chapter 4). From the fact that all the methods result in graphs with the same slope angle (except for the Miedema2021 method), it can be concluded that the approach for determining the effective area and effective width has a huge influence on the penetration depth at very low impact velocities (around 0m/s) but it does not influence the amount of penetrated centimeters per m/s. The methods employing a static approach to estimate the effective area and effective width consider d $\approx$ 0 when the impact velocity is 0 m/s, assuming that the effective area and effective width are sufficient to support the marble's weight. On the other hand, the methods that update $A_{effective}$ and W as z increases take into account an initial penetration depth of approximately half a centimeter. This is because with this approach an initial penetration depth is computed for which there is a balance between the bearing force, buoyancy force, and gravity force, resulting in a more realistic estimation. However, a drawback of these methods is that they tend to overestimate the penetration depth of the large marble by approximately 0.75 to 1 cm, resulting in an error of nearly 100%.

Among the methods compared in Figure 8.1, the Miedema (2021) method stands out as the only one producing an exponential graph. This distinctive shape arises from the fact that the drag force is not taken into account in this particular method. The Miedema method is based on a simplified

equation, $d = E_{\text{kinetic}}/F_{\text{net}}$, where the kinetic energy increases quadratically with the impact velocity. Consequently, this quadratic relationship between impact velocity and penetration depth is observed in the graph. In contrast, the other methods consider an increasing F_{net} as z increases and account for the drag force, which is a function of v^2.
Finally, it is interesting to see that the WEMT method follows the Miedema method for an impact velocity of 0 - 0.5 m/s. When the impact velocity further increases, the added bearing force as a result of an increasing z results in a linear progression of the graphs.

In Figure 8.2 the results for all methods are plotted together with the results of the experiments that were carried out using the medium marble (D = 3.5cm, density = 2430 kg/m^3). The results are similar to those regarding the large marble. The best fit is again provided by methods that use a static value for the effective area and effective width while assuming an increasing magnitude for the bearing force for an increasing z.

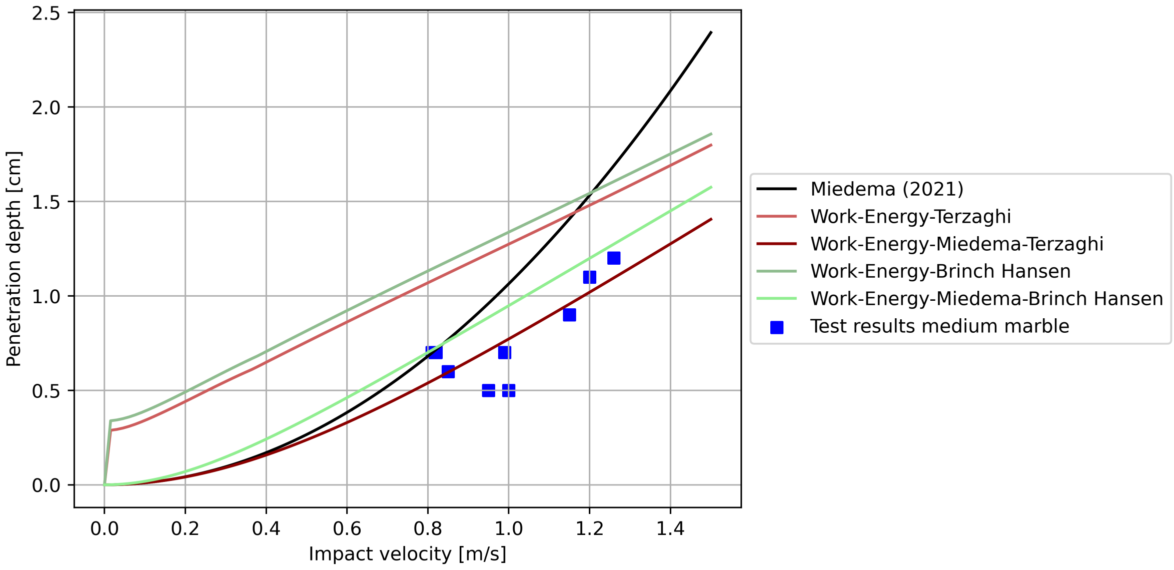

Figure 8.2: All methods plotted together with the test results for the medium marble in coarse sand ($\phi = 32°$).

From the analysis of Figure 8.1 and Figure 8.2, it can be deduced that the WEMT method exhibits the closest match to the laboratory test results, both for the large marble tests and the medium marble tests. To further evaluate the accuracy of this method, a relative error can be computed by comparing their outcomes with the corresponding test results for similar impact velocities.
By calculating the relative error, the deviation between the predicted penetration depths using the WEMT method and the actual penetration depths measured in the laboratory experiments can be quantified. This relative error provides a quantitative measure of the discrepancy between the model predictions and the experimental data.
The relative error is calculated using the formula in Equation 8.1

$$\text{Relative error}[\%] = \frac{\text{Model output} - \text{experiment data}}{\text{experiment data}} \cdot 100 \tag{8.1}$$

A model that provides the best fit must strike a balance between underestimating and overestimating the penetration depth for various impact velocities because the data from the laboratory experiments show some degree of scatter. By doing this, the outcome graph that is produced can show a consistent average that closely matches the test results. As a result, it follows that the best-case scenario would result in a mean relative error of 0%, showing that, on average, the model predictions match the measured penetration depths exactly.

The WEMT method calculates the penetration depth for the large marble in coarse sand with a relative error of -1.52%. This means that this method underestimate the mean of the test results by less

than 2%, which is quite satisfactory.
For the medium marble tests in coarse sand, the WEMT method calculates the penetration depth with a relative error of 11.88%. It can thus be said that the models match the large marble results better than the medium marble results. The method that was used to determine the relative errors as well as the relative errors for each individual impact velocity can be found in section C.1.

8.2. Validation in fine sand

In the upcoming analysis, the model outcomes will be compared to the experimental results obtained in fine sand (SIBELCO M34 (section 6.3)). It is anticipated that modeling the reaction of fine sand to penetration will be more intricate compared to coarse sand. This complexity can be attributed to the heightened influence of pore pressures in fine sand, primarily resulting from its lower permeability. The reduced permeability restricts the movement of water within the pores, resulting in a more pronounced effect of dilatancy. As a consequence, the behavior of fine sand during penetration is expected to exhibit distinct characteristics compared to coarse sand.

The test results for the experiments conducted in fine sand were previously discussed in subsection 7.2.2 and are now presented alongside the model outcomes in Figure 8.3 As anticipated, the 'Work-Energy' and 'Impulse-Momentum' methods overestimate the penetration depth. This can be attributed to the fact that these methods do not consider the reinforcing effect of dilatancy on the saturated sand. Dilatancy, a phenomenon characterized by increased stiffness and strength in saturated soils, plays a significant role in fine sand, leading to a more substantial resistance to penetration. By neglecting this strengthening effect, the 'Work-Energy' and 'Impulse-Momentum' methods yield higher predictions for the penetration depth.
Again, the models that work with a preset value for the effective width and effective area fit the test results accurately. It can be concluded that overestimating the effective width and effective area of the marble/stone seems to account for the effect of dilatancy.

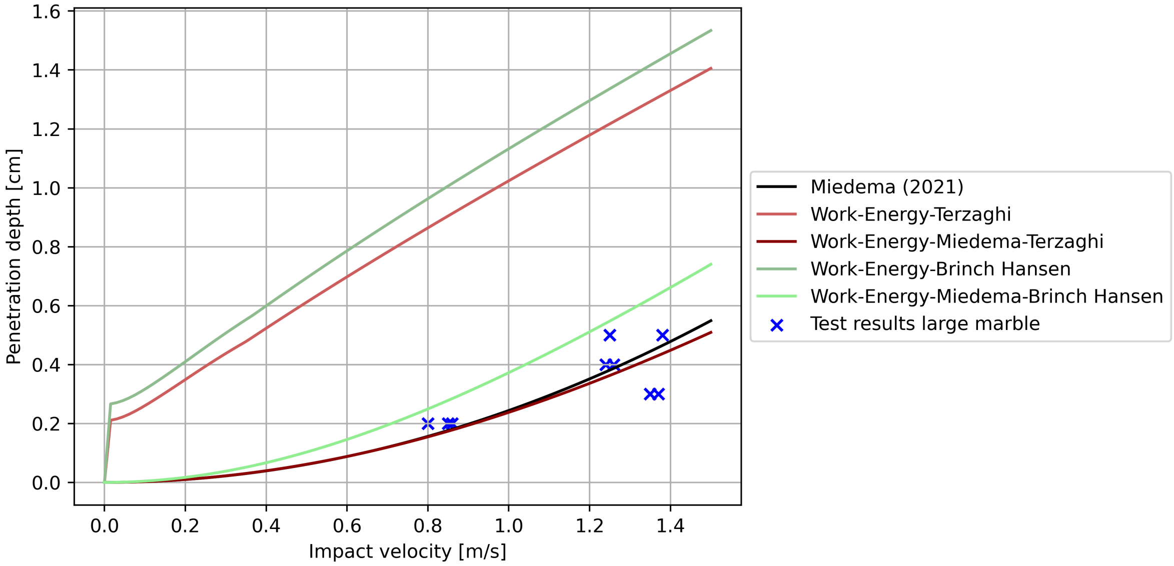

Figure 8.3: All methods plotted together with the test results for the large marble in fine sand ($\phi = 40^{\circ}$).

The same holds again for the outcomes of the model for the medium marble in fine sand (Figure 8.4). This time, the static methods that use the Brinch Hansen formula for estimating the ultimate bearing capacity seem to fit the data better than the methods that use Terzaghi.

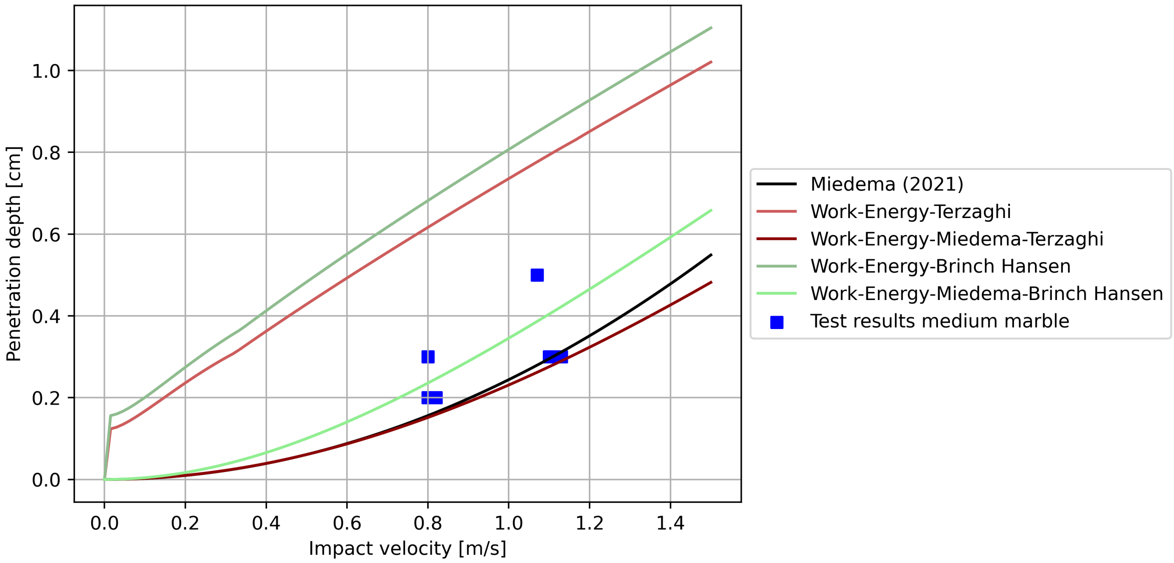

Figure 8.4: All methods plotted together with the test results for the medium marble in fine sand ($\phi = 40°$).

The relative error is once again calculated for both the Work-Energy-Miedema and the Impulse-Momentum-Miedema methods, however, this time both the Terzaghi as well as the Brinch Hansen models are evaluated.

For the method that use the Terzaghi equation to calculate the ultimate bearing capacity of the soil, the WEMT method yields a relative error of 5.15%. For the medium marble the relative error is -19.82%. The method that uses Brinch Hansen seemed to match the test data better than the Terzaghi method for the medium marble situation. However, the relative error is only slightly lower: 19.65% for the WEMBH method. The relative error for each impact velocity can be found in section C.1.

8.3. Probabilistic approach

Up until now, the model validation process has relied on a fixed value for the angle of internal friction, both for coarse sand and fine sand. However, as discussed in subsection 6.3.5, the exact angle of internal friction for the sand remains somewhat uncertain, prompting the introduction of two normal distribution scenarios to address potential variations. These two normal distributions are shown again in Figure 8.5.

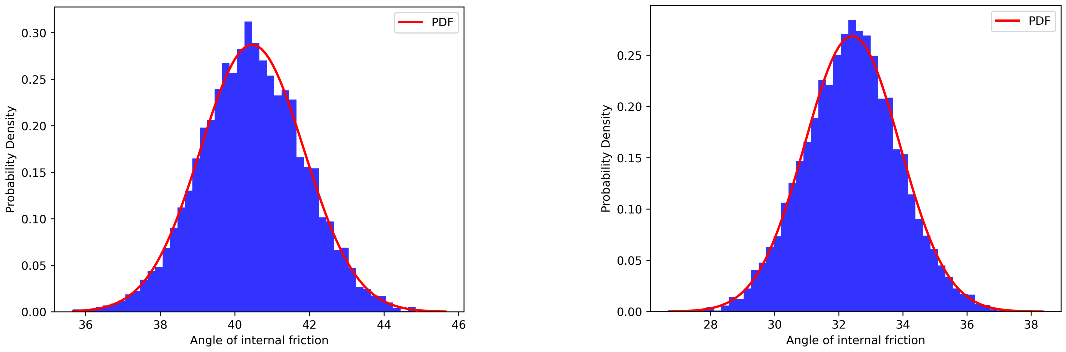

(a) **(b)**

Figure 8.5: Probability density function for the angle of internal friction of the fine- (a) and coarse sand (b) that is used during lab experiments. Mean: $40.44°$ (a), $32.42°$ (b) standard deviation: $1.39°$(a), $1.49°$ (b)

To integrate this normal distribution into the WEMT model, the penetration depth for each impact velocity recorded during the lab tests is recalculated. However, this process is repeated 1000 times, each time utilizing a distinct angle of internal friction randomly drawn from the normal distributions illustrated in Figure 8.5. This procedure enables the establishment of a 90% confidence interval, effectively indicating the range within which the actual penetration depth is most likely to fall.

It turns out that when this method is applied, almost all test results are within the model's 90% confidence interval. This method eliminates the impression that a falling rock's penetration depth can be precisely calculated. After all, the test results also show that similar circumstances can have various effects. As a result, it is correct to provide a range within which the outcome is most likely to fall rather than a single result for the penetration depth of a stone. Figure C.16 displays the outcome of this approach when combined with the WEMT method. In this instance, it relates to the experiment using a large marble and coarse sand. The outcomes for the medium marble in coarse sand, the large marble in fine sand, and the medium marble in fine sand can be found in section C.6.

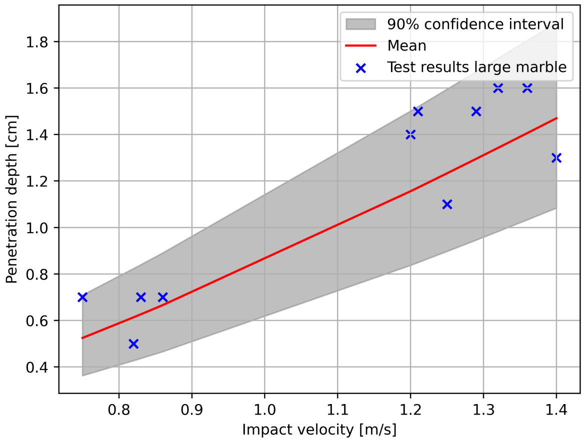

Figure 8.6: Figure showing the 90% range for the penetration depth when the angle of internal friction is picked from Figure B.6b

8.4. Conslusion

By comparing the correlation between the penetration depths of marbles of various sizes, it is possible to successfully relate the experimental data from the marbles, employed as a way to simulate the penetration of stones into a submerged sand layer. If the dimensionless penetration depth shows a linear relationship when it is plotted against the impact velocity on the horizontal axis, it means that the two variables are more or less correlated linearly. In other words, it can be anticipated that the dimensionless penetration depth will rise according to the impact velocity. We can conclude from Figure 7.3b and Figure 7.4b that this is indeed the case. Together with the fact that the WEMT- and the IMMT fit the data from the lab test well for both marble sizes, it can be assumed that the marble experiment results can be extrapolated to real-world scenarios involving stone penetration into submerged sand. The same conclusion was drawn by Beemsterboer (Beemsterboer, 2013) when he studied the dimensionless penetration of steel spheres in clay.

From comparing the outcomes of the different methods for calculating the penetration depth of glass marbles with the actual experiment data can be concluded that using a combination of the method of Miedema and the numerical Work-Energy method is the best choice for calculating the penetration depth of individual rocks during subsea rock installation.

9

Validation of the multi-stone model

Chapter 5 introduced a simplified theory proposed by Beemsterboer (Beemsterboer, 2013), which aimed to describe additional penetration of rocks resulting from rock-rock interactions at the seafloor. He assumed that all energy and momentum were conserved during the collision, which was fully plastic in nature.

It is important to note that Beemsterboer's theory primarily focused on rock penetrations in clay, and its applications to other soil types, such as sand, require further validation.

During laboratory experiments, that are described in subsection 6.2.2 and section B.3, marbles were used as proxies to model the collisions of rocks on the seafloor during subsea rock installation. The additional penetration of these collisions was measured and each collision was recorded and meticulously analyzed to gain insight into the physics of particle collision on sandbeds.

Section 7.3 shows the results of the multi-stone experiments and a description of how the dynamics of underwater collisions work. In this chapter, the theory by Beemsterboer is validated against lab test data in sand with the goal to assess the applicability of Beemsterboer's theory in estimating volume losses during subsea rock installation.

9.1. Validation in course sand

In the application of Beemsterboer's theory to the WEMT method, it is assumed that the collision is fully plastic, although it has been concluded in section 7.3 that this assumption may not hold true in the actual experimental conditions. Specifically, with each collision, the impact velocity is divided by i+1, where i represents the collision index. This adjustment is based on the assumption that all momentum is conserved during the collision process. However, as observed from the experimental findings discussed in section B.3, the collisions exhibit elastic behavior to some extent, which challenges the assumption of full plasticity.

The initial conditions to calculate the single stone penetration depth were as follows:

$$\begin{aligned} v_{z=0} &= v_0 \\ z &= 0 \end{aligned} \tag{9.1}$$

To calculate the penetration depth after collision i, the impact velocity that was measured for collision i is divided by i + 1 and the initial value for z is equal to the penetration depth as a result of collision i - 1. The reason for this is that marble 2 will begin the additional penetration already partly embedded in the sand, with a velocity that is less than the impact velocity of marble 1 due to the conservation of momentum. This leads to the following initial conditions:

$$\begin{aligned} v_z &= \frac{v_i}{i+1} \\ z &= z_{i-1} \end{aligned} \tag{9.2}$$

To validate the results for run 1 for example, the initial conditions for the first collision would be

$$\begin{aligned} v_z &= \frac{1.25}{2} \\ z &= 1.6\text{cm} \end{aligned} \tag{9.3}$$

When these conditions are applied to each collision for each run, the results that are supplied by the model can be compared to the data that was gathered during the lab tests. The results are shown in Figure 9.1. Only the WEMT method is shown since this method matched the data from the single stone lab tests most accurately, together with the IMMT method. For clarity however, only one method is plotted in Figure 9.1.

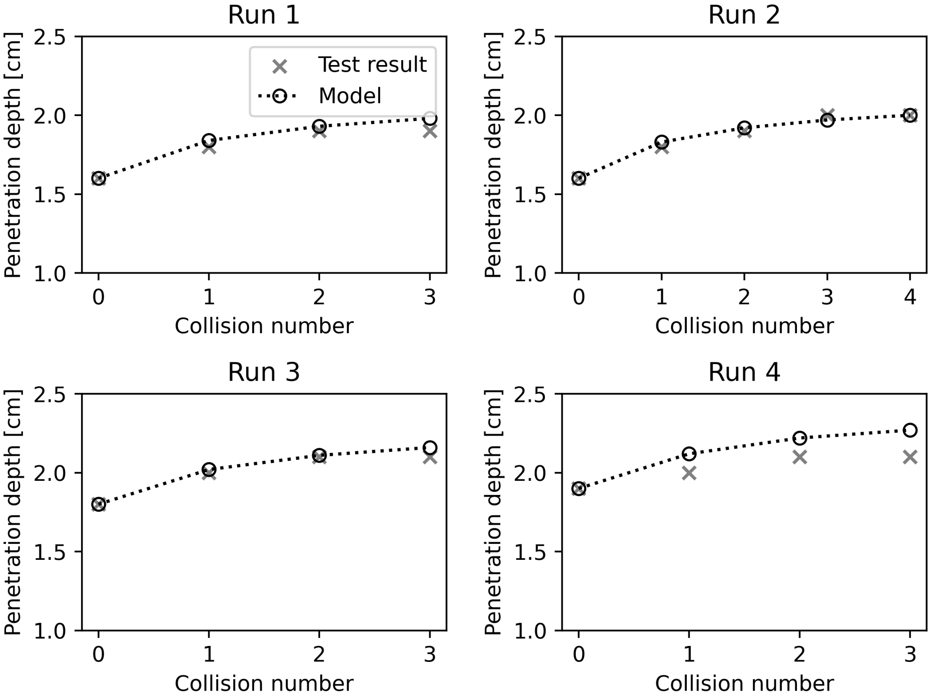

Figure 9.1: Results of the muli-stone lab tests plotted together with the outcomes of the WEMT method.

The model demonstrates a close match with the experimental data for the additional penetrations in the first two collisions, with only a slight deviation observed in runs 1, 2, and 3. However, in run 4, the model tends to overestimate the additional penetration by approximately one millimeter in the first collision. This discrepancy affects the subsequent collisions, as the penetration depth of each collision is calculated based on the prior collision.

According to the model, the additional penetration depth decreases by approximately half in each successive collision, aligning with Beemsterboer's theory. However, the experimental data indicates that in three out of the four runs, there is no noticeable additional penetration after three collisions. It is possible that there is some residual additional penetration after the third collision, such as 0.4 mm, which may not be detectable with the measurement technique employed in the experiments.

When the model is instructed to calculate two additional collisions for run one (collisions 4 and 5), the results are depicted in Figure 9.2. It is observed that collision 5 contributes only an additional 0.3mm to the penetration depth, which is rounded down to 0mm. In this case, it can be concluded that Beemsterboer (Beemsterboer, 2013) and Miedema (Miedema, 2021) were correct in their hypothesis that additional penetration becomes negligible after five stones are dropped successively onto the seabed.

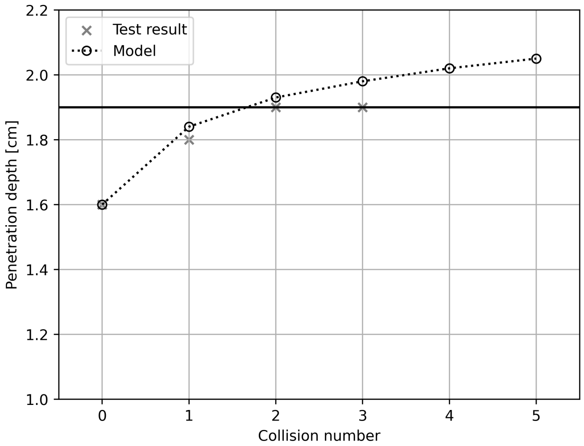

Figure 9.2: Final penetration depth after 5 collisions calculated using the WEMT model. The black horizontal line visualizes the final penetration depth measured during the lab experiments.

9.2. Conclusion

The application of the multi-stone theory to the WEMT method has yielded results that closely align with the data collected from the laboratory experiments. Although the actual collision dynamics in real-world scenarios are much more complex than what is accounted for in this method, the outcomes remain consistent with reality. Unlike in clay, the additional penetration resulting from marble collisions in sand is minimal. Both the experimental results and the model outcomes indicate that the additional penetration is often on the scale of tenths of millimeters. This is not expected to be significantly more when it is extrapolated to real-life size. This will however be tested later on in this thesis. The next objective is to devise a methodology for quantifying the volume loss during the rapid deposition of multiple stones. This scenario simulates real-life conditions where a considerable number of stones are dumped in a relatively short period. The aim is to understand how the cumulative impact of multiple stone deposits affects the volume loss and to establish a practical approach for estimating this phenomenon.

Part V

Modelling

10

Sensitivity analysis

As a result of numerous assumptions and simplifications, the outcomes of theoretical models will differ somewhat from reality. However, when ideal conditions are created regarding stone size, bed density and impact velocity, as was the case with the lab experiments, the model achieves high resemblance with the experiment results. It can be stated that the work energy method and the impulse-momentum method with soil resistance based on Terzaghi's theory and an effective- area and width that is based on Miedema's theory can be used to determine the immediate penetration of a single stone.
The models have been validated for different sizes, impact velocities and soil strengths and the theory appears to be able to accurately predict the penetration.

To assess the impact of various parameters in the model, a sensitivity analysis is conducted to examine the effect of input variables on the final penetration depth. This analysis helps identify which variables have a significant influence on the calculated penetration. In order to determine the influence of each individual variable, it is necessary to systematically modify each variable within an appropriate range while keeping all other variables constant. This allows for a comprehensive understanding of the relative importance of each variable in shaping the outcomes.
For the sensitivity analysis, Sobol' sampling is chosen as the method to investigate the model's sensitivity to certain input parameters. This is done by using the SALib package in Python. In Sobol' sampling, a set of input variables is chosen, and each variable is assigned a range or distribution of values. In Sobol' sampling, a set of input variables is chosen, and each variable is assigned a range or distribution of values. For each sample, the model is run, and the corresponding output values are recorded. By systematically varying the values of each input variable across multiple samples, Sobol' sampling provides a comprehensive exploration of the entire input space.
After running the model for all the different combinations of input parameters, the results are analysed and three sensitivity indices are presented per input parameter: S1 (first-order sensitivity index), S2 (second-order sensitivity index) and ST (Total-order sensitivity index). The S1 index quantifies the contribution to the output variance for the input variable in question, the S2 index quantifies the contribution to the output variance caused by the interaction between the input variable in question and all other input variables and finally the ST index quantifies the contribution to the output variance caused by the input variable in question, including both its first-order effects and all higher-order interactions. In this chapter we will only look at the ST index values for the input variables, the complete analysis can be found in Figure B.6a.

The input variables that will be part of the sensitivity analysis and their ranges are presented in Table 10.1 and an explanation of the values can be found in Figure B.6a.

Stone diameter	D	0.05	-	0.3	m
Stone density	ρ_s	2400	-	3400	kg/m^3
Water density	ρ_w	998	-	1050	kg/m^3
Coefficient of added mass	C_m	0.1	-	1	-
Drag coefficient	C_D	0.2	-	1.4	-
Depth of the seabed	z	1	-	50	m
Unit weight of the sand	γ'	1500	-	2000	kg/m^3
Impact velocity of the stone	v_{impact}	0	-	7	m/s

Table 10.1: Range of possible input variables

The result of the sensitivity analysis for the WEMT method is presented in Figure 10.1

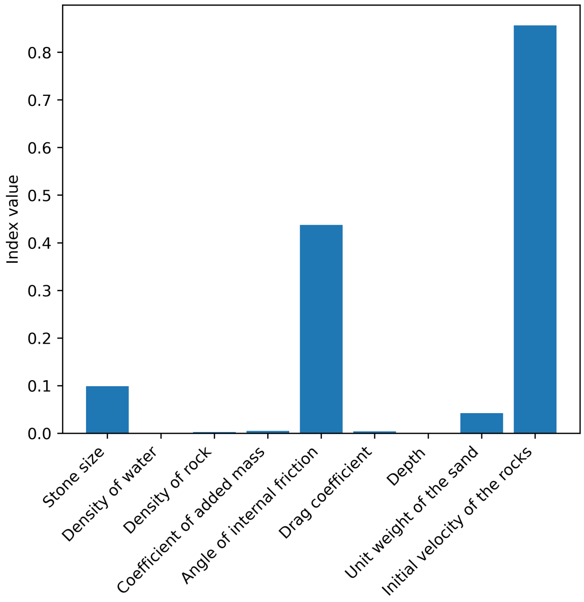

Figure 10.1: Total-order sensitivity index for all input variables for the WEMT method.

Figure 10.1 yields insightful results concerning the model's key input variables. Notably, the size of the rock, the impact velocity, and the angle of internal friction have been found to have the greatest influence on the results of the model. These factors play a crucial role in the reliability and precision of the calculated results, as demonstrated by the way they significantly influence the model's predictions. A more thorough analysis and clarification of these important variables will undoubtedly result in a more accurate and detailed comprehension of the penetration depth of rocks during subsea rock installation.

The sensitivity analysis outcomes have not only identified the angle of internal friction, rock size, and impact velocity as pivotal variables, but have also underscored the critical need for a comprehensive approach to handling these inputs. This underscores the importance of considering a range of values for the angle of internal friction, given its paramount significance in the model's accuracy. Relying solely on a single predetermined value can potentially trigger substantial errors, even with minor deviations. This underscores how small deviations can be magnified into considerable discrepancies within the overall model predictions. Consequently, it further underscores the urgency of incorporating a broader array of values for the angle of internal friction, encompassing inherent uncertainties and augmenting the model's resilience against potential disparities.
The S1 and S2 results of the sensitivity analysis can be found in Figure B.6a

11

Modelling subsea rock installation

The knowledge gained throughout the course of this thesis must be combined into a single model in order to create a preliminary estimate of the volume loss experienced during subsea rock installation via rock penetration into the sandy seafloor. Using the outputs of the models that were validated during the validation phase (discussed in Part IV), this model will determine the penetration depth that results from multi-stone penetration. It's critical to recognize that this is a simplified version of the complex process of subsea rock stacking.

Initially, the single stone model is employed to determine the penetration depth for a range of rock sizes that possess dimensions more aligned with reality compared to the marbles used in testing. After establishing the penetration depth for these real-sized rocks, the outcomes are harnessed to compute the additional penetration prompted by rock-rock collisions on the seafloor. Ultimately, the work conducted by Ravelli (Ravelli, 2012) is harnessed to approximate the dispersion pattern of rocks across the seafloor. Notably, Ravelli's study draws from CFD calculations, although the scope of his research encompasses results solely for a single stone size and two stand-off distances (SODs). The dispersion pattern of rocks is then leveraged to construct a map that delineates areas on the seafloor with the most pronounced volume loss.

11.1. Single stone penetration

First, the single stone penetration depth is calculated again since the multi-stone model is based on the single stone penetration depth. As the model explores scenarios that have not been physically tested, it is no longer possible to rely on directly measured impact velocities. This requires the adoption of Equation 4.3, as outlined in chapter 4. Through this formula, it becomes possible to determine the terminal settling velocity for all rock sizes. subsection 7.1.2 shows us that the measured impact velocity does not always correspond to the calculated impact velocity when a particle has not yet reached its terminal settling velocity. However, Figure 7.1 shows us that when the terminal settling velocity is approached, the differences between the theoretical- and measured velocity decrease. Nevertheless, the uncertainty will be taken into account in the model.

For now, soil properties are used that are similar to that of the coarse sand that was used for testing. This means that also the probability distribution for the angle of internal friction (Figure B.6b) will be used for demonstrating the model for rocks with realistic sizes. This leads to penetration depths for single stones that can be seen in Figure 11.1.

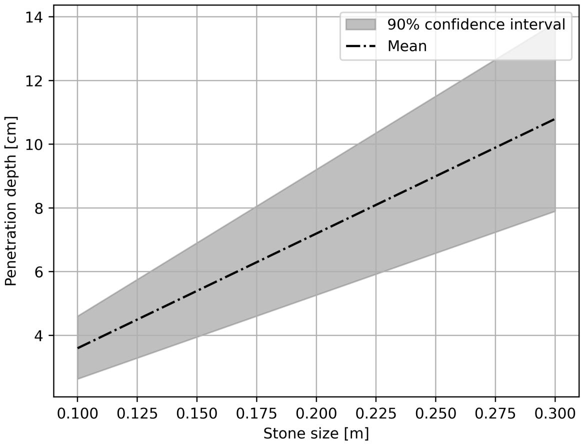

Figure 11.1: Single stone penetration depth for a range of rock sizes

Incorporating a probabilistic distribution for the impact velocity introduces an element of uncertainty into the model (as depicted in Figure 11.2). Nevertheless, as highlighted previously, neglecting the uncertainty associated with input variables can lead to a misleading impression of precision in relation to the model's output. As for Figure 11.2, a normal distribution is used for the impact velocity with for every stone size a mean equal to its terminal settling velocity as calculated with Equation 4.3 and a standard distribution of 5%.

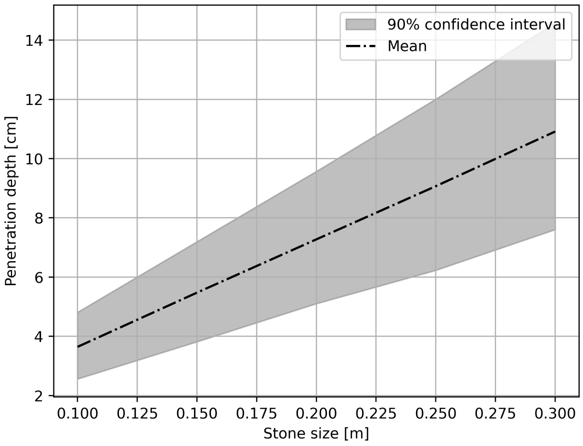

Figure 11.2: Single stone penetration depth for a range of rock sizes

Now that the single stone penetration depths are known for rocks with diameters between 10cm and 30cm, this can be used as input for the multi-stone model.

11.2. Multi-stone penetration

For the multi-stone model, the additional penetration as a result of rock-rock collisions on the seafloor will be illustrated for the two ends of the rock size spectrum: rocks measuring 10cm and those measuring 30cm (diameter).
The additional penetration will be calculated in the way that is described in chapter 5 and validated in chapter 9.

11.2.1. Rock collision

Initially, the additional penetration stemming from rock-rock collisions on the seafloor will be established for rocks having a diameter of 10cm. Currently, the angle of internal friction is the sole probabilistic input variable. This approach is adopted to clearly demonstrate the influence of input parameters.
A range of values for phi (ϕ) has once more been chosen because the angle of internal friction has a significant impact on the model's outcome. This range is normally distributed and has an average of 32.42 degrees and a standard deviation of 1.49 degrees, which is in line with the tested sand. From this normal distribution, a total of 10000 random samples are taken in order to determine the range in which 90% of the 10000 values fall. The extremes of this range are found to be $29.95°$ and $34.84°$. Naturally, these values may vary with each set of 10000 samples drawn. However, the disparity between the results of this approach generally remains within the range of approximately 0.03 degrees.

The effect this range for the angle of internal friction has on the outcomes of the model is quite extensive as can be seen in Figure 11.3

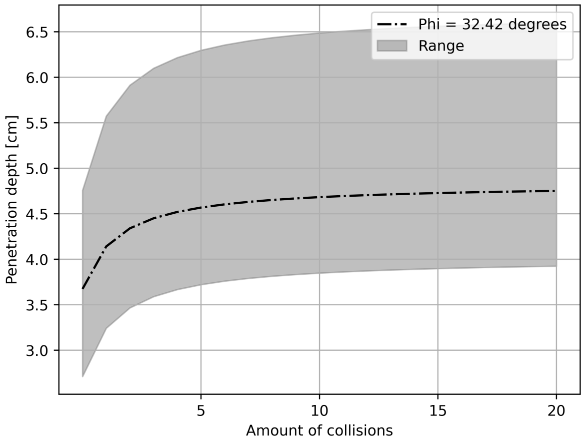

Figure 11.3: Figure showing what effect the range of values for the angle of internal friction has on the outcome of the multi-stone model when a 10cm stone is considered.

A similar calculation can be performed for rocks with a diameter of 30cm. Once more, the impact velocity matches the terminal settling velocity for the rock, as determined in Equation 4.3. For a rock of this dimension, the impact velocity amounts to 3.9 m/s. The range between the most advantageous penetration depth and the least favorable, considering the angle of internal friction, was established using the same values as for the 10cm diameter stone. The result can been seen in Figure 11.4

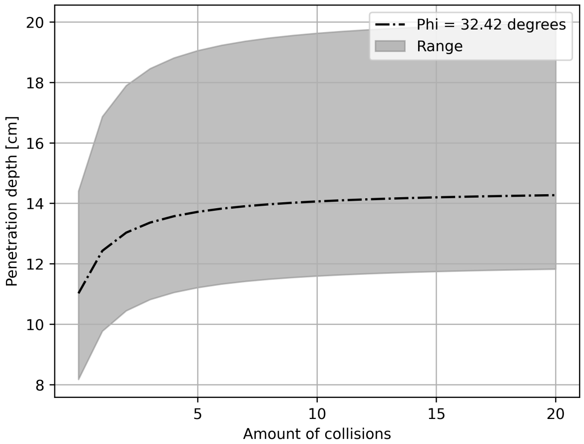

Figure 11.4: Figure showing what effect the range of values for the angle of internal friction has on the outcome of the multi-stone model when a 30cm stone is considered.

A noteworthy observation is that in both scenarios (10cm and 30cm rock), the penetration depth undergoes a 30% increment following 20 rock-rock collisions, considering the average value for the angle of internal friction (represented by the black dotted line in both figures).

11.2.2. Distributions of rocks on the seafloor

It is crucial to comprehend how stones are distributed on the seafloor after being released from the fallpipe. This information is essential for locating collision zones where stones are likely to interact vigorously. Understanding how stones settle after a fallpipe helps us understand where collisions between them are more likely to happen. This knowledge serves as a fundamental building block for estimating volume loss during the installation of subsea rock.

While acknowledging the complexity, some assumptions will be made regarding the distribution of rocks for the purposes of this thesis. These assumptions will serve as the basis for calculating the likelihood of collisions and the volume lost during the installation of subsea rocks. It's crucial to understand that, despite the fact that these assumptions simplify the actual situation, they still allow us to move forward with the analysis and shed light on the overall scheme of the procedure.

As mentioned earlier in this thesis, the work by Ravelli (Ravelli, 2012) will be utilized to establish a simplified rock distribution on the seafloor. While this simplification might not capture the full intricacies of the actual distribution, it offers a valuable starting point for assessing collision risks and volume loss. The spatial arrangement of stones post-fallpipe directly impacts collision dynamics. Knowing where stones end up allows us to predict collision hotspots accurately. This understanding becomes a cornerstone for estimating volume loss during subsea rock installation projects.

According to Ravelli, the rocks will end up according to a 2D normal distribution when the diameter of the rocks is 10cm, the diameter of the fallpipe is 1m, the SOD is 6m and the velocity with which the rocks leave the pipe is 5m/s. The mean of this normal distribution is -0.01m (this is almost exactly under the center of the fallpipe) and the standard deviation is 0.42 m. When the stand-off distance is 15m, the mean location is still -0.01m and the standard deviation is 0.48m. It is assumed that this 2D normal distribution for a SOD of 6m can also be used as a 3D normal distribution, with the same mean and standard deviation in the direction of both axes.

When a grid is created with square cells that have the same dimensions as the rocks (diameter $\cdot$ diameter), an accurate picture can be created of where the rocks end up. De dimensions of the grid are determined by the 95% confidence interval of the 3D normal distribution. Consequently, the initial step involves establishing the virtual placement of the rocks by randomly selecting values from the 3D distribution. Subsequently, the region encapsulating 95 percent of the rocks' final positions is defined, leading to the creation of the grid. Once the grid is in place, the model proceeds to calculate the quantity of rocks within each grid cell. An example of such a grid including the accumulation of rocks is shown in Figure B.6a. In this case, it concerns 300 dumped rocks with a diameter of 10cm.

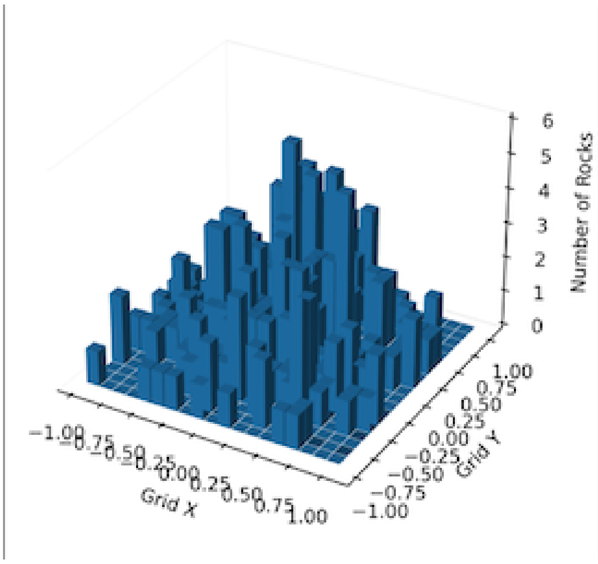

Figure 11.5: Distribution of 10cm rocks on a 3D grid. The z-axis represents the number of stones that are stacked on top of each other.

When Figure 11.5 is linked to Figure 11.3, the total penetration depth as a result of initial penetration and multi-stone penetration can be illustrated on the same grid as in Figure 11.5. This is shown in Figure 11.6.

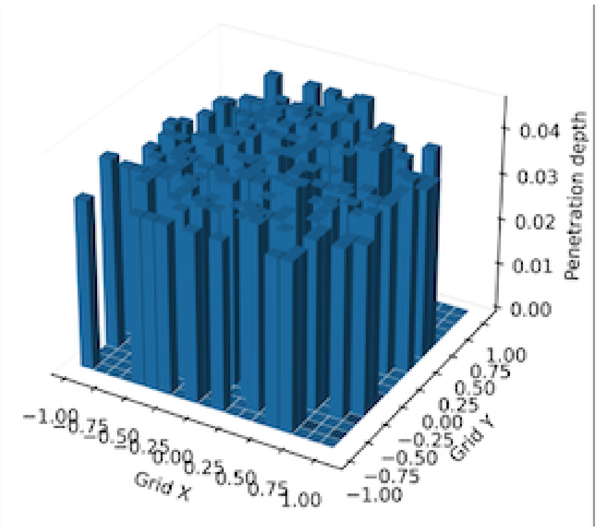

Figure 11.6: Total penetration depth as a result of the distribution shown in Figure 11.5

Because the additional penetration is so little compared to the initial penetration depth, it is hard to see the difference in total penetration depth between the cells. As already mentioned before, the total penetration depth corresponds to the number of rocks that ended up in a cell, combined with the multi-stone model outcomes that are illustrated in Figure 11.3. The mean value for ϕ was chosen to illustrate the average total penetration depth as a result of subsea rock installation.

11.2.3. Volume loss

The last essential step in this process involves calculating the volume loss per grid cell and subsequently summing up these values to determine the overall total volume loss. By quantifying the volume loss in each grid cell and aggregating these results, a clear picture can be created of the cumulative effect of subsea rock installation within the designated area. The volume loss per cell is calculated from the number of stones per grid cell and the total penetration depth per grid cell. The required formula for calculating the volume loss per grid cell is shown in Equation 11.1.

$$\text{Volume loss} = \begin{cases} 0, & d_t = 0 \\ \pi(r_s \cdot (d_t)^2 - \frac{1}{3}(d_t)^3), & d_t \leq r_s \\ \frac{1}{2}V_{rock} + (\frac{1}{2}V_{rock} - \pi(r_s \cdot (D - d_t)^2 & \\ -\frac{1}{3}(D - d_t)^3)), & d_t > r_s \end{cases} \tag{11.1}$$

Where:

d_t = Total penetration depth

The result of applying Equation 11.1 on Figure 11.5 and Figure 11.6, the result is a plot that illustrates the volume loss per grid cell. This plot is shown in Figure 11.7.

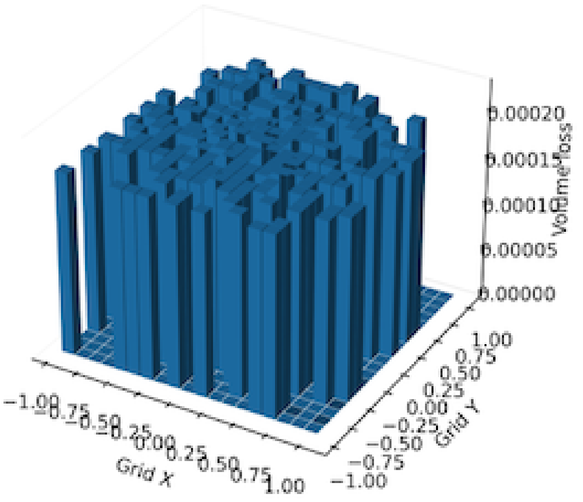

Figure 11.7: Volume loss per grid cell

The computation of the total volume loss involves the summation of volume loss values for each individual grid cell. In this particular scenario, the aggregate volume loss amounts to 0.037 m^3 of rock, corresponding to approximately 70 rocks. This substantial value represents nearly 25% of the overall volume. The results for the 30cm rocks can be found in section D.2. It is interesting to note that the relative volume loss is much less when larger stones are used. An explanation for this can be found in the fact that the same 3D distribution is used for rocks with a 0.1m diameter as for the rocks with a 0.3m diameter. This means that fewer stones will be subject to single penetration since there will be much more collisions. It is questionable if the distribution of the rocks on the seafloor is comparable for both scenarios, however, if it is then the use of larger rocks is recommended.

Part VI

Conclusions

12

Discussion and recommendations

This chapter will consist of two parts: one for the discussion (section 12.1) and one for the recommendations (section 12.2). In the discussion part, the results of the thesis will be interpreted and the significance of the results will be explained. Furthermore, there will be reflected upon the methodology and the limitations of the research will be discussed.
In the recommendations part, some suggestions will be made for future research on this topic or topics that are similar in nature.

12.1. Discussion

The adoption of the adapted Terzaghi method, originally intended for analyzing the maximum bearing capacity of shallow foundations, for assessing sand resistance against an indenter presents one of the assumptions made. Because foundations are designed not to move, the Terzaghi function does not take the dilatancy force into account, the force that is caused by the enlarging of the voids between the grains due to shearing. The reinforcing effect that dilatancy has on the bearing capacity is now simulated by overestimating the effective width and the effective area. It would make more sense physically if a formula could be used to show how this strengthening effect of dilatancy depends on the velocity and depth of penetration of the stone.

Moreover, the question of whether scaling the experiments up to their real dimensions can be extended in the way that was done in this thesis is still uncertain. While this appears to hold true with 3.5cm and 6cm marbles, it remains uncertain whether the same applies when working with stones measuring 15 to 30cm.

For the multi-stone part of the model, some more assumptions and simplifications are made. This is needed due to the complexity inherent in simulating the behavior of an aggregate mass of rocks, a task demanding intensive software resources and substantial computational power. The current model neglects to consider the contact forces that arise when rocks collide. As a consequence, the model relies solely on centric rock-rock collisions to calculate the additional penetration depth resulting from rocks landing atop each other. This oversimplified approach creates an unrealistic scenario wherein rocks neatly stack on one another, overlooking the real-world scenario in which rocks land partially on top of multiple other rocks that are already spread out on the seabed.

Furthermore, the current model does not take the potential reinforcing effect that previously penetrated rocks might exert on the soil's bearing capacity into account. Each stone penetrating the sand displaces a certain volume of sand, leading to a subsequent compaction of the sand layer. In principle, this compaction should enhance the soil's resistance to further stone penetration, but this hypothesis necessitates validation through subsequent research efforts.
Finally, during the lab experiments, it was observed that when the mass of water that a descending particle brings into motion is suddenly stopped due to penetration into a sand layer, the water mass acts as a jet and washes away part of the sand layer. This results in small scour holes that are filled

up with other dumped rocks, causing additional rock volume loss that is not taken into account.

12.2. Recommendations for further research

Since the single stone model can be considered quite accurate for the two different soil types that were used during lab testing, it is recommended for further research to focus more on the multi-stone part of the model. As already mentioned in section 12.1, the model would benefit from a more realistic way of describing rock-rock collisions within a bulk mass of dumped rocks.

The following additional research is recommended:

- **Physical model test for multi-stone additional penetration.**
  Incorporating the expansive water tank within the dredge laboratory at 3ME for physical model testing allows for the utilization of rocks that mirror real-world dimensions more accurately. Employing such a setup would enable the measurement of the overall penetration depth subsequent to rock deposition, potentially employing methods like settlement gauges. This approach promises to yield a more nuanced understanding of the interplay between rock size and volume loss, thus contributing to a more comprehensive comprehension of the phenomenon.
- **In situ measurement of volume loss.**
  A noticeable gap in this thesis lies in the absence of real-world data extracted from actual subsea rock installation projects. Such data would serve as a vital bridge between theoretical constructs and practical applications. It is strongly advocated that future endeavors leverage real data when accessible, facilitating the refinement and enhancement of the model. This incorporation would undoubtedly contribute to a more robust and accurate representation of the phenomenon under investigation.
- **In situ measurement of surface erosion of the seabed**
  As already mentioned in the discussion, more research on surface erosion during SRI is required. According to Visser and Van der Meer (Visser and Van der Meer, 2008), the surface erosion in clay can vary between 0 and 15 cm due to a soft top layer that is generally present when the seafloor is made up out of clay. It is unknown what the surface erosion will be for sandy seafloors. However, during the multi-stone tests for this thesis, a large amount of surface erosion was observed due to the mass of water a descending particle brings into motion. When this particle, in this case, a marble, is suddenly stopped due to penetration into a sand layer, the water mass acts as a jet and washes away part of the sand layer. A picture of this phenomenon is shown in Figure B.6 in section B.3. Further research is recommended into this erosion of the top layer of a sandy seafloor since it would cause the need for extra volumes of rock required to offset this erosion effect.
- **Development of a DEM model**
  It is recommended to progress toward the creation of a DEM model that integrates rock collision dynamics with geotechnical computations. To facilitate the development of this model, the utilization of real data from both physical model tests and actual subsea rock installation projects is advised.
  It is important to note that while this advanced model would demand significantly more computational time than the simplified model developed in this thesis, the considerable advantage lies in the higher precision and intricacy it would offer. The possible refined level of detail achieved through this approach would undoubtedly yield more accurate and comprehensive insights into the complex processes governing subsea rock installation.

13

Conclusion

In conclusion, this thesis' prime objective was to dive into a comprehensive exploration of volume loss during subsea rock installation, specifically focusing on the immediate penetration of rocks. This dimension, when combined with immediate settlement and surface erosion, forms a vital aspect of the overarching concept of volume loss in subsea rock installation. The primary quest revolved around understanding the sum of forces acting on a rock as it penetrates, a key factor in uncovering the single rock's penetration depth across different types of sandy seafloors.

Acknowledging the dynamic nature of rock penetration, the research delved into the intricacies of adding together diverse forces in a manner that genuinely captures the intricate interplay of net forces throughout the penetration process. Two distinct methodologies have been examined in detail for their applicability to this issue – the work-energy method and the impulse-momentum method – to depict the evolution of net forces and, in turn, the progression of single rock penetration in subsea rock installation.

To gather information about the relationship between the penetration depth and various input variables, lab tests were performed, and test data was gathered. Careful comparison between the results of all the different methods and the test data led to the conclusion that the WEMT- and IMMT methods (work-energy and impulse-momentum methods, notably leveraging Terzaghi's approach for bearing force determination and static values for effective- width and cross-sectional area), aligned best with test data, even though they inherently overestimated effective- width and cross-sectional area. This seemingly contradictory outcome can be explained by the influence of dilatancy effects in compacted sands. In these situations, the restricted permeability leads to heightened resistance as the voids between grains need to be filled with water owing to the expansion of these voids which, in turn, is a direct result of shear forces between the grains.

As previously mentioned, two methods closely matched test results. The average deviation between model output and lab test results for the 6cm marble test in coarse sand was only about 1.5%. Incorporating the uncertainty in angle of internal friction by considering a range of model outputs for various angles of internal friction revealed a 90% confidence interval that neatly aligned with the scatter of lab test results for both the WEMT- and the IMMT method.

For selecting the preferred method, factors such as computation time and result similarity were weighed. While both methods yielded similar outcomes, the impulse-momentum method demanded significantly more computational time. Consequently, the work-energy method emerged as the favored approach for addressing volume loss during subsea rock installation resulting from rock penetration.

Building on the foundation of single rock penetration depths on diverse sandy seafloors, this knowledge paved the way for the development of a multi-stone methodology. This innovative approach is rooted in momentum conservation, extending the insights from individual rock penetration to scenarios involving multiple rocks. Minor adaptations seamlessly transformed the single rock model into a multi-stone model.

To validate empirically, the dredge laboratory at 3ME facilitated a series of tests. These experiments involved dropping 6cm diameter marbles onto one another, scrutinizing collision dynamics intricately, and measuring the additional penetration depths resulting from these interactions. While acknowledging that real collision dynamics are much more intricate than the model's simplified rendition, which does not capture soil's spring-like behavior during collisions, it's intriguing to note that the model effectively predicted the extent of additional penetration arising from these collisions. Unlike in clay, the additional penetration resulting from marble collisions in sand is minimal.

The cumulation of efforts lies in the fusion of the multi-stone model with a three-dimensional normal distribution delineating the eventual positions of rocks post-fallpipe discharge. This amalgamation made it possible to calculate the collective penetration depth for rocks emerging from the fallpipe.

Comparing the aggregate volume loss across two scenarios – one with 10cm diameter rocks and the other with 30cm diameter rocks – yields an insightful pattern. A discernible inverse relationship emerges between rock size and volume loss, echoing our understanding of subsea rock installation, where larger rocks seemingly contribute less to overall volume loss.

References

Albaba, A. (2012). *Modelling creep and rate effects in soils* (Doctoral dissertation). https://doi.org/10.13140/2.1.1758.5443

Ambroso, M., Santore, C., Abate, A., & Durian, D. J. (2005). Penetration depth for shallow impact cratering. *Physical Review E*, *71*(5), 051305.

Beemsterboer, T. N. (2013). *Modelling the immediate penetration of rock particles in soft clay during subsea rock installation, using a flexible fallpipe vessel* (Master's thesis). TU Delft.

Bowles, J. E. (1988). *Foundation analysis and design*.

Brzinski III, T. A., Schug, J., Mao, K., & Durian, D. J. (2015). Penetration depth scaling for impact into wet granular packings. *Physical Review E*, *91*(2), 022202.

Ciamarra, M. P., Lara, A. H., Lee, A. T., Goldman, D. I., Vishik, I., & Swinney, H. L. (2004). Dynamics of drag and force distributions for projectile impact in a granular medium. *Physical review letters*, *92*(19), 194301.

Clark, A. H., & Behringer, R. P. (2013). Granular impact model as an energy-depth relation. *Europhysics Letters*, *101*(6), 64001.

Craig, W. H., & Sabagh, S. K. (1994). Stress-level effects in model tests on piles. *Canadian geotechnical journal*, *31*(1), 28–41.

Cubrinovski, M., & Ishihara, K. (1999). Empirical correlation between spt n-value and relative density for sandy soils. *Soils and Foundations*, *39*(5), 61–71.

Cubrinovski, M., & Ishihara, K. (2002). Maximum and minimum void ratio characteristics of sands. *Soils and foundations*, *42*(6), 65–78.

CUR. (2007). *The rock manual, the use of rock in hydraulic engineering*. Ciria.

Das, B. M., & Sivakugan, N. (2016). *Fundamentals of geotechnical engineering*. Cengage Learning.

de Bruyn, J. R., & Walsh, A. M. (2004). Penetration of spheres into loose granular media. *Canadian Journal of Physics*, *82*(6), 439–446.

de Vries, G., Brennodden, H., van der Meer, J., & Wendel, S. (2009). Ormen lange gas field: Immediate settlement of offshore rock supports. *Journal of offshore mechanics and Arctic engineering*, *131*(2).

Esteban, M. D., Diez, J. J., López, J. S., & Negro, V. (2011). Why offshore wind energy? *Renewable energy*, *36*(2), 444–450.

Esteban, M. D., López-Gutiérrez, J.-S., Negro, V., & Sanz, L. (2019). Riprap scour protection for monopiles in offshore wind farms. *Journal of Marine Science and Engineering*, *7*(12), 440.

Ghassemi, H., & Yari, E. (2011). The added mass coefficient computation of sphere, ellipsoid and marine propellers using boundary element method. *Polish maritime research*, *18*(1 (68)), 17–26.

GLDD. (2022). *Great lakes dredge & dock corporation awarded large-scale u.s. offshore wind rock installation project*. https://investor.gldd.com/news-releases/news-release-details/great-lakes-dredge-dock-corporation-awarded-large-scale-us

Hansen, J. B. (1970). A revised and extended formula for bearing capacity.

Hatanaka, M., & Feng, L. (2006). Estimating relative density of sandy soils. *Soils and foundations*, *46*(3), 299–313.

Holmen, J. K., Olovsson, L., & Børvik, T. (2017). Discrete modeling of low-velocity penetration in sand. *Computers and Geotechnics*, *86*, 21–32.

IADC. (2019). Subsea rock installation. *Facts about*.

Isbash, S. (1935). Construction of dams by dumping rock into flowing water.

Kaldellis, J., & Kapsali, M. (2013). Shifting towards offshore wind energy—recent activity and future development. *Energy policy*, *53*, 136–148.

Katsuragi, H., & Durian, D. J. (2007). Unified force law for granular impact cratering. *Nature physics*, *3*(6), 420–423.

Katsuragi, H., & Durian, D. J. (2013). Drag force scaling for penetration into granular media. *Physical review E*, *87*(5), 052208.

Meyerhof, G. (1956). Penetration tests and bearing capacity of cohesionless soils. *Journal of the Soil Mechanics and Foundations Division*, *82*(1), 866–1.

Miedema, S. (2014). *The delft sand, clay rock cutting model*. TU Delft open.

Miedema, S. (2021). Rock placement and stability for offshore windmill foundation.

Mujtaba, H., Farooq, K., Sivakugan, N., & Das, B. M. (2018). Evaluation of relative density and friction angle based on spt-n values. *KSCE Journal of Civil Engineering*, *22*, 572–581.

Nordstrom, K., Lim, E., Harrington, M., & Losert, W. (2014). Granular dynamics during impact. *Physical review letters*, *112*(22), 228002.

Offshore wind [Accessed: 2023-05-15]. (n.d.).

Patra, C., Sivakugan, N., & Das, B. (2010). Relative density and median grain-size correlation from laboratory compaction tests on granular soil. *International journal of geotechnical engineering*, *4*(1), 55–62.

Rambabu, M., Rao, S. N., & Sundar, V. (2003). Current-induced scour around a vertical pile in cohesive soil. *Ocean Engineering*, *30*(7), 893–920.

Ravelli, F. (2012). *Improving the efficiency of a flexible fallpipe vessel: An experimental study on the spreading of rock in an impinging plane jet* (Master's thesis). TU Delft.

Sánchez, S., López-Gutiérrez, J.-S., Negro, V., & Esteban, M. D. (2019). Foundations in offshore wind farms: Evolution, characteristics and range of use. analysis of main dimensional parameters in monopile foundations. *Journal of Marine Science and Engineering*, *7*(12), 441.

Seguin, A., Bertho, Y., Gondret, P., & Crassous, J. (2009). Sphere penetration by impact in a granular medium: A collisional process. *Europhysics Letters*, *88*(4), 44002.

Shill, S., & Hoque, M. (2015). Comparison of bearing capacity calculation methods in designing shallow foundations. *Gazipur, Bangladesh*.

Stevens, M. A., Gasser, M. M., & Saad, M. B. (1991). Wake vortex scour at bridge piers. *Journal of Hydraulic Engineering*, *117*(7), 891–904.

Stoter, M. (2018). On the fall process of rock during subsea rock installation: 1-d modelling of the falling process in the fallpipe.

Sumer, B. M. (2014). *Liquefaction around marine structures (with cd-rom)* (Vol. 39). World scientific.

Techet, P. A. (n.d.). *Derivation of added mass around a sphere*. https://web.mit.edu/2.016/www/handouts/Added%5C%20Mass%5C%20Derivation%5C%20050916.pdf

Terzaghi, K. (1943). *Theoretical soil mechanics*. John Wiley & Sons.

Uehara, J., Ambroso, M., Ojha, R., & Durian, D. J. (2003). Low-speed impact craters in loose granular media. *Physical Review Letters*, *90*(19), 194301.

Van der Schrieck, G. (2006). *Dredging technology: Ct5300*. TU Delft.

Van Rhee, C. (2002). On the sedimentation process in a trailing suction hopper dredger.

Vehmeijer, R. (2022). Modelling an inclined fallpipe for subsea rock placement.

Visser, R., & Van der Meer, J. (2008). Immediate displacement of the seabed during subsea rock installation (sri). *Terra et Aqua*, *110*, 3.

Wang, J.-P., François, B., & Lambert, P. (2017). Equations for hydraulic conductivity estimation from particle size distribution: A dimensional analysis. *Water Resources Research*, *53*(9), 8127–8134.

Whitehouse, R. J., Harris, J. M., Sutherland, J., & Rees, J. (2011). The nature of scour development and scour protection at offshore windfarm foundations. *Marine Pollution Bulletin*, *62*(1), 73–88.

Youd, T. (1973). Factors controlling maximum and minimum densities of sands. *Evaluation of relative density and its role in geotechnical projects involving cohesionless soils*, *523*, 98.

List of Figures

List of Tables

Acronyms

ELL Extreme Lower Limit. 10
EUL Extreme Upper Limit. 10

FPS Frames Per Second. 29

GLDD Great Lakes Dredge & Dock Company. i

IVP Initial Value Problem. 23

LT Length - to - Thickness ratio. 11

NLL Nominal Lower Limit. 10
NUL Nominal Upper Limit. 10

ODE Ordinary Differential Equation. 23

PDF Probability Density Function. 36

RK4 Fourth order Runge-Kutta method. 23

SOD Stand-Off-Distance. 63
SRI Subsea Rock Installation. 2
SSDV Side Stone Dumping Vessel. 8

UBC Ultimate Bearing Capacity. 14

WEMT Work-Energy-Miedema-Terzaghi. 51

Part VII

Appendices

A

Appendices(theory)

A.1. Effective area and effective width of a rock

The effective area of a rock is related to its effective width, which in turn depends on the penetration depth, as explained in Chapter 2 of this thesis. The effective area is the cross sectional area at a particular distance z1 from the lower bottom of the rock, where z1 is the penetration depth at moment t1. The formula for the effective area is shown in Figure B.6a.

$$A_{effective} = \frac{1}{4}W^2 \tag{A.1}$$

In which W is the effective width. When the rock penetrates further into the soil, the effective width will increase due to the shape of the rock (spherical). This means that at t2, the effective area will be dependent on z2, as shown in Figure A.1.

Figure A.1: Visualization of effective width

A.2. Python code for WEMT-method

```
    #Work-Energy-Miedema ODE Terzaghi
def differential_equation(z, K, params):
    # Unpack the parameters
    d_n50, m_s, V_rock, Am_s, Phi = params

    # Define other required variables
    g = 9.81
    rho_water = 1025
    rho_rock = 2650
    C_d = 0.4
    Dpth = 30
    unit_weight_soil = 1938
    k = 1.15e-3
    dn = 0.137
    CSA = (1/4 * np.pi * d_n50**2)
```

```
    # Extract the relevant variables from K
    v = np.sqrt(2 * K[0] / Am_s)

    # Calculate other required variables based on z and K
    s = z  # Assuming z is directly related to s

    # Calculate F_net as a function of z and K
    B = d_n50
    Aparticle = 1/4 * np.pi * d_n50**2

    c = 0
    unit_weight_water = rho_water
    EUW = (unit_weight_soil - unit_weight_water) * g

    if np.all(np.isclose(s, 0)):
        width = 0.00001
    elif np.all(np.greater_equal(s, 1/2 * d_n50)):
        width = d_n50
    else:
        width = 2 * np.sqrt((1/2 * d_n50)**2 - np.abs(s - 1/2 * d_n50)**2)

    A_particle = 1/4 * np.pi * width **2


    phi = math.radians(Phi)
    N_q = ((np.exp((3 * np.pi / 4 - phi/2)*math.tan(phi))**2)) / (2 * (math.cos(np.pi/4 + phi/2))**2
    N_gamma = (1.5 * (N_q - 1)) * math.tan(phi)
    N_c = (N_q - 1)/(math.tan(phi))
    dp = ((v * A_particle)/k ) * dn * rho_water * g
    soil_stress = 100000 + (unit_weight_water * Dpth * g + unit_weight_soil * s * g)
    water_pressure = 100000 + (unit_weight_water * Dpth * g + unit_weight_water * s * g) #- dp
    water_pressure = np.where(water_pressure < 0, 0, water_pressure)
    ES = soil_stress - water_pressure


    F_grav = m_s * g  # gravitational force
    F_buoy = V_rock * rho_water * g  # buoyancy force 1
    F_drag = 1/2 * rho_water * Aparticle * C_d * (2/m_s * K)  # drag force
    F_bearing = CSA * (1.2 * c * N_c + ES * N_q + 0.4 * EUW * d_n50 * N_gamma)
    F_net = F_grav - F_buoy -  F_drag - F_bearing


    # Calculate the derivative dK/dz
    dKdz = F_net

    return dKdz

def event(z, K, params):
    return K[0]

event.terminal = True
```

```
# Define the parameters
d_n50 = d50
rho_water = 1025
rho_rock = 2650
C_m = 0.4
V_rock = (np.pi * d_n50 ** 3) / 6
m_s = V_rock * rho_rock
Am_s = (V_rock * rho_rock) + (C_m * V_rock * rho_water)
Phi = phi1

params = [d_n50, m_s, V_rock, Am_s, Phi]

# Define the range of V0 values
V0 = 2.75

# Initialize an empty array to store the z_crossing values
z_crossing_values = []


# Define the initial condition
K0 = 0.5 * Am_s * V0**2

initial_condition = [K0]
z_span = (0, 1.0)  # Range of z values for integration

# Solve the ODE with termination condition
solution = solve_ivp(lambda z, K: differential_equation(z, K, params), z_span, initial_condition, ev

# Retrieve the value of z where K=0
z_crossing = solution.t_events[0][0]
```

A.3. Plot of all methods

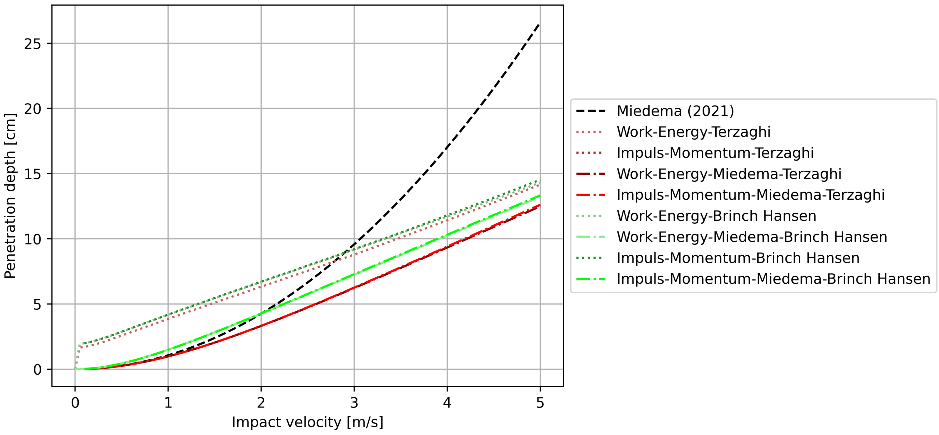

Figure A.2: Results of all the different methods described in section 4.5 for a 20cm rock in sand with an angle of internal friction of 32 degrees.

B

Appendices (data gathering)

B.1. Sand properties

The datasheet for the Dorsilit sand can be found on the following page.

TECHNISCHES DATENBLATT

together more future ®
dorfner

Dorsilit® 8 FG 0,3 - 0,8 mm

Erstellt Mai 2011 von
ESch
Revision 2

Eigenschaften: Dorsilit® - Kristallquarzsande sind gewaschene Sande, die sich durch ihren hohen SiO2- Gehalt und die Abwesenheit von Huminstoffen und anderen Verunreinigungen auszeichnen.

Chemische Analyse

	[Ma.-%]
SiO_2	98
Al_2O_3	0,8
Fe_2O_3	0,01
Ti_2O	0,04
K_2O	0,3
Na_2O	0,03
CaO	0,02
MgO	0,01
Glühverlust $_{1000 °C}$	0,25

Lieferform: Lose oder verpackt in 25 kg Säcken, sowie Big Bags á ca. 1.500 kg

Hinweis: Verpackte Produkte unterliegen der normalen Alterung und sollten nicht länger als 6 Monate gelagert werden. Hinweise auf die Entsorgung etc. können Sie unserem Sicherheitsdatenblatt entnehmen.

Feuchtigkeit DIN ISO 787,T2	< 1	[Ma.-%]
Dichte	2,63	[g/ml]
Schüttdichte	1,6	[g/ml]

Kornverteilung

mm	[Ma.-%] ca.
>1	Spuren
> 0,8	1
0,63 - 0,8	31
0,315 - 0,63	67
< 0,315	1
d_{50}	0,51mm

Typische Werte:

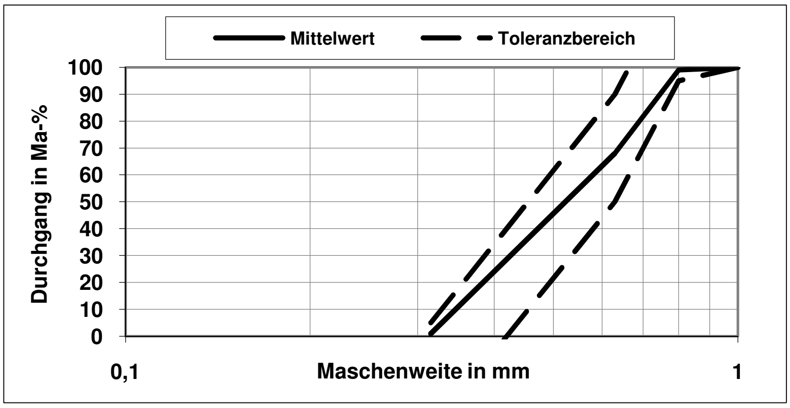

Basis: Produktionsdurchschnittswerte 2008/2009

Wir weisen ausdrücklich darauf hin, dass es sich bei den vorliegenden Produkten um Naturprodukte handelt, die veredelt und/oder gemischt sein können (auch mit synthetischen Produkten). Alle angegebenen Daten und Werte sind daher lediglich als Richtwerte, die produktspezifische Toleranzbreiten haben können, zu verstehen. Unser Vertragspartner bleibt verpflichtet, die Tauglichkeit des Produkts für seine Einsatzzwecke zu prüfen und konkrete Auskünfte über Toleranzbreiten und anwendungstechnische Erfahrungen aufgrund der naturgegebenen sowie produktions- und lagerstättenbedingten Toleranzen für den konkreten Verwendungszweck zu erfragen. Im Übrigen gelten unsere "Allgemeinen Verkaufs- und Lieferbedingungen". Die genannten Analysenwerte stellen keine Garantie oder Zusicherung im rechtlichen Sinne dar, sondern basieren auf durchschnittlichen Jahreswerten. Aktuelle Analysenwerte stellen wir auf Wunsch gerne zur Verfügung.

The datasheet for the Sibelco sand can be found on the following two pages.

Verpakking 40kg

WIT ZAND

Omschrijving: Kwartszand van Mol

Het kwartszand van Mol,M32 wordt na ontginning industrieel bewerkt: gezeefd, gewassen en geklasseerd. Het kwartszand van Mol vormt een uitstekende grondstof voor diverse toepassingen zoals bv. Keramische industrie, pleisters, mortels, coatings enz…
Deze kwaliteit wordt verpakt in 25kg en 40kg en BigBag 1,5 ton.

Korrelverdeling en Fysische eigenschappen
Methode: ISO-zeving

M32	
D50	260µm
> 355 µm	7%
> 250 µm	57%
> 180 µm	93%
< 63 µm	≤0,1%
soortelijk gewicht	2,65kg/dm3
stortgewicht	1,5kg/dm3
hardheid	7 Mohs
pH	7
gloeiverlies	0,15 %
kleur L*	70 Minolta CM-3610d
a*	2,79 D65/10°
b*	9,82

Chemische Samenstelling (XRF) %

	M32
SiO2	99,5
Fe2O3	0,03
Al2O3	0,20
TiO2	0,03
K2O	0,05
CaO	0,01

Bovenvermelde informatie is gebaseerd op gemiddelde waarden. De typische eigenschappen en chemische analyses zijn bedoeld als voorbeelden en kunnen niet beschouwd worden als vervanging voor eigen testen en onderzoek in alle omstandigheden waarbij eigenschappen en chemische samenstellingen kritische factoren zijn. Verkoop en levering geschieden steeds volgens onze alge-

KWARTSZAND VAN MOL M31 - M32 - M34

De kwartszanden van Mol - **M31, M32** en **M34** - worden na ontginning industrieel bewerkt: gezeefd, gewassen en geklasseerd. Deze kwaliteiten zijn vochtig en gedroogd leverbaar; per vrachtwagen, wagon of schip; in bulk en in zakken (droog).
De **kwartszanden van Mol** vormen een uitstekende grondstof voor de glas-, kristal- en keramische industrie, voor de gieterijen, voor tegellijmen, pleisters, mortels, coatings enz…

KORRELVERDELING EN FYSISCHE EIGENSCHAPPEN
Methode: ISO-zeving

		M31	M32	M34	
D50		370	260	170	µm
AFS		45	50	75	
> 1000 µm		1			%
> 710 µm		5			%
> 500 µm		25			%
> 355 µm		53	7		%
> 250 µm		85	57	3	%
> 180 µm		98	93	30	%
> 125 µm				91	%
< 63 µm		sporen	≤ 0,1	≤ 0,3	%
soortelijk gewicht		2,65	2,65	2,65	kg/dm³
stortgewicht		1,6	1,5	1,4	kg/dm³
hardheid		7	7	7	Mohs
pH		7	7	7	
gloeiverlies		0,15	0,15	0,15	%
kleur	L*	70	70	72	Minolta CM-3610
	a*	2,63	2,79	1,93	D65/10°
	b*	9,58	9,82	7,76	

B.2. Angle of internal friction determination

To incorporate the empirical correlation between the uniformity coefficient, angularity, and the $e_{min}-e_{max}$ range, a probability density function needs to be included as an input variable in the Terzaghi formula. This formula is used to determine the bearing capacity of the two types of sand used in laboratory testing. Figure B.1 and Table B.1 presented by Youd (Youd, 1973) are used to establish this probability density function.

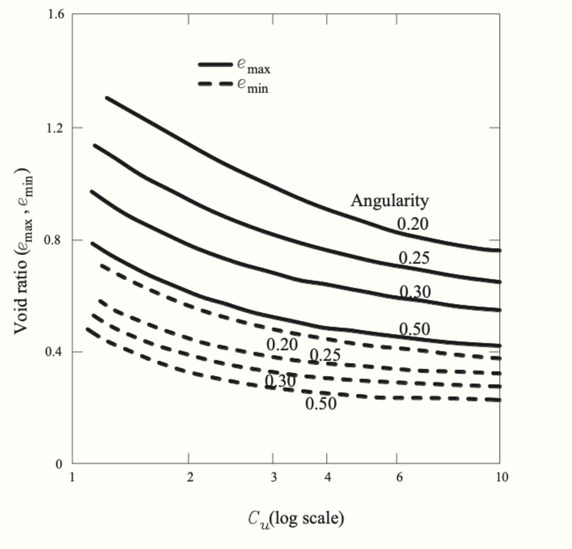

Figure B.1: Variation of e_{max} and e_{min} with C_u and angularity (Patra et al., 2010).

Angularity class	Angularity interval	Mean angularity
Very angular	0.12 - 0.17	0.14
Angular	0.17 - 0.25	0.21
Subangular	0.25 - 0.35	0.30
Subrounded	0.35 - 0.49	0.41
Rounded	0.49 - 0.70	0.59
Well rounded	0.70 - 1	0.84

Table B.1: Correlation between friction angle and relative density (Meyerhof, 1956)

The angularity interval for subangular sand results in an e_{min} interval and an e_{max} interval for both types of sand. These intervals are shown in Table B.2 and were determined using the correlation between the uniformity coefficient, angularity and e_{min} / e_{max} in Figure B.1. Since the void ratio is a value that was determined by measuring the sand properties in the lab, a small range of $\pm$ 10% is used.

Sand	e_{min} interval	e_{max} interval	e interval
Fine	0.44 - 0.57	0.88 - 1.1	0.51 - 0.63
Coarse	0.43 - 0.5	0.81 - 1	0.67 - 0.81

Table B.2: e_{min} and e_{max} intervals as a result of the angularity interval.

Since there is no information given on the distribution of the values within the ranges given by Youd (Youd, 1973), a uniform distribution is assumed. The distribution of the values in the ranges for e_{min} and e_{max} are determined by using the Sobol' sequence in Python. This uses a quasi-random sampling method to generate samples across the parameter space. The Sobol' sequence ensures a more even spread of samples compared to traditional random sampling methods. The range of values for each

parameter is defined by the bounds specified in the problem definition, but the distribution of samples within that range is not assumed or controlled by the sampling method itself. The ranges are given in Table B.2.
In Python, Sobol' sampling is now utilized to generate 8000 combinations of the three input variables required for calculating relative density. By employing a loop in Python, these combinations result in 8000 relative densities and, subsequently, 8000 angles of internal friction. To depict the probability density functions (PDFs), normal distributions are formed by calculating the mean and standard deviation, as shown in Figure 6.7.

B.3. Multi-stone experiments

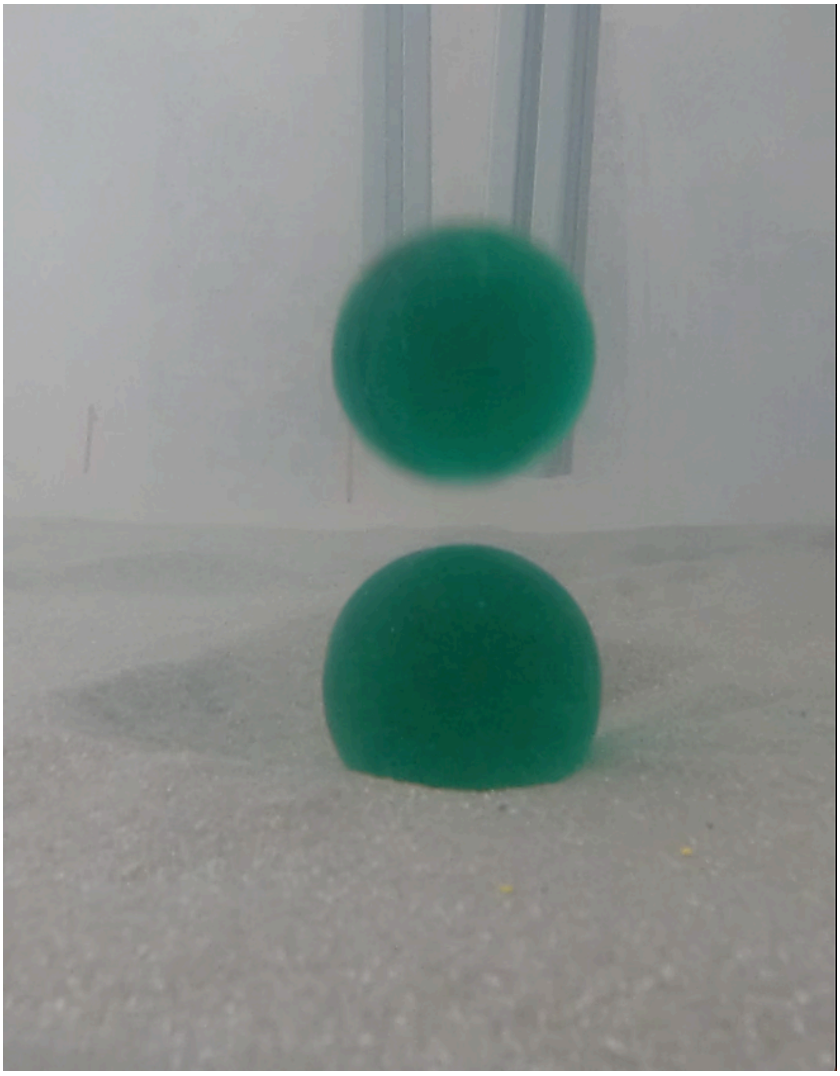

Figure B.2: Snapshot of one the multi-stone experiments

Figure B.3: Snapshot of one the multi-stone experiments

B.4. Tracker

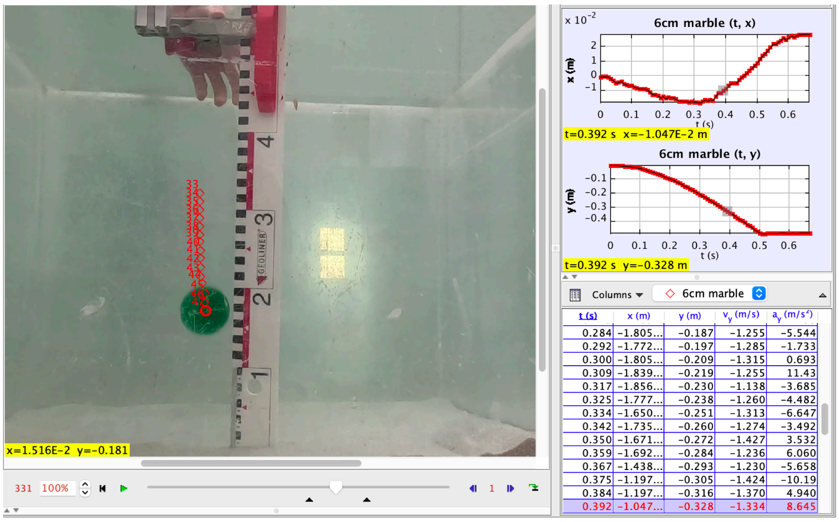

t (s)	x (m)	y (m)	v_y (m/s)	a_y (m/s²)
0.284	−1.805...	−0.187	−1.255	−5.544
0.292	−1.772...	−0.197	−1.285	−1.733
0.300	−1.805...	−0.209	−1.315	0.693
0.309	−1.839...	−0.219	−1.255	11.43
0.317	−1.856...	−0.230	−1.138	−3.685
0.325	−1.777...	−0.238	−1.260	−4.482
0.334	−1.650...	−0.251	−1.313	−6.647
0.342	−1.735...	−0.260	−1.274	−3.492
0.350	−1.671...	−0.272	−1.427	3.532
0.359	−1.692...	−0.284	−1.236	6.060
0.367	−1.438...	−0.293	−1.230	−5.658
0.375	−1.197...	−0.305	−1.424	−10.19
0.384	−1.197...	−0.316	−1.370	4.940
0.392	−1.047...	−0.328	−1.334	8.645

Figure B.4: Tracker video analysis for determining impact velocity.

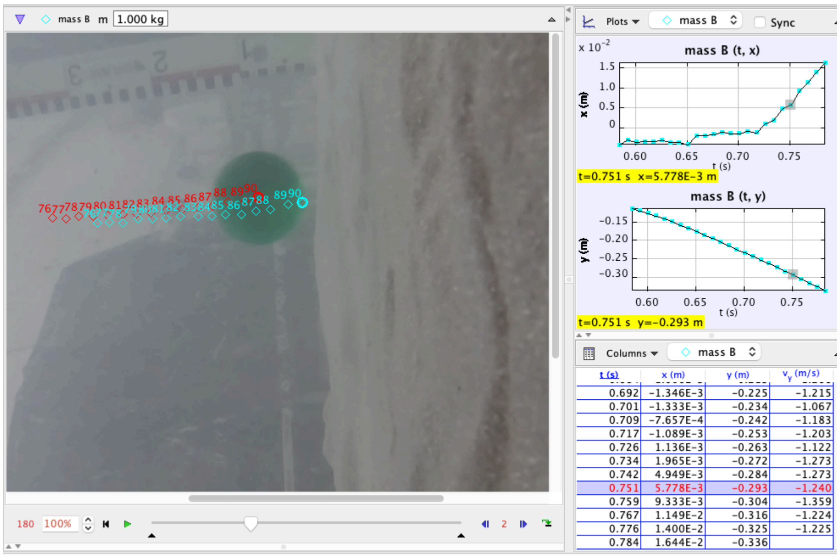

t=0.751 s x=5.778E-3 m

t=0.751 s y=-0.293 m

t (s)	x (m)	y (m)	v_y (m/s)
0.692	-1.346E-3	-0.225	-1.215
0.701	-1.333E-3	-0.234	-1.067
0.709	-7.657E-4	-0.242	-1.183
0.717	-1.089E-3	-0.253	-1.203
0.726	1.136E-3	-0.263	-1.122
0.734	1.965E-3	-0.272	-1.273
0.742	4.949E-3	-0.284	-1.273
0.751	5.778E-3	-0.293	-1.240
0.759	9.333E-3	-0.304	-1.359
0.767	1.149E-2	-0.316	-1.224
0.776	1.400E-2	-0.325	-1.225
0.784	1.644E-2	-0.336	

Figure B.5: Tracker video analysis for determining impact velocity.

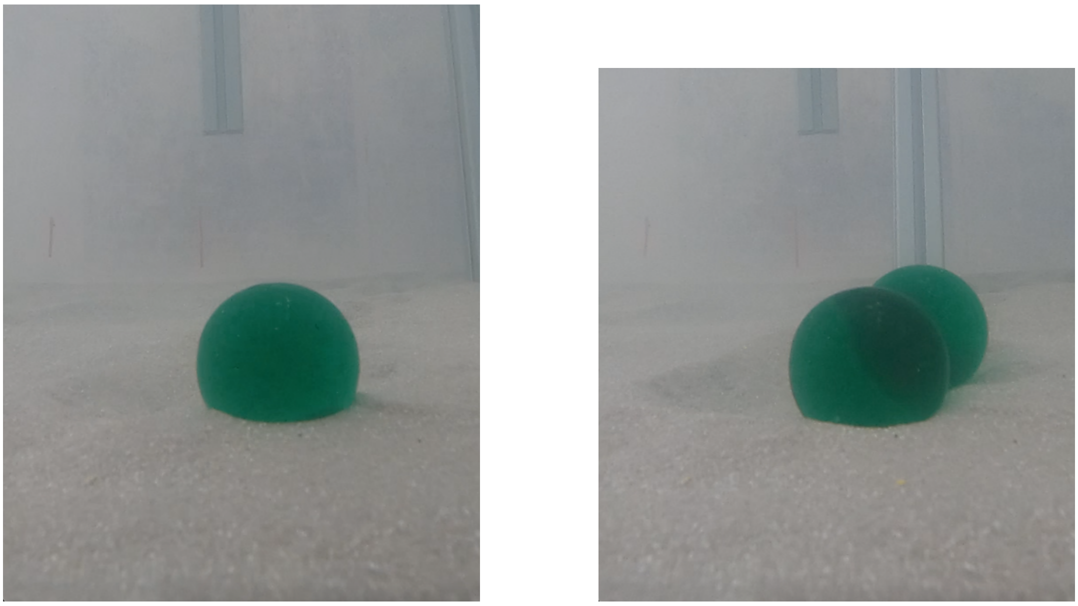

(a) (b)

Figure B.6: Two moments are captured here during multi-stone penetration testing. It can be clearly seen that after collision (b), a crater was formed next to marble 1 (the one already in the sand before the collision). This crater was created by the jet effect caused by marble 2 bringing the water surrounding it into motion.

C

Appendices (Validation)

C.1. Relative error

C.1.1. Large marble in coarse sand, WEMT method

Impact velocity [m/s]	Lab result [cm]	Model result [cm]	Relative error [%]
0.75	0.7	0.56	−20.64
0.82	0.5	0.65	29.81
0.83	0.7	0.66	−5.32
0.86	0.7	0.70	0.64*
1.20	1.4	1.22	−12.90
1.21	1.5	1.24	−17.64
1.25	1.1	1.30	18.20
1.29	1.5	1.37	−8.97
1.32	1.6	1.41	−11.58
1.36	1.6	1.48	−7.44
1.40	1.3	1.53	19.06
Mean			−1.52

Table C.1: Relative errors for the large marble in coarse sand, using the WEMT method. * *Relative error $\neq$ 0 as a result of rounding the model outcome to two decimal places.*

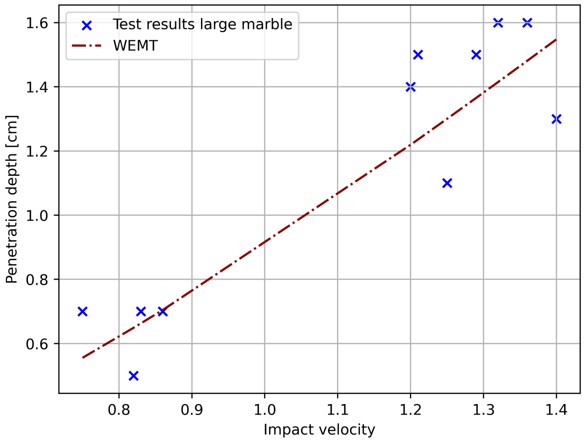

Figure C.1: Results for the WEMT method plotted together with the lab test results

C.1.2. Large marble in coarse sand, IMMT method

Impact velocity [m/s]	Lab result [cm]	Model result [cm]	Relative error [%]
0.75	0.7	0.56	−20.69
0.82	0.5	0.65	29.73
0.83	0.7	0.66	−5.29
0.86	0.7	0.71	0.83*
1.20	1.4	1.22	−12.71
1.21	1.5	1.24	−17.42
1.25	1.1	1.30	18.63
1.29	1.5	1.37	−8.82
1.32	1.6	1.42	−11.32
1.36	1.6	1.49	−7.07
1.40	1.3	1.55	19.60
Mean			−1.32

Table C.2: Relative errors for the large marble in coarse sand, using the IMMT method. * *Relative error $\neq$ 0 as a result of rounding the model outcome to two decimal places.*

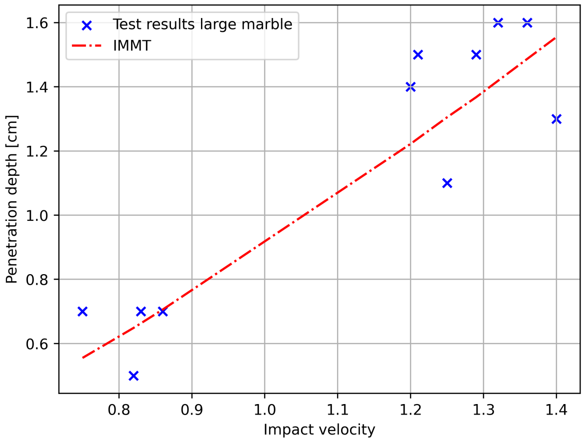

Figure C.2: Results for the IMMT method plotted together with the lab test results

C.1.3. Medium marble in coarse sand, WEMT method

Impact velocity [m/s]	Lab result [cm]	Model result [cm]	Relative error [%]
0.81	0.7	0.58	−16.66
0.82	0.7	0.60	−14.98
0.85	0.6	0.63	5.13
0.95	0.5	0.75	50.52
0.99	0.7	0.80	14.64
1	0.5	0.82	63.00
1.15	0.9	1.01	11.88
1.2	1.1	1.07	−2.53
1.26	1.2	1.15	−4.08
Mean			11.88

Table C.3: Relative errors for the medium marble in coarse sand, using the IMMT method.

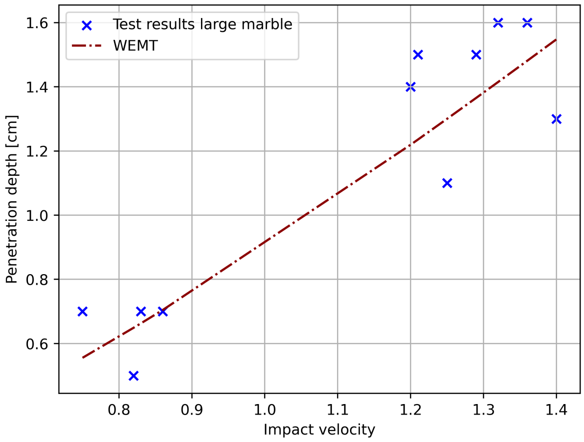

Figure C.3: Results for the WEMT method plotted together with the lab test results

C.1.4. Medium marble in coarse sand, IMMT method

Impact velocity [m/s]	Lab result [cm]	Model result [cm]	Relative error [%]
0.81	0.7	0.58	-16.46
0.82	0.7	0.60	-14.74
0.85	0.6	0.63	4.94
0.95	0.5	0.76	51.09
0.99	0.7	0.80	14.75
1	0.5	0.82	63.27
1.15	0.9	1.01	12.27
1.2	1.1	1.08	-2.05
1.26	1.2	1.15	-3.85
Mean			12.14

Table C.4: Relative errors for the medium marble in coarse sand, using the IMMT method.

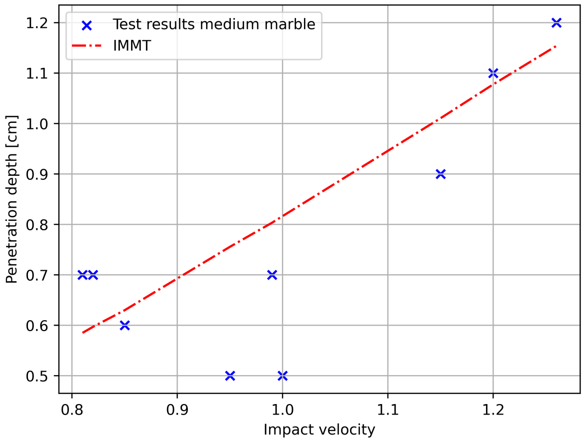

Figure C.4: Results for the IMMT method plotted together with the lab test results

C.2. Large marble in fine sand, WEMT method

Impact velocity [m/s]	Lab result [cm]	Model result [cm]	Relative error [%]
0.8	0.2	0.17	−16.49
0.85	0.2	0.19	−6.09
0.86	0.2	0.19	−3.94
1.24	0.4	0.39	−3.66
1.25	0.5	0.39	−21.76
1.26	0.4	0.40	−0.74 *
1.35	0.3	0.45	50.44
1.37	0.3	0.46	54.59
1.38	0.5	0.47	−6.00
Mean			5.15

Table C.5: Relative errors for the large marble in fine sand, using the WEMT method. * *Relative error $\neq$ 0 as a result of rounding the model outcome to two decimal places.*

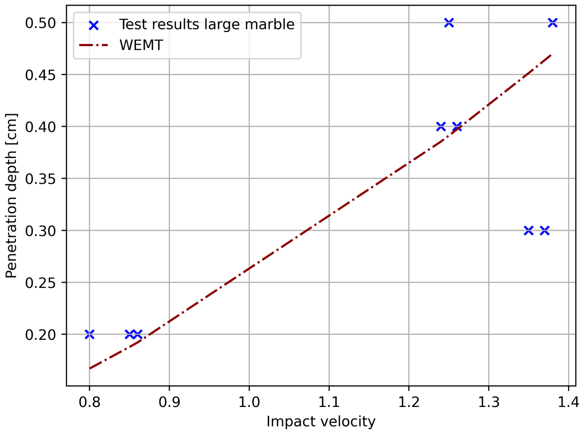

Figure C.5: Results for the WEMT method plotted together with the lab test results

C.3. Large marble in fine sand, IMMT method

Impact velocity [m/s]	Lab result [cm]	Model result [cm]	Relative error [%]
0.8	0.2	0.16	−20.03
0.85	0.2	0.18	−7.91
0.86	0.2	0.19	−5.49
1.24	0.4	0.38	−4.77
1.25	0.5	0.39	−22.52
1.26	0.4	0.39	−1.53
1.35	0.3	0.45	50.56
1.37	0.3	0.46	54.80
1.38	0.5	0.47	−5.85
Mean			4.14

Table C.6: Relative errors for the large marble in fine sand, using the IMMT method.

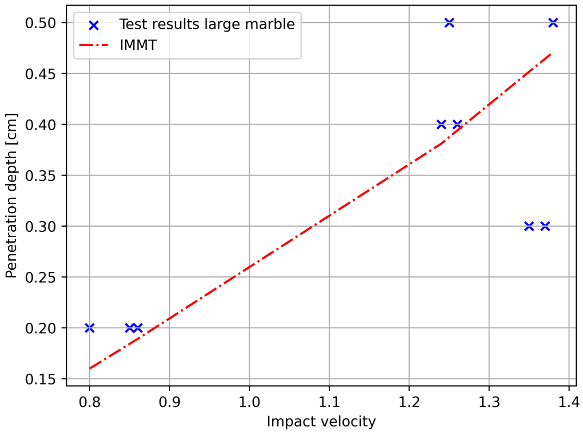

Figure C.6: Results for the WEMT method plotted together with the lab test results

C.4. Medium marble in fine sand, WEMT method

Impact velocity [m/s]	Lab result [cm]	Model result [cm]	Relative error [%]
0.8	0.3	0.16	-45.49
0.8	0.2	0.16	-18.23
0.82	0.2	0.17	-14.31
1.07	0.5	0.28	-43.62
1.10	0.3	0.30	-1.14
1.13	0.3	0.31	3.85
Mean			-19.82

Table C.7: Relative errors for the medium marble in fine sand, using the WEMT method.

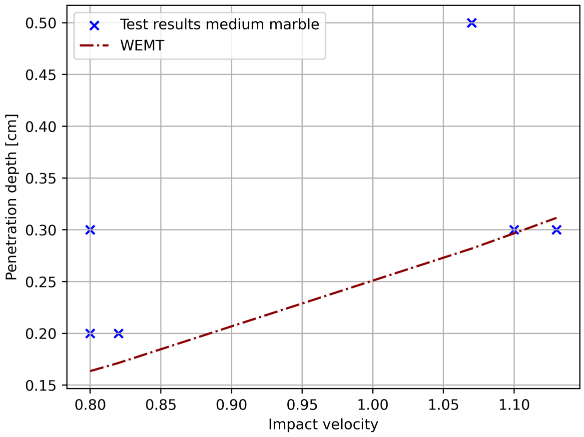

Figure C.7: Results for the WEMT method plotted together with the lab test results

C.5. Medium marble in fine sand, IMMT method

Impact velocity [m/s]	Lab result [cm]	Model result [cm]	Relative error [%]
0.8	0.3	0.15	−48.58
0.8	0.2	0.15	−22.86
0.82	0.2	0.16	−18.12
1.07	0.5	0.28	−44.77
1.10	0.3	0.29	−2.36
1.13	0.3	0.31	3.18
Mean			−22.25

Table C.8: Relative errors for the medium marble in fine sand, using the IMMT method.

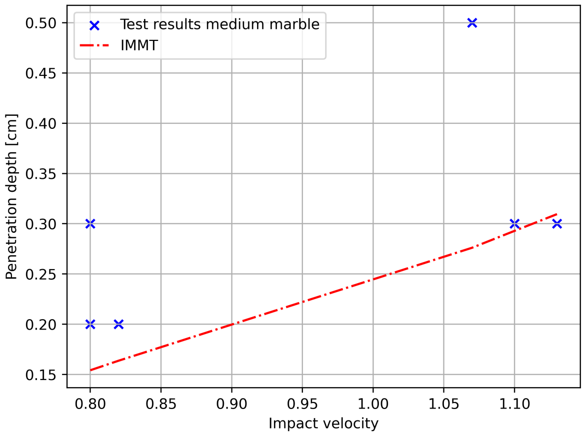

Figure C.8: Results for the IMMT method plotted together with the lab test results

C.6. Probabilistic approach

In this section, the results of the probabilistic approach are shown. The probabilistic approach involves the inclusion of the uncertainty concerning the internal angle of friction of the sand that was used for testing.

C.6.1. Large marble in coarse sand, WEMT method

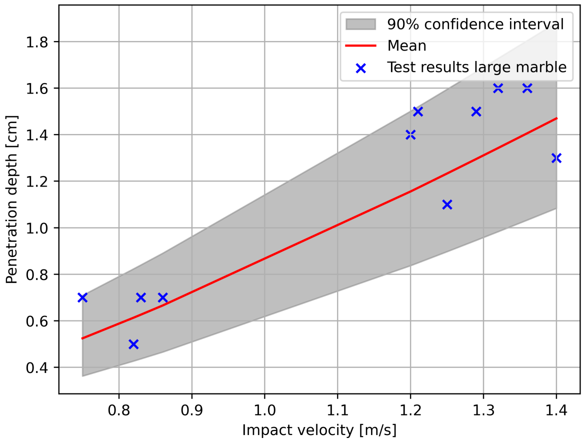

Figure C.9: Figure showing the 90% range for the penetration depth of the large marble when the angle of internal friction is picked from Figure B.6b

C.6.2. Medium marble in coarse sand, WEMT method

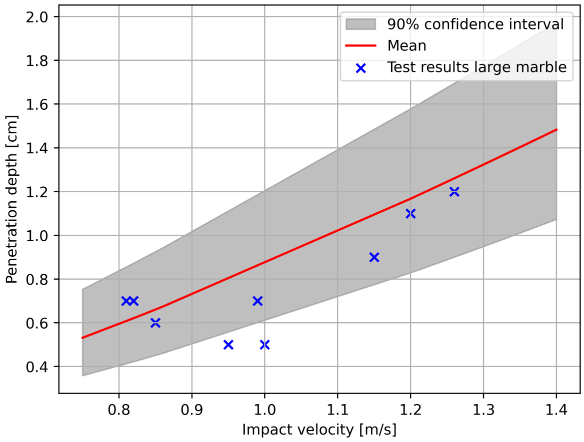

Figure C.10: Figure showing the 90% range for the penetration depth of the medium marble when the angle of internal friction is picked from Figure B.6b

C.6.3. Large marble in fine sand, WEMT method

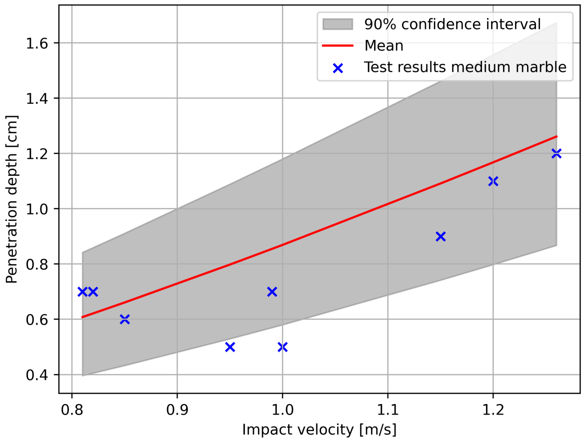

Figure C.11: Figure showing the 90% range for the penetration depth of the large marble when the angle of internal friction is picked from Figure 8.5a

C.6.4. Medium marble in fine sand, WEMT method

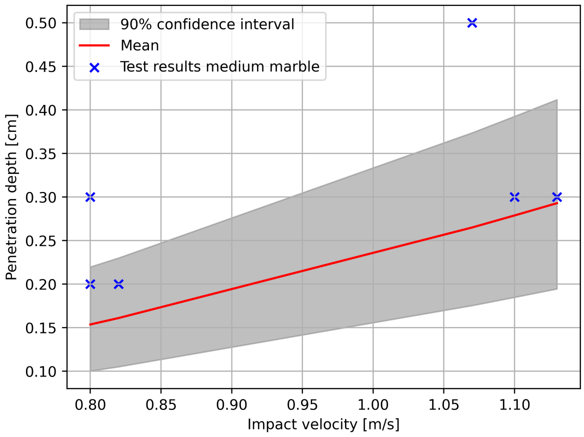

Figure C.12: Figure showing the 90% range for the penetration depth of the medium marble when the angle of internal friction is picked from Figure 8.5a

C.6.5. Large marble in coarse sand, IMMT method

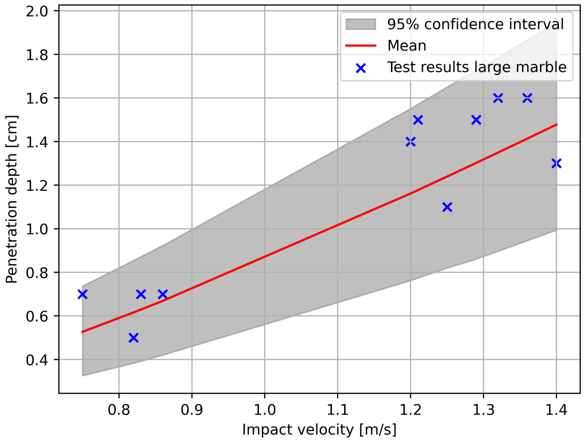

Figure C.13: Figure showing the 90% range for the penetration depth of the large marble when the angle of internal friction is picked from Figure B.6b

.

C.6.6. Medium marble in coarse sand, IMMT method

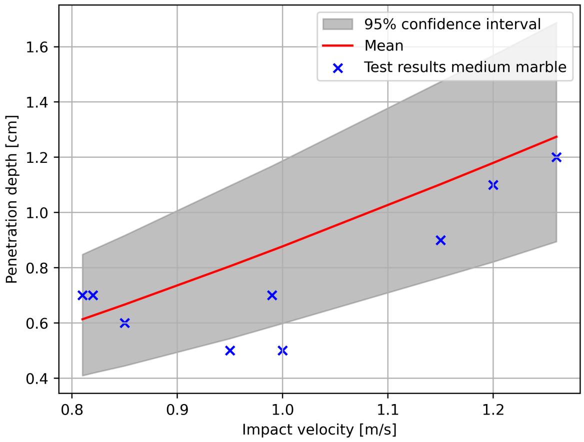

Figure C.14: Figure showing the 90% range for the penetration depth of the large marble when the angle of internal friction is picked from Figure B.6b

.

C.6.7. Large marble in fine sand, IMMT method

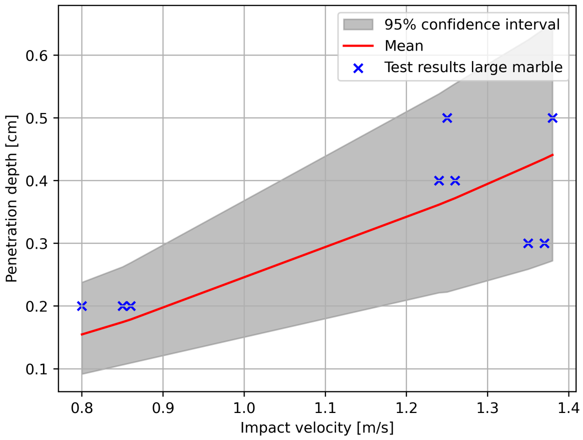

Figure C.15: Figure showing the 90% range for the penetration depth of the large marble when the angle of internal friction is picked from Figure 8.5a

.

C.6.8. Medium marble in fine sand, IMMT method

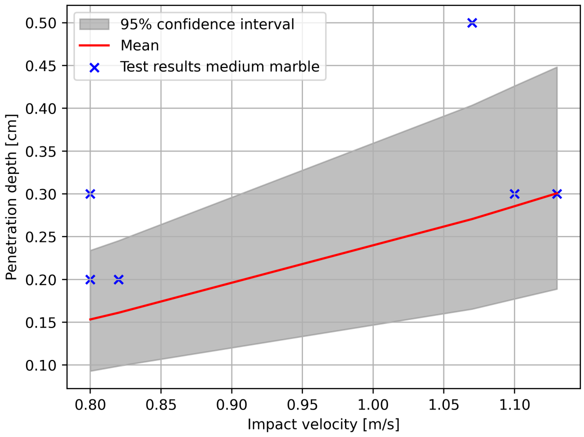

Figure C.16: Figure showing the 90% range for the penetration depth of the medium marble when the angle of internal friction is picked from Figure 8.5a

.

D

Appendices (modelling)

D.1. Global sensitivity analysis

The ST- (total) and S2 results of the global sensitivity analysis are shown here. Again, the S2 index quantifies the contribution to the output variance caused by the interaction between the input variable in question and all other input variables

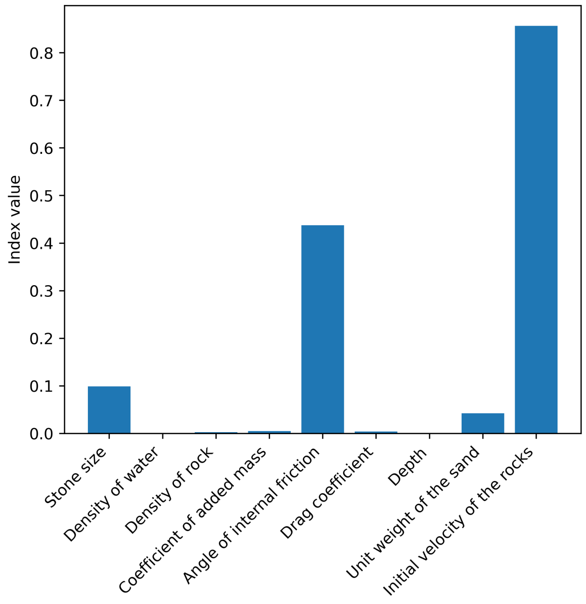

Figure D.1: Total-order sensitivity index for all input variables for the WEMT method.

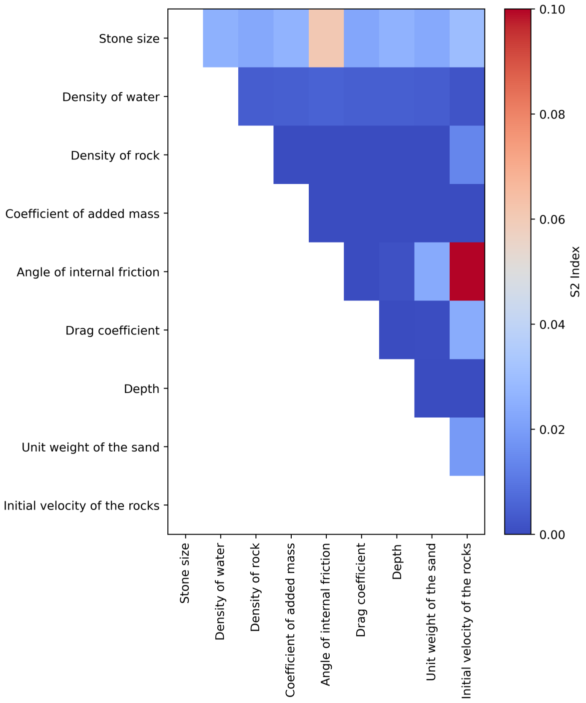

Figure D.2: S2 sensitivity index for all input variables for the WEMT method.

D.2. Multi-stone modelling

The results of the multi-stone model for rocks with a 30cm diameter are shown below. It concerns rock distribution over the seafloor, total penetration depth, and volume loss.

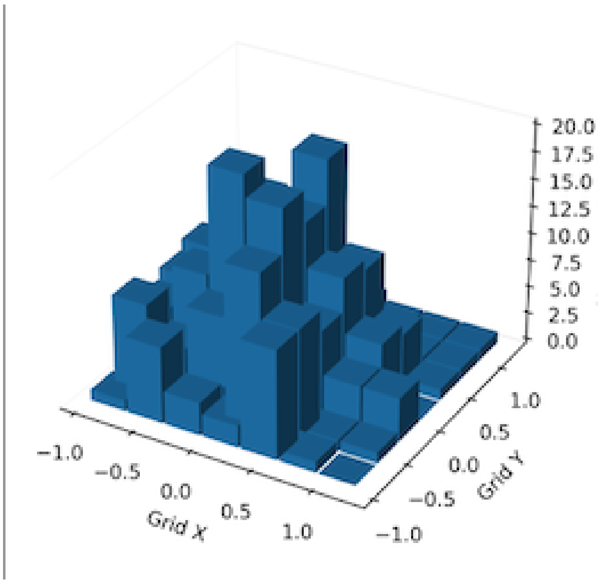

Figure D.3: Distribution of the rocks over the seafloor for rocks with a diameter of 30cm. The z-axis represents the number of rocks per grid cell.

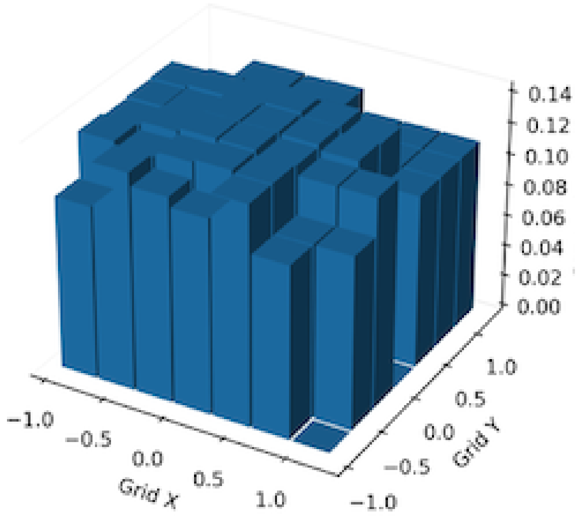

Figure D.4: Total penetration depth as a result of the distribution shown in Figure D.3. The z-axis represents the penetration depth in cm.

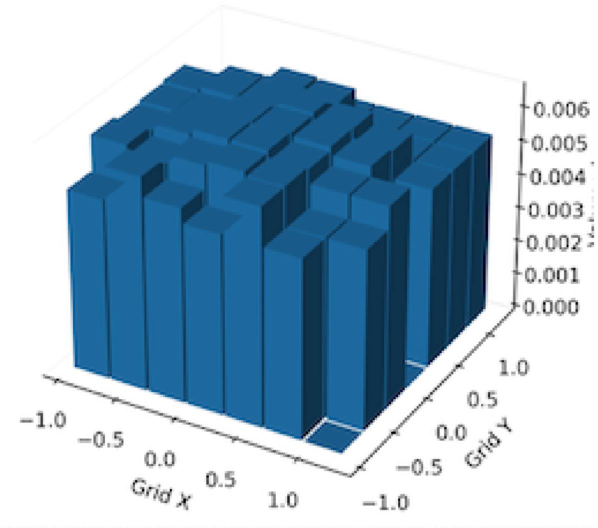

Figure D.5: Volume loss per grid cell due to the rock distribution shown in Figure D.3. The total volume loss is equal to 0.27 m^3. The z-axis represents the volume loss per grid cell in cubic meters.